DEVELOPMENT AND ASSESSMENT OF A NOVEL AMORPHOUS SILICA ENCAPSULATION TECHNOLOGY FOR MITIGATING BIOTOXICITY OF WELDING FUME PARTICLES

By

JUN WANG

A DISSERTATION PRESENTED TO THE GRADUATE SCHOOL
OF THE UNIVERSITY OF FLORIDA IN PARTIAL FULFILLMENT
OF THE REQUIREMENTS FOR THE DEGREE OF
DOCTOR OF PHILOSOPHY

UNIVERSITY OF FLORIDA

2013

To my parents, Dr. Xiaode Wang and Mrs. Xuhui Hou, my wife, Mrs. Yingjia Zhu, and lovely daughter, Ms. Cecilia Wang. They always support and encourage me, give me the strength, and inspire me to achieve the milestone here.

ACKNOWLEDGMENTS

First, I would like to thank my supervisor Dr. Chang-Yu Wu, for his continuous patience and guidance throughout my doctoral study. Dr. Wu is the role model for me in the research and academic world. He dedicated all his resources to light up my path and help me climb the “Ph.D. mountain” and see the beauty of the “summit”.

I am sincerely grateful to my family. Without their endless support and cheering up, I would not be able to push the boundaries. My daughter, Cecilia Wang, who was born at the same time with the completion of this dissertation, is the greatest gift in my life.

I want to acknowledge the funding agencies supporting my doctoral study, particularly Mrs. Kathleen Paulson at Naval Facilities Engineering Command. The funding agencies are the reason my studies can be completed without financial disruption.

I would like to thank my whole Ph.D. committee, namely Dr. Myoseon Jang, Dr. Wesley Bolch, Dr. Vito Ilacqua, and Dr. Jean-Claude Bonzongo, for their time, attention, criticism, and encouragement.

I would like to mention all the undergraduate student assistants, including Mr. Mark Kalivoda, Ms. Jianying Guan, Ms. Jessica Sharby, and others who worked with me. The undergraduate students’ enthusiasm helped me achieve the research goal, while working with them honed my mentorship skill.

Finally, I want to express my deepest gratitude to those who helped, cared, and inspired me, in the past, present, and future.

TABLE OF CONTENTS

page

LIST OF TABLES

LIST OF FIGURES

LIST OF ABBREVIATIONS

ACGIH	American Conference of Governmental Industrial Hygienists
ANOVA	ANalysis Of VAriance
ASE	Amorphous Silica Encapsulation
ASTM	American Society for Testing and Materials
AWS	American Welding Society
BP	Base Plate
CO	Carbon Monoxide
ELPI	Electrical Low Pressure Impactor
FL	Fusion line
GMAW	Gas Metal Arc Welding
GTAW	Gas Tungsten Arc Welding
HAP	Hazardous Air Pollutant
HAZ	Heat Affected Zone
IC	Ion Chromatography
ICP-AES	Inductively Coupled Plasma-Atomic Emission Spectroscopy
IDST	Insulated Double Shroud Torch
LEV	Local Exhaust Ventilation
LPM	Liter Per Minute
NIOSH	National Institute for Occupational Safety and Health
NO	Nitric Oxide
OSHA	Occupational Safety and Health Administration
PEL	Permissible Exposure Limit
PPE	Personal Protection Equipment
REL	Recommended Exposure Limit

SCE	Silica Coating Efficiency
SMAW	Shielded Metal Arc Welding
SMPS	Scanning Mobility Particle Sizer
TEM	Transmission Electron Microscopy
TEOS	Tetraethyloxysilane
TMS	Tetramethylsilane
TWA	Time weighted average
WM	Weld metal
XPS	X-ray photoelectron spectroscopy

Abstract of Dissertation Presented to the Graduate School
of the University of Florida in Partial Fulfillment of the
Requirements for the Degree of Doctor of Philosophy

DEVELOPMENT AND ASSESSMENT OF A NOVEL AMORPHOUS SILICA ENCAPSULATION TECHNOLOGY FOR MITIGATING BIOTOXICITY OF WELDING FUME PARTICLES

By

Jun Wang

August 2013

Chair: Chang-Yu Wu
Major: Environmental Engineering Sciences

Welding generates a large number of metallic nanoparticles and poses serious health risks to welders. The tightening occupational standard requires more reduction in exposure, which is not satisfied by current control technologies. The objective of this study was to develop an amorphous silica encapsulation (ASE) technology for limiting chromium oxidation and encapsulating fume particles with an amorphous silica layer and to assess its effectiveness.

A quantitative method to determine silica coating efficiency (SCE) on metal particles was first developed. Different acid mixtures were tested as digestion methods targeting at metals and silica coating. SCEs were calculated based on the measured concentrations following digestion by HNO_3/HF and aqua regia. The results showed that 14-39% of fume particles were encapsulated. The low SCEs were due to premature decomposition of silica precursor. An insulated double shroud torch (IDST) was designed to overcome the premature decomposition by separating the flows of the shielding gases. The results from the laboratory and field demonstrated over 90% reduction of Cr^{6+}. The SCEs using the IDST were enhanced to around 48~64% at the

low and medium primary shielding gas flow rates. The highest SCE of 76% occurred at the high shielding gas flow rate (30 Lpm) with a TMS carrier gas flow of 0.64 Lpm. Transmission electron microscopy (TEM) images confirmed the amorphous silica layer on the fume particles. The concentration of TMS was below safety threshold (1%) in the worst case scenario. Mechanical structure tests showed that the quality of welds from the baseline and from the ASE technology were similar.

With only a 3.8% additional cost, this novel ASE technology has the potential to cost-effectively address the welding fume exposure issue, which has been listed as “priority research area” in the National Occupational Research Agenda. Upon successful demonstration, this novel technology can help the industries meet the occupational standard, and protect over 0.5 million welders in the US. The newly developed method to quantify SCEs can be used in other silica coated nanoparticles applications. The study helps further understand how silica and metals interact in a high temperature aerosol system.

CHAPTER 1
INTRODUCTION

Background

Stainless steel contains alloying metals such as chromium (Cr), nickel (Ni), and manganese (Mn) (Peckner and Bernstein 1977; Marshall 1984). Stainless steel welding, the joining of pieces of metal with stainless steel filler material, is a common industrial practice. These metals in welding filler materials such as wires and electrodes can vaporize during the welding process due to the high temperature of the welding arc. The metals are oxidized and subsequently form nano-sized particles as the temperature drops (Hewett 1995; Zimmer and Biswas 2001; Moroni and Viti 2009) which may stay airborne in welders' breathing zones (Schoonover et al. 2011).

The welding fumes pose potential adverse health risks to welders, who may inhale toxic metals such as hexavalent chromium (Cr^{6+}), Ni, Mn, and other toxic components. Because of their nanometer to sub-micrometer size, the inhaled particles can penetrate deeply into the human respiratory tract (Yu et al. 2000; Biswas and Wu 2005; Geiser and Kreyling 2010). Upon contact with human organs, these metals can be released from the particles, absorbed, distributed, and metabolized (Li et al. 2004).

Chromium, because of its resistance to corrosion and discoloration (Marshall 1984; Kropschot and Doebrich 2010), is one of the major components of stainless steel. Cr^{6+} is formed as a result of Cr oxidation with reactive species such as oxygen and ozone in the welding arc zone (Gray et al. 1983; Dennis et al. 1997). Cr^{6+} exposure continues to be a troublesome issue in industrial occupation environments (Korczynski 2000; Pellerin and Booker 2000). Among all the metals present in welding fumes, Cr^{6+} draws the most concern due to its carcinogenic effect (IARC 1990), which has been

confirmed by extensive human and animal data (Langård 1988; USEPA 1998). By contrast, trivalent chromium (Cr^{3+}) is relatively less toxic and actually one essential nutrient for human metabolism activity (Anderson 1997). Among all the other metals in welding fumes, nickel is also a known human carcinogen (IARC 1990), while manganese is a neurotoxin that can induce neurological symptoms such as cognition dysfunction (Harris et al. 2011; Laohaudomchok et al. 2011; Summers et al. 2011). Numerous toxicological studies have shown that welders inhaling fume particles are exposed to these toxic metals and bear the risk of respiratory diseases, neurological symptoms, and cancer (Keskinen et al. 1980; Antonini et al. 1998; Antonini et al. 2003; Antonini et al. 2007; Flynn and Susi 2009; Harris et al. 2011; Rice et al. 2011; Summers et al. 2011; Zeidler-Erdely et al. 2011; Thaon et al. 2012).

The exposure limits set by regulatory agencies and professional organizations are listed in Table 1-1. The Occupational Safety and Health Administration (OSHA) does not currently regulate total welding fumes; the National Institute for Occupational Safety and Health (NIOSH) considers welding fumes to be potential occupational carcinogens and has set the recommended exposure limit (REL) at the lowest feasible concentration (NIOSH 2007). The American Conference of Governmental Industrial Hygienists (ACGIH) has also assigned welding fumes an 8-hour time weighted average (TWA) threshold limit value (TLV) of 5 mg/m^3 (ACGIH 2012). OSHA lowered the 8-hour time weighted average (8-hr TWA) permissible exposure limit (PEL) for Cr^{6+} from 52 $\mu g/m^3$ to 5 $\mu g/m^3$ in 2006.(OSHA 2006a) NIOSH just lowered 10-hr TWA REL for Cr^{6+} of 1 $\mu g/m^3$ (NIOSH 2008) to 8-hr TWA REL of 0.2 $\mu g/m^3$ in 2013. Because of the residual risk of lung cancer even at REL (NIOSH 2008), NIOSH also recommended adoption of

reasonable control technology to further reduce Cr^{6+}. Although ACGIH recommended a TLV of 50 µg/m^3, the value has not been updated since 2006. The tightening standards revealed the fact that the previously set high value was not enough for protecting the workers. All the relevant agencies regulate or recommend exposure limits for Ni and Mn from 15 ng/m^3 to 5 mg/m^3 level (Table 1-1), which are more tolerated than for Cr^{6+}. It should be noted that NIOSH RELs are always order of magnitude lower than OSHA PEL. OSHA regulates the permissible exposure standard to an economically feasible level for the industries, and offers the appropriate protection for the workers. NIOSH recommends the conservative values based on the newest research.

Table 1-1. Exposure limits for airborne Cr^{6+}, Ni, Mn, and welding fume

Airborne	OSHA (2006a)	NIOSH (2008)	ACGIH (2012)
Cr^{6+}	5 µg/m^3	0.2 µg/m^3 (2013)	50 µg/m^3
Ni	1 mg/m^3	0.015 mg/m^3	0.1~1.5 mg/m^3
Mn	5 mg/m^3	1 mg/m^3	0.2 mg/m^3
Welding fume	Not regulated	Lowest feasible	5 mg/m^3

Distribution of Welding Fume Particles in the Human Body

The deposition pattern of welding fume particles in the human respiratory system are determined by various parameters, such as particle size distribution (PSD) (ICRP 1994) and flow rate (Geiser and Kreyling 2010). Some large size particles will be removed directly by mechanical exhalation through mouth or nose. The median diameter of the welding fume particles is around 20 nm (Zimmer and Biswas 2001). Particles in this nanometer range have a higher probability of reaching the conducting airways or the alveoli (Oberdorster et al. 2005), from where they are not easily removed by mechanical exhalation. After deposition, the release of the metals from the

nanoparticle complex depends on the particle size and solubility of the metals. The metals dissolved in the biological fluid will then enter the systemic blood stream. The undissolved particles will be carried by the cilia towards the pharynx, where they were either swallowed or expelled via coughing.

Inhalation exposure to Cr^{6+} and Ni, which are carcinogens, can lead to the development of neoplasms following initiation, promotion, and progression stages of carcinogenesis (ATSDR 2008a). Cr^{6+} is known to coordinate with DNA bases and disrupt DNA structure (Hansen and Stern 1985). The absorption of Cr through inhalation to the lungs depends on the oxidation state of the Cr, i.e., Cr^{3+} or Cr^{6+}. The kinetic process for Cr^{6+} follows a linear first order kinetics, with about 80% of the Cr^{6+} compounds removed from the lungs in a week (ATSDR 2008a). Absorbed Cr is carried by blood to various systemic tissues. The targets of Cr distribution include the lymph nodes, spleen, liver, kidney, and heart wall (Zeidler-Erdely et al. 2008). Cr^{3+} is an essential nutrient to glucose, protein, and fat metabolism. The higher redox potential of Cr^{6+} and its ability to penetrate the cell membranes gives it a greater toxic potency (Zatka 1985). Consequently, the reduction of Cr^{6+} to Cr^{3+} or even Cr^{0} could limit the toxicity of welding fume particles.

Inhalation carcinogenesis of Ni has not been well studied, mainly due to the poor sensitivity of current analytical methods for Ni and its compounds (ATSDR 2005). In contrast to Cr^{6+}, studies found Ni exposure was most likely associated with non-respiratory tract cancers, such as stomach and bone cancer (Mayer et al. 1998; Kasprzak et al. 2003; Oller et al. 2008). IARC classified metallic Ni as a possible human carcinogen, while other Ni compounds were classified as human carcinogens (IARC

1990). In this case, insulating Ni to prevent the formation of Ni compounds will reduce the carcinogenicity of welding fume particles.

The site of action of Mn is in the brain due to its neurological toxin nature (Keane et al. 2010). Consequently, the distribution of Mn to the brain is critical for its toxicity (ATSDR 2008b). The absorption of Mn mainly depends on the welding fume particle size (Antonini et al. 2011). Small size particles deposit in the deeper airways, get absorbed in the blood, and are then transported to systemic organs via the bloodstream (Richman et al. 2008). While the blood-brain barrier is a mechanism to limit toxics reaching the central nervous system and the brain (Sriram et al. 2010), particles deposited in the nasal mucosa can be directly transported to the brain (Richman et al. 2008).

Current Control Technologies

These occupational standards pushed the development of Cr^{6+}-free welding technology to ensure welder's health and safety (CDC 2008). There are various ways to mitigate the emission of welding fume particles and reduce fume exposure (Hewitt and Hirst 1993). The most effective methods are still personal protective equipment (PPE) such as respirators (Cho et al. 2011). However, the majority of welders prefer not to wear a respirator as it is bulky and heavy. Although respirators are distributed in industrial facilities, it is not mandatory to do the fitting test and workers are not required to wear the respirators during welding operations.

Metal inert gas (MIG) welding uses shielding gas to protect welds from surrounding atmospheric components such as nitrogen and water. The shielding gas also helps limit the oxidation of metals by lowering penetration of reactive oxygen species (Dennis et al. 1997) and reducing fume generation rates (Ebrahimnia et al.

2009). However, there are numerous types of shielding gases (Antonini et al. 1998), and some combinations of these gases actually could increase ultraviolet (UV) intensity and ozone concentration (Dennis et al. 1997). Shielded metal arc welding (SMAW) uses vapor generated from flux coating to prevent oxidation and to ensure the purity of the weld. It should be emphasized that the purposes of these shielding technologies aimed at expelling oxygen species are to ensure and promote the weld quality, rather than to reduce the toxicity of welding fume.

Local exhaust ventilation (LEV) technology is commercially available to remove welding fumes from welders' breathing zones (Lee et al. 2007; Meeker et al. 2010). However, LEV is inconvenient in outdoor welding, where welders move frequently (Hewitt and Hirst 1993; Flynn and Susi 2012). On-gun extraction was developed to collect welding fume near the welding arc; nevertheless, the current type of extraction gun is bulky and heavy from an operational perspective and less effective in vertical and overhead welding (Wallace et al. 2001; Flynn and Susi 2012). There are also concerns that the suction force of the LEV or on-gun extraction would disturb the flow of the shielding gas, and thus affect the weld quality.

Control technologies targeting Cr^{6+} have also been developed. For example, the addition of reactive metals, such as zinc (Zn) and aluminum (Al), to welding wires can reduce the formation of Cr^{6+} (Dennis et al. 1996). Reducing agents used as shielding gas additives such as methane (C_2H_4) or nitrogen oxide (NO) can reduce ozone formation in the welding fumes and hence limit the formation of Cr^{6+}. Dennis et al.(2002) tested NO and C_2H_4 as shielding gas additives, and found about 50~70% removal efficiencies. However, the flammability of methane and the formation of toxic NO_2 are

potential risks when using the two reducing agents. Carbon monoxide (CO) is also used in the industry as a reducing gas (Jie et al. 2008) to reduce metal oxidation, yet is itself a hazardous air pollutant (HAP). Replacing the Cr content in the stainless steel wire with other materials with identical functions such as ruthenium (Ru) can reduce the amount of Cr in welding fume (Paulson et al. 2011), but this option is limited by the lack of availability of these rare metals.

In summary, there is currently no widely adopted technology conforming to the new occupational standards to mitigate the formation of airborne Cr^{6+} emissions from welding, and which is well received by welders. A technology that can be broadly applied to most welding conditions, well balanced in efficiency and feasibility, is critically needed for the better protection of welders' health and safety, satisfaction of the occupational standards, as well as reduction of medical cost for the society.

Amorphous Silica Encapsulation Technology

Coating an amorphous silica layer on particle surfaces to insulate engineered nanoparticles from degradation from exposure to the surrounding environment has been reported in various studies (Liz-Marzán et al. 1996; Biswas et al. 1997; Correa-Duarte et al. 1998; Yi et al. 2005; Teleki et al. 2009). Amorphous silica encapsulation (ASE) technology has been demonstrated to be an effective measure to control nano-sized metal particles and to reduce the environmental pollution from combustion system and incinerators (Biswas et al. 1995; McMillin et al. 1996; Owens and Biswas 1996; Biswas et al. 1997; Biswas and Wu 1998). The process is conceptually illustrated in Figure 1. Silica precursor injected into the high temperature zone reacts with reactive oxygen species, hence limiting the oxidation of metals. Silica coating is achieved through the condensation of *in-situ* generated amorphous silica onto metal particles. The

amorphous silica layer insulates the metal species from human organisms when inhaled. Silica formed from reaction also effectively increases the size of particles in the system. The two-fold approach of limiting oxidation potential and coating metal particles in an amorphous silica layer goes beyond previous control technologies by addressing all the toxic metals regardless of their oxidation state.

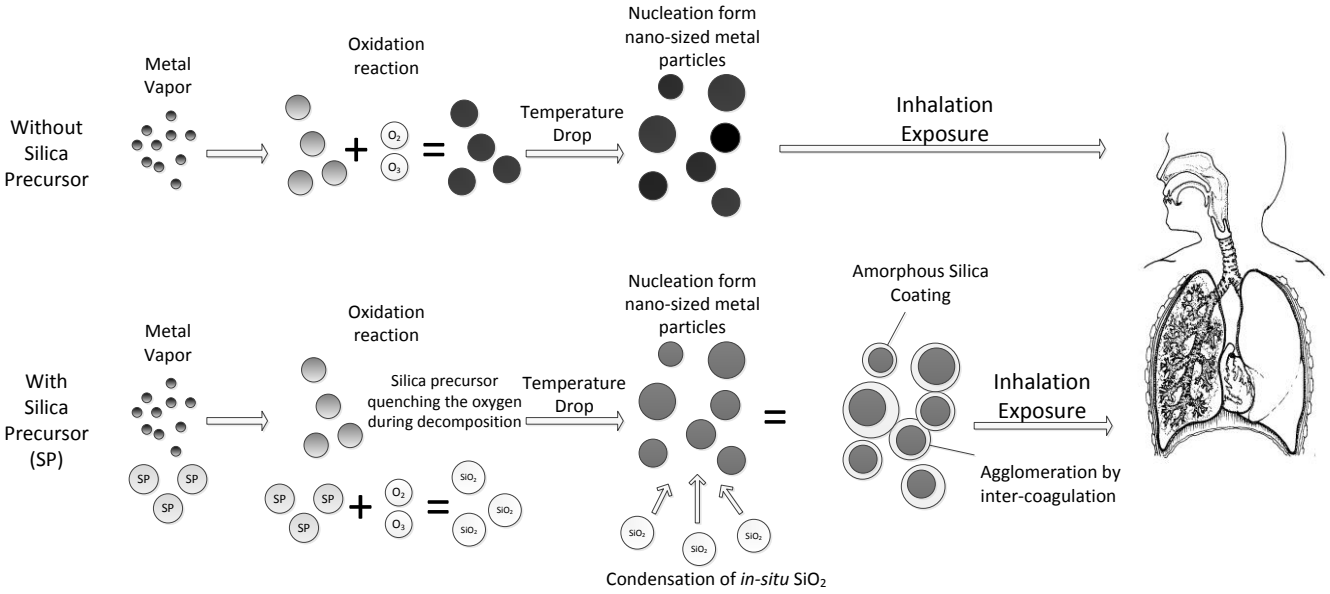

Figure 1-1. Mechanistic illustration of the ASE technology

Initial proof-of-concept demonstration of the amorphous silica encapsulation technology applied to welding has been successfully achieved in the preliminary experiments (Topham et al. 2010; Topham et al. 2011; Yu et al. 2011). Vapor phase silica precursor tetramethylsilane (TMS) was added to shielding gas and decomposed at the welding arc zone. TMS reacted with the oxygen species to form silica, hence limiting the oxidation of Cr. *In-situ* generated silica then condensed on metal particles to form an amorphous silica coating, which was observed in the TEM images. However, the initial success of the ASE technology is also constrained to specific operating

conditions. Expanding this technology to a wide range of welding operations is critical to its practical application. More importantly, the assessment of the change of welding fume particles' physical, chemical, and toxicological properties due to silica precursor is necessary to demonstrate the effectiveness of this technology.

Analysis of Silica Encapsulation

Bioavailable fraction of the welding fume particle is the toxicants dissolved and absorbed, thus enters the systematic circulation. The silica layer on the welding fume particles can effectively prevent the toxic metals from being bioavailable. Quantifying the coating efficiency of silica layer on the metal particles, i.e. the fraction of metals encapsulated that is not bioavailable, is essential for assessing the ASE technology, as well as other silica-metal core-shell structure particle synthesis or control technology. The traditional methods to examine the silica encapsulation on particles were to visualize the particles using either Scanning Electron Microscopy (SEM) or Transmission Electron Microscopy (TEM). However, due to the two-dimensional nature of microscopic image, metal appears to be encapsulated in the images could be non-, partially or fully encapsulated or even enriched on silica surface (Maynard et al. 2004), in a three-dimensional space. In addition, the microscopic images can only portray a portion of the particles on the microscope grid. Whether the images can represent the real conditions of the silica encapsulation have always been questioned.

Silica is immune to most acid attacks except hydrofluoric acid (HF) (Xu et al. 2005). Nitric acid or aqua regia is a common acid to dissolve metals in the environmental samples (Dulski 1996; Myöhänen et al. 2002). By using different digestion acids with different levels of abilities to dissolve silica, the amount of metals encapsulated inside the silica shell can be calculated.

Research Goals

The hypotheses of this doctoral research are: (1) the proportion of the metals encapsulated inside the silica layer can be quantified with different digestion methods; (2) insulating the flow of the silica precursor from the other shielding gas flow should be able to eliminate premature decomposition of the silica precursor, thus further reducing Cr^{6+} and improving the SCEs compared to the pre-mixed mode; (3) the ASE technology will not noticeably change the cost and the mechanical qualities of the product compared to the conventional welding process.

To prove the hypothesis, a quantitative method to determine the proportion of metals encapsulated inside the amorphous silica shell was first developed, using HNO_3/HF mixture and aqua regia. To overcome the premature decomposition of silica precursor, an insulated double shroud torch (IDST) was designed and tested for Cr^{6+} reduction, as well as silica encapsulation efficiency (SCE) using the newly developed quantitative method. During the study, the impacts of this technology on industrial cost, hazard, and weld quality were examined, and compared to the baseline condition.

Success of the demonstration of the ASE technology in welding will bring great health and safety benefits to welders, currently estimated to be 466,400 in United States (BLS 2008), as well as reduce tremendous medical cost associated with the toxic welding fume exposure.

CHAPTER 2
DETERMINATION OF SILICA COATING EFFICIENCY ON METAL PARTICLES USING MULTIPLE DIGESTION METHODS

Objective

Metal particles, including both elemental and oxidized metals, are commonly found in industrial systems such as coal combustor (Biswas et al. 1995), incinerator (Chen et al. 1999), furnace (Gullett and Raghunathan 2002), boiler (Frederick et al. 2004), engine (Kittelson et al. 2006), and other high temperature processes involving metals including arc welding (Zimmer and Biswas 2001). These metals vaporize at the flame/arc zone, and then quickly nucleate and condense to form nano-sized particles as temperature drops, due to the sharp decrease of their saturation vapor pressure (Sethi and Biswas 1990). Those nano-sized metal particles are respirable and able to travel deep within the lung (Oberdörster et al. 2007). Compared to their larger size counterparts, nano-sized particles are more likely to penetrate tissues and cannot be easily removed from human body (Biswas and Wu 2005). The presence of toxic metal particles in the ambient and occupational environment has led to a rapid development of various control techniques. However, traditional emission control technologies exhibit less effectiveness for nano-sized metal particles (Kim et al. 2007). The tightening of emission standards and occupational exposure limits requires development of next generation control technologies for nano-sized metal particles.

The toxicity of metal particles is mainly decided by their surface composition that is in contact with tissues rather than their bulk composition. A novel amorphous silica encapsulation (ASE) technology was recently developed to control nano-sized metal particles and to reduce their toxicity. Silica coating was achieved through the condensation of in-situ generated amorphous silica onto metal particles (McMillin et al.

1996; Biswas et al. 1997; Biswas and Zachariah 1997). The ASE technology had been demonstrated in several studies of controlling metal particles in flue gas of combustion system (Biswas et al. 1995; McMillin et al. 1996; Owens and Biswas 1996; Biswas et al. 1997; Biswas and Zachariah 1997; Biswas and Wu 1998; 2005). Amorphous silica has a low solubility in water (Iler 1979) and is relatively non-toxic compared to metals such as chromium (Cr), manganese (Mn) and nickel (Ni). Hence, amorphous silica coating outside the metal cores has the potential advantage of changing the biotoxicity of metal particles (Yu et al. 2011). Recent studies applied this technique to gas tungsten arc welding (GTAW) (Topham et al. 2010) and gas metal arc welding (GMAW) (Topham et al. 2011), from which the formed welding fume mainly consisted of nano-sized metal particles. The transmission electron microscopy (TEM) image of fume particles formed with the addition of silica precursor showed some silica shell/metal core particles. However, the silica coating was not present on all the metal particles due to the heterogeneous reaction existing in the welding fume formation. Moreover, different levels of silica coating were found under different shielding gas flow rates. Silica particles alone and uncoated metal particles were also observed in the low shielding gas flow condition. Visual examination by TEM only focused on a small fraction of the fume particles and cannot be used to quantitatively determine the silica coating efficiency in bulk scale.

Since silica coating efficiency (SCE) is critical in the silica encapsulation technique, it is necessary to quantify the coating efficiency of silica on metal particles, i.e. the fraction of metals encapsulated inside silica coating that is not bioavailable. Besides metal emission control, it should be noted that silica encapsulation has wide

applications in nanotechnology, e.g. to modify the surface function of metal particles (McMillin et al. 1996; Biswas et al. 1997; Hall et al. 1999; Fu et al. 2006; Guo et al. 2010; Niitsoo and Couzis 2011). Hence, determination of silica coating efficiencies is important to evaluate the functionality of silica coating in those cases.

Among the analytical systems which can determine the elemental composition of particles, Inductively Coupled Plasma - Atomic Emission Spectroscopy (ICP-AES) is a recognized, versatile analytical instrument for its low detection limit, large dynamic range, and capability of simultaneous analysis of multiple elementals (Wu et al. 1996). ICP-AES operates on the principle of atomic emission by atoms ionized in argon plasma flame. Light of specific wavelengths is emitted as electrons return to the ground state of the ionized elements and makes it possible to quantitatively identify the species present in the solution (Atanassova et al. 1998). Comparing to Graphite Furnace - Atomic Absorption Spectrometry (GF-AAS) and Proton Induced X-ray Emission (PIXE), ICP-AES has the equivalent detection limit but less matrix effect (Rubio et al. 1984; Menzel et al. 2002). It costs much less than Inductively Coupled Plasma - Mass Spectroscopy (ICP-MS) (Webb et al. 2005). All the above make ICP-AES an inexpensive and relatively accurate way to determine the total metals (Boevski et al. 2000). However, metal particle samples need to be treated in order to transfer metal analyte from solid phase into liquid solutions. The common practice is to mix particle phase metals with strong acids and dissolve metals in a temperature controlled environment. The digests are diluted to an acceptable total dissolved solids (TDS) concentration for ICP-AES analysis.

Several digestion methods have been reported effective to dissolve metal particles (Lamble and Hill 1998; Sandroni et al. 2003; Okorie et al. 2010). Different digestion methods have varied metal recovery efficiencies. Nitric digestion alone is generally effective for most metals. For certain metals like copper (Cu), recovery efficiency can be greatly promoted by adding hydrofluoric acid (HF) (Ikävalko et al. 1999). HF is also commonly employed in digestion of solid samples containing both organic and inorganic silicon (Xu et al. 2005). The main concerns for the use of HF are corrosion to silica parts in the instrument and hazards of exposure to the operators. This risk can be minimized by adding a stoichiometric amount of boric acid (H_3BO_3) into the complex after digestion. Digestion with aqua regia is also a common method for the determination of trace elements in soils and sediments (Myöhänen et al. 2002). Aqua regia is a mixture of nitric acid (HNO_3) and hydrochloric acid (HCl) in a volume ratio of 1:3. There is almost no common metal that can survive the acid attack of aqua regia (Dulski 1996). Other acids such as sulfuric acid and phosphoric acid were also mentioned in some studies (Wu et al. 1996; Xu et al. 2005). Heating block, ultra-sound assisted and microwave digestions were used to provide a high energetic environment to assist strong acid attack (Kuss 1992; Filgueiras et al. 2000). Among those methods, microwave digestion is highly recommended in determination of trace metals with the advantages of fast decomposition rate, less volatile loss, less contamination, precise temperature and pressure control. It requires less acid and therefore can lower the method detection limit (Lamble and Hill 1998).

The objective of this chapter was to develop a method for determining silica coating efficiency on metal particles generated from the ASE technology. Silica coated

metal particles were generated using gas metal arc welding (GMAW) with a silica precursor. The fume particles from the process mainly contained Fe, Cr, Ni, Mn, and Cu. Metal recovery efficiencies of three digestion acid mixtures were compared. Silica coating efficiencies were calculated by the apparent concentration differences between digestion methods which can effectively dissolve silica coated metal particles and which can only dissolve metals.

Experimental Methods

Sample Preparation

A GMAW welding machine (Lincoln 140C) was used for generating welding fume particles using ER 308L stainless steel welding wires. Figure 2-1 shows the schema of the fume production and sampling system. The GMAW welding fume particles primarily come from the welding wire (Castner and Null 1998). The 308L welding wire nominally contains 20% Cr, 10% Ni, 1.7% Mn, 0.03% Cu, and balanced with Fe (Vitek and David 1987). Silica coated particles were generated by adding tetramethylsilane (TMS) as the silica precursor. Argon and carbon dioxide mixture (3:1, v/v), which is commonly used for stainless steel GMAW, was employed as the shielding gas in this study. A fraction of the shielding gas was used as the carrier gas for the TMS vapor. Injected TMS decomposed at the high temperature welding arc zone to form an amorphous silica coating on welding fume particles. The particles thus generated were then collected onto glass fiber filter (Whatman 90 mm), weighed and digested. Previous study showed the higher shielding gas flow rate, the more silica coating observed (Topham et al. 2011). Hence, three welding conditions were selected to represent the low, medium, and high shielding gas flow conditions studied previously. The operating parameters of

different welding conditions are listed in Table 2-1. Sampling under each condition was carried out at least four times.

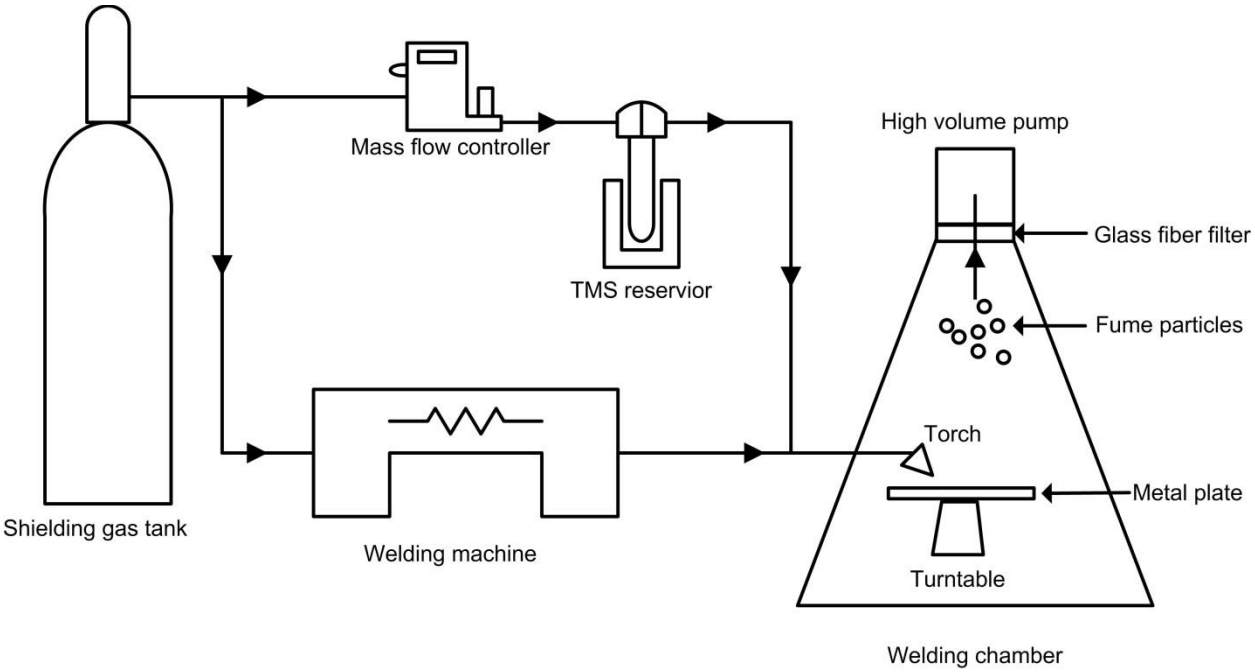

Figure 2-1. Schematic diagram for the sampling system

Table 2-1. Welding parameters and silica coating efficiencies under different welding conditions

Welding condition	Primary shielding gas flow rate (Lpm)	TMS carrier gas flow rate (Lpm)	Silica coating efficiency ±SD (n)
1	30	2.8	38.67% ± 6.76% (5)
2	25	2.1	25.76% ± 4.21% (4)
3	20	2.1	13.82% ± 3.79% (5)

Instrumentation and Chemical Reagents

Analysis of total metals was carried out by an ICP-AES system (Perkin-Elmer Plasma 3200). The system is equipped with a plasma torch with an alumina injector which enables measurement of the samples with HF. Two monochromators covering the spectral range of 165-785 nm with a grated ruling of 3600 lines/mm are included in the system. The system also contains a crossflow nebulizer, a spray chamber, and a Gilson four-channel peristaltic pump. The system is capable of analyzing metals in

digest solution with a detection limit range of less than part per million (ppm). The operating conditions for the ICP-AES are listed in Table 2-2.

Table 2-2. Operation conditions of Plasma 3200 ICP-AES

Incident Power (W)	1300
Plasma gas flow rate (Lpm)	13
Auxiliary gas flow rate (Lpm)	0.5
Nebulizer gas flow rate (Lpm)	0.8
Peristaltic pump flow rate (mL min^{-1})	1
Reading delay time (s)	40
Reading per sample	5 replicates

The metals analyzed by ICP-AES included Fe, Cu, Cr, Ni, and Mn. Two atomic emission spectral lines for each element were used simultaneously to reduce spectral interference introduced by other co-existing elements in the matrix. The wavelengths of their spectral lines are listed in Table 2-3. The concentration of each metal in a sample was determined by averaging the results of five reading replicates. A single calibration curve was constructed for each metal with six aqueous standards. The concentration ranges of calibration solutions were 10–100 mg L^{-1} for Fe and 1–60 mg L^{-1} for Cr, Ni, Mn, and Cu. All the calibration plots were linear in the investigated concentration ranges with the correlation coefficients greater than 0.999. Blank samples were used to determine the method detection limits of different digestion methods. Standard samples were randomly inserted into sample queue to test the bias after a relatively long period of running ICP-AES.

The mass of collected samples were measured by an analytical scale (Sartorius MC210S) with a readability of 10 µg. Each batch of samples was weighed three times and the mean value was calculated. Transmission electron microscopy (TEM, JEOL 2010F) was used to acquire visual evidence of silica coating on welding fume particles.

The fume particles were loaded onto a specialty TEM grids (Pelco Lacey Carbon Type-A 300 mesh) inserted into the welding chamber.

Table 2-3. Wavelength of spectral lines (nm) and method detection limit (mg L^{-1}) for each metal in this study

Metal	Wavelengths (interference metals (McLaren and Berman 1985)*)	Method detection limit by digestion acid mixture		
		HNO_3 alone	HNO_3/HF mixture	Aqua regia
Fe	238.204, 259.940,	0.49	0.32	0.36
Cr	205.552 (Fe, Mo), 267.716 (Mn, V)	0.28	0.33	0.29
Ni	231.604, 221.647	1.66	0.57	0.48
Mn	257.610 (Fe, Cr), 293.306 (Fe, Al)	0.66	0.47	0.85
Cu	324.754, 327.396	0.78	0.36	0.54

All chemicals used were analytical grade or higher purity. Calibration curve was obtained from external standard. Standard solutions were prepared by diluting high purity stock solutions with deionized (DI) water: 10 g L^{-1} Fe and 100 mg L^{-1} Cu (Fisher Scientific), 1000 mg L^{-1} Ni and 1000 mg L^{-1} Mn (Spex Certiprep). Cr standard was in the form of 1000 mg L^{-1} chromate (CrO_4^{2-}) (Acros Organics) and thus conversion was necessary to get the Cr concentration.

$$[\mathrm{Cr}] = [\mathrm{CrO_4^{2-}}]\frac{51.996\ \mathrm{g/mol}}{115.992\ \mathrm{g/mol}} \qquad 2\text{-}1$$

All acid solutions (Fisher Scientific), HNO_3, HF, and HCl were at their original concentration and not diluted. Boric acid (H_3BO_3) (Acros Organics) was obtained in solid phase. Water used for dilution and cleaning was deionized by a water purification system (Barnstead Nanopure II) to a final conductivity of 18.2 mΩ-cm.

Labwares were cleaned before and after analysis to prevent exposure to potential residual contamination during the whole period of experiments. Polytetrafluoroethylene (PTFE) tubes with screw caps (VWR) were used as the

digestion vessel to eliminate the risk of HF to glassware. Screw caps can prevent the vaporization of analyte and environmental contamination. All glassware and PTFE tubes were rinsed by DI water, immersed in nitric acid bath (3M HNO_3) for at least 72 h, cleaned in an ultrasonic cleaner (FS220) for 4 h, and dried in an oven (230G Isotemp) in a laminar flow hood. To further minimize the memory effect of any acid employed in this study, each PTFE tube was labeled and fixed to a specific digestion method, e.g., the tube used for HNO_3 alone and aqua regia would not contact with HF under any circumstances.

Digestion Process

Digestion was assisted by using a microwave digesting system (CEM MDS 81D). An 8-step microwave heating procedure was designed according to the review of experiments done on metal digestion (Lamble and Hill 1998) and is listed in Table 2-4. The sample digests were cooled and filtered by ashless filter (Whatman 32 mm) to remove the solid residues. The filtered digests were diluted to 50 mL with 2% HNO_3 added. The diluted solutions were analyzed by ICP-AES immediately after dilution.

Table 2-4. Operating programs of CEM MDS-81D microwave digesting system

Increment	Power (W)	Duration (s)
1	250	120
2	400	120
3	500	600
4	250	480
5	400	240
6	600	360
7	0	120
8	300	180

The basic principle of the digestion process is to utilize HNO_3, HCl, and HF acid to solubilize the metal particles. HNO_3 alone method and aqua regia method were

adopted to determine the most aggressive acid mixture without breaking the silica coating on metal particles. The particle-loaded filters were cut to quarters after weighing. Each quarter was digested with different acid mixtures. The homogenous mass distribution of metal particles on the filter was examined to avoid interference from mass difference among filter quarters.

HNO_3 alone: Filter samples were placed in the PTFE vessels with 10 mL of HNO_3 added to each vessel. The screw caps on the vessels were tightened to prevent loss during digestion.

HNO_3/HF mixture: HF involved digestion method was based on EPA method 3052 (E.P.A. 1996) to completely dissolve the metals and silica coating. Filter samples were placed in the PTFE vessels with 9 mL of HNO_3 and 1 mL of HF added to each vessel. After the microwave digestion, a stoichiometric amount of H_3BO_3 was added to eliminate the free fluoride ion in order to prevent damage to the ICP-AES sample loops. The amount of H_3BO_3 was calculated based on the following chemical reaction.

$$H_3BO_3 + 4HF \rightarrow HBF_4 + 3H_2O \qquad 2\text{-}2$$

Aqua Regia: Aqua regia (HNO_3:HCl, 1:3, v/v) digestion method was based on ISO standard 11466 (ISO 1995). Filter samples were placed in the PTFE vessels with 7.5 mL of HCl and 2.5 mL of HNO_3 added to each vessel.

All the acid mixtures were placed at room temperature for 10 h before sent to the microwave digesting system.

Method Detection Limit and Recovery Efficiency

Blank filters were digested and used as lab blanks to determine the background level of metals. Method detection limit is defined as 3 times standard deviations of metal

concentration in lab blank (IUPAC 1997). Relative standard deviation (RSD) was calculated among metals and digestion methods.

The metal recovery efficiency σ was calculated to determine the capacity of each digestion method. Pure metal powders (Acros Organics) were weighed and spiked onto blank glass fiber filters. Measured and known mass of spike samples were compared to calculate the metal recovery efficiency by the following equation.

$$\sigma = \frac{C_{measured}}{C_{Spiked}} \times 100\% \qquad 2\text{-}3$$

Metal ratios in spiked samples were kept nearly constant and similar to the metal particles generated from the welding process. The spiked samples were digested and analyzed using the same methods as the generated particles. *t*-test was used in comparison of metal recovery efficiency for different digestion methods.

Results and Discussion

Method Detection Limit

Method detection limits determined from laboratory blanks are shown in Table 2-3. Detection limits of five metals in this study were generally around 1 mg L^{-1} level. Based on the results, the choice among different digestion methods had little influence on the method detection limit since the metal concentration in this study is much higher than 1 mg L^{-1}. The HNO_3 alone digestion method shows a slightly higher detection limit for Ni and Cu than the other two methods. However, the method detection limits hereby were limited by the instrument (ICP-AES) and trace metal impurity levels of the glass fiber filter. The detection limit could be significantly decreased if analyzed by ICP-MS though it costs more and the procedures are more complicated. The silica shell/metal core structure particles are always synthesized in bulk volume and likely tests will not be

carried out for a minute amount of particles. Hence, high resolution (lower than 1 ng L^{-1}) is not necessary in most cases. Glass fiber filter was used in this study because it has good resistance to high temperature generated by welding and it can handle the high flow rate generated by the high-volume sampling pump. Since the trace metal level in glass fibers was much less than the collected metal mass, its impact on method detection limit is not critical to the concentration measurement. In applications where high temperature and high flow rate are not encountered, alternative filters such as cellulose and membrane filters could be used to reduce the trace metal impurities (Dams et al. 1972; Scott et al. 1976; Sievering et al. 1978). Filters are not necessary if the particles can be transferred to digestion vessel without being collected on filters.

In the experiment, metal matrix effect and HF memory effect could also interfere with the resolution and affect the detection limit (Tan and Horlick 1987; Todoli et al. 2002; Xu et al. 2005). Carefully acid washing the vessels after the experiment could also lower the detection limit by removing possible residual contaminations.

Metal Recovery Efficiency

Figure 2-2 shows the recovery efficiencies for different digestion methods and different metals. For all the elements and methods, the recovery efficiencies ranged from 90-110%. Recovery efficiencies of HNO_3/HF mixture for all metals except Cu are close to 100% and statistically they are significantly different from the other two methods (p<0.05). Cu has the highest average recovery efficiency of 103.7%. Metal recovery efficiencies over 100% can be attributed to the filter impurity level, e.g., glass fiber filter generally has 3 ng/cm^2 of Cu (Scott et al. 1976). The selection of wavelengths of Cr and Mn cannot avoid the spectral inferences from Fe as shown in Table 3. Overestimation of Cr and Mn could happen due to spectral effect induced by high

concentration of Fe in the welding fume particles. In addition, non-spectral matrix effect of ICP-AES could either enhance or depress the signals for those metals (Todoli et al. 2002).

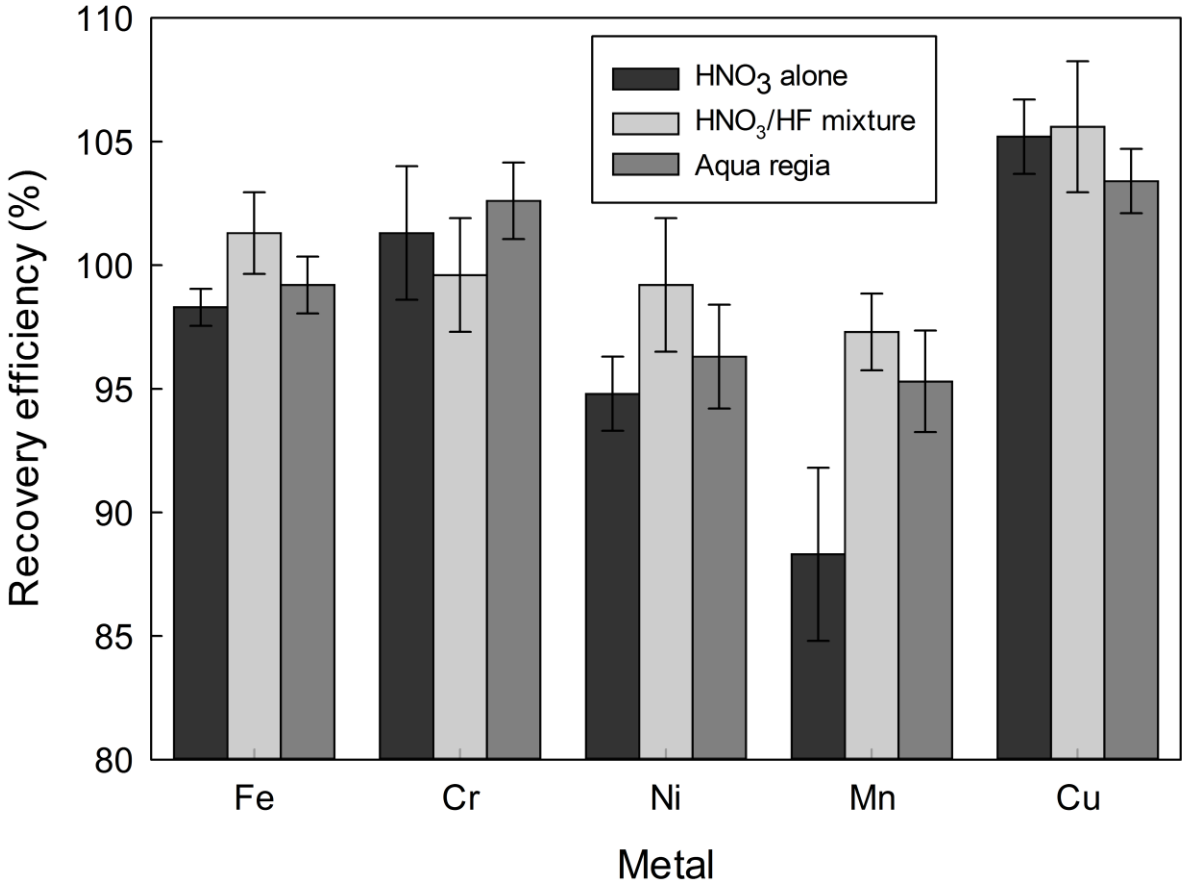

Figure 2-2. Recovery efficiencies for Fe, Cr, Ni, Mn, Cu by different digestion acid

The RSD for each metal in different methods was less than 3.5%. Except for Cr, HNO_3/HF mixture showed the highest mean recovery efficiencies compared to the other two acid mixtures (p<0.05). Aqua regia was higher than HNO_3 alone for Mn (p<0.05), but no significant difference was found on other metals. HNO_3 alone showed a low recovery efficiency of 88.3% for Mn and a relatively high deviation. This represents the relatively low acid attack ability by HNO_3 alone. Hence, aqua regia was adopted instead

of HNO_3 acid alone in the following silica coating efficiency test to have a comparison with HNO_3/HF mixture. However, mixture of HCl and HNO_3 requires a well-sealed vessel such as PTFE tube due to the formation of highly evaporative gas phase NOCl and Cl_2. HNO_3 alone could be an alternative if the sealant cannot be perfectly achieved. In this study, the recovery efficiency test was done using elemental metals, while in real applications such as flame synthesis or welding fume, metal oxides could dominate the particle compositions. Differences in their solubilities should be checked. However, the differences can be neglected in high energy environment provided by the microwave digestion system (Nadkarni 1984).

Silica Coating Efficiency

Figure 2-3 shows the TEM imagery of fume particles collected at welding condition 1. Metal particles are darker while silica is in light color, due to the penetration ability of electron when interacting with the particles.

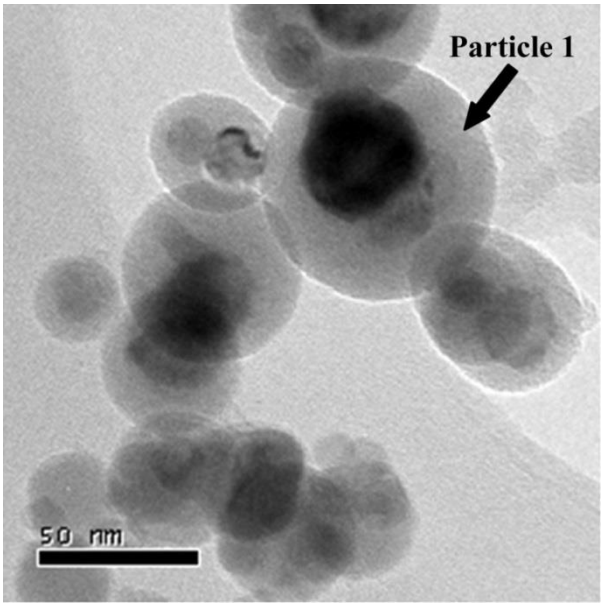

Figure 2-3. TEM imaginary of welding fume particles with silica coating

In the TEM image, some particles (e.g., Particle 1) have a high electron density (darker) region surrounded by a low electron density region (lighter). This is likely the result of metal encapsulated by silica coating layer. Nonetheless, due to the two-dimensional nature of TEM image, metal in particle 1 could be non-, partially or fully encapsulated or even enriched on silica surface (Maynard et al. 2004), in a three-dimensional space. To truly determine the level of encapsulation, the silica coating efficiency would be critically important.

HNO_3/HF mixture breaks the silica coating on the metal particles, and according to the metal recovery efficiencies results it had the most aggressive solubilization ability. Aqua regia showed the similar digestion ability on metal-only particles but did not have any effect on particles with silica coating. The mass difference between the results obtained from these two digestion methods was therefore used to calculate the silica coating efficiency using the following equation.

$$\eta = \frac{\sum_{i=1}^{N} C_{NF,i} - \sum_{i=1}^{N} C_{AR,i}}{\sum_{i=1}^{N} C_{NF,i}} \times 100\% \qquad 2\text{-}4$$

where η: Silica coating efficiency, %

N: Number of metals involved

$C_{NF,i}$: Measured concentration of the i^{th} metal digested by HNO_3/HF mixture

$C_{AR,i}$: Measured concentration of the i^{th} metal digested by aqua regia

Silica coating efficiency η represents the ratio of metals inside the silica coating, which could not be dissolved by aqua regia. It should be noted that the silica coating efficiency for individual metal can be calculated through this equation without summation. However, due to the heterogeneous interaction between silica and metal in this study, the coating process is not targeting at any specific metal. Hence, the silica coating efficiency for individual metal was not calculated. $C_{AR,i}$ can be replaced with metal concentration measured by other acid digestion methods when appropriate, e.g.,

HNO_3 acid alone without Mn in the system. For specific applications, some rare metals such as Ru, Ta, Os, and Rh can withstand common acid attack such as aqua regia (Craig and Anderson 1995). Under such a circumstance, the equation is not capable of handling those rare metals.

Silica coating efficiencies were acquired from three sets of samples generated under different welding conditions. Mean value and standard deviation of metal concentration were obtained for all the samples and are shown in Table 2-5. This shows a relatively consistent welding fume particle composition during the experiment. Cu was not detected at most conditions because of the relatively small proportion of Cu in welding wire. The presence of Cu in some of the samples was likely the ablation of welding nozzle tip and shell, rather than the wire. In the samples where Cu was detected, concentration of Cu was close to the method detection limit. Except Cu, other metals showed a good agreement among replicas (RSD <14%).

Table 2-5. Measured concentrations (mg L^{-1}) of metal elements digested by different acid mixtures

Metals	Welding Condition 1 (n=5)	Welding Condition 2 (n=4)	Welding Condition 3 (n=5)
$C_{NF, Fe}$	56.34 (1.13)*	78.79 (8.67)	63.51 (1.91)
$C_{AR, Fe}$	33.28 (3.00)	51.79 (2.07)	59.38 (3.56)
$C_{NF, Cr}$	31.02 (1.55)	45.45 (1.36)	37.19 (2.98)
$C_{AR, Ct}$	28.13 (2.79)	31.33 (2.19)	28.56 (1.71)
$C_{NF, Ni}$	12.82 (0.38)	20.15 (0.81)	13.41 (0.54)
$C_{AR, Ni}$	n.d.**	17.43 (1.57)	14.82 (1.78)
$C_{NF, Mn}$	19.73 (0.99)	20.92 (0.84)	17.65 (1.24)
$C_{AR, Mn}$	14.05 (1.83)	22.17 (3.10)	12.33 (1.11)
$C_{NF, Cu}$	3.12 (1.03)	n.d.	1.78 (0.33)
$C_{AR, Cu}$	n.d.	n.d.	n.d.

* Number in the parentheses indicated the standard deviation among sample replicates
** n.d. Not detected in the samples or lower than method detection limit.

Results of Mn in welding condition 2 and Ni in welding condition 3 suggest more metals have been digested by aqua-regia than HNO_3/HF mixture. These two anomaly values could be attributed by uneven distribution of particles on different quarters of one glass fiber filter.

Based on the metal concentrations acquired and the equation, silica coating efficiencies were calculated and are listed in Table 2-1. As shown, the silica coating efficiencies were generally low (<40%), due to the heterogeneous nature of gaseous reaction between silica precursor and metals. The highest silica coating efficiency occurred under welding condition 1 which had a higher shielding gas flow rate. The higher shielding gas dispersed more heat generated from the welding arc. Examination of the inner shell of welding nozzle showed a large amount of white silica powder deposited under the low shielding gas flow condition. This confirmed that TMS in the low shielding gas flow condition already decomposed before reaching the effective coating position, because heat was quickly transferred to the welding nozzle area resulting information of silica earlier than desired. As shown, the knowledge of silica coating efficiency is very important in understanding the effect of processing conditions (welding parameters) on the process performance (silica coating distribution). By understanding the defect of welding nozzle under low shielding gas flow condition, a new welding torch should be developed to allow insulation from the heat transfer.

The equation based on multiple digestion methods can be used in examining silica coverage of various silica shell/metal core structure particles applications (Ohmori and Matijevic 1992; Liz-Marzán et al. 1996; Correa-Duarte et al. 1998; Lu et al. 2002; Graf et al. 2003; Yi et al. 2005; Teleki et al. 2009). The silica coating efficiencies in

those cases could be an indicator for the effectiveness of the silica shell, e.g., change of functionality, biocompatibility, or colloidal stability by silica shell.

Summary

ICP-AES and microwave digestion were capable for simultaneous analysis of multiple metals down to ~1 mg L^{-1} in this study. The accuracy of results was confirmed by metal recovery efficiencies by different digestion methods. HNO_3/HF acid mixture and aqua regia digestion method were both very effective for treatment of ICP-AES analyte. Major metals (Fe, Mn) and minor metals (Cr, Ni, Cu) in welding particles showed good recovery under those two methods.

The calculation of silica coating efficiencies based on the measured mass difference between two digestion methods quantified the metals sealed inside the silica shell. Five metals were tested in this study based on the composition of stainless steel wires used in metal particles generation. More metal speciation should be examined in the future to verify the method's applicability range. It is also possible to apply this analytical method to applications of silica shell/metal core particles, where high silica coating efficiencies were expected from synthesis based on homogenous reaction but no quantitative confirmation yet.

Metals encapsulated by amorphous silica cannot be further extracted by general acid such as HNO_3 or aqua regia. Hence, silica encapsulation is a promising technique to reduce the biotoxicity of metal compounds in nanoparticles. The experimental result showed silica coating efficiency increased with increasing shielding gas flow rate. The low silica coating efficiency under low shielding gas flow rate was due to the premature decomposition of silica precursors. Modification of welding gun structure to overcome

this shortage likely will improve the silica coating efficiencies under a wide range of flow rates.

CHAPTER 3
DOUBLE SHROUD DELIVERY OF SILICA PRECURSOR TO REDUCE HEXAVALENT CHROMIUM IN WELDING FUME

Objective

The amorphous silica encapsulation (ASE) technology has been shown to be an effective measure for controlling metal nanoparticles emissions from pyroprocesses such as combustors and incinerators (Biswas et al. 1995; Owens and Biswas 1996; Biswas and Zachariah 1997; Biswas and Wu 1998). The use of shielding gas in welding process provides a medium for the introduction of a vapor phase silica precursor. Silica precursor injected through the shielding gas decomposes in the high temperature of the welding arc zone and reacts with reactive oxygen species, hence providing a reducing environment (as shown in Figure 3-1). The in-situ generated silica condenses on the metal particles, and further insulates Cr from oxygen species by forming an amorphous silica layer. An *E.coli* growth experiment demonstrated that in-situ generated amorphous silica has much less biotoxicity than the particles of Cr and other metals (Yu et al. 2011). The byproducts from the decomposition of silica precursor are carbon dioxide and water.

The ASE technology applied to welding was described in previous studies (Topham et al. 2010; Topham et al. 2011; Wang et al. 2011; Yu et al. 2011). A vapor phase silica precursor, tetramethylsilane (TMS), added to the shielding gas reduced Cr^{6+} concentration over 90% under the high primary shielding gas flow rate of 30 liters per minute (Lpm). The inhibition of Cr oxidation was not considerable effective under medium (25 Lpm) and low (20 Lpm) shielding gas flow rates. This ineffectiveness constrains the application to very specific operating conditions. High shielding gas flow

can significantly increase welding operation costs, which would impede the use of the ASE technology in industrial practice.

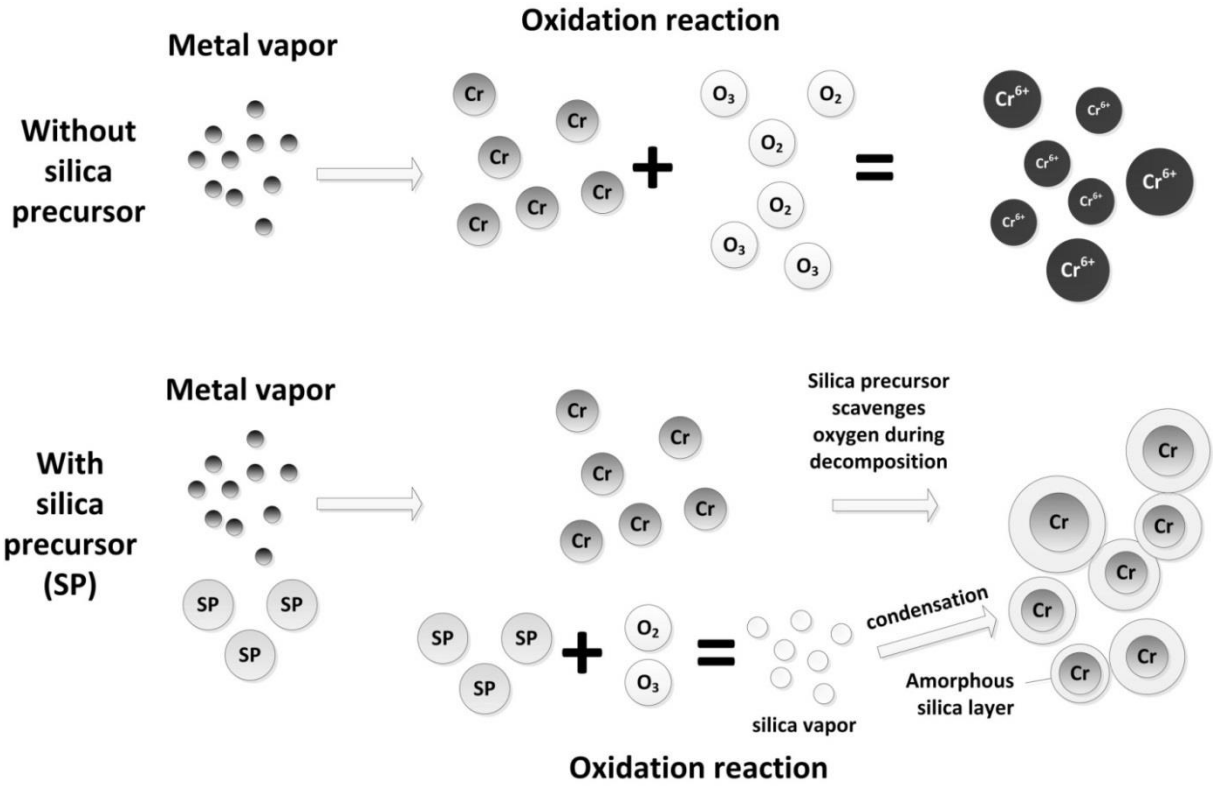

Figure 3-1. Mechanistic illustration of silica precursor for reducing the formation of Cr^{6+}

Medium and low shielding gas flows could not effectively disperse the heat generated from welding process. TMS 'premixed' upstream with the shielding gas, being sensitive to high temperatures, decomposed before reaching the welding arc zone. Furthermore, a large quantity of silica powder was found deposited inside the welding gun under those conditions. A new welding gun design was needed to overcome these problems. Another question to be addressed was that the analytical method (NIOSH 7604)(NIOSH 1994) used in the previous study could not verify the oxidation state of Cr sealed inside the amorphous silica shell formed during the process.

The objective of this chapter was to develop an alternative way to deliver silica precursor effectively into the welding arc zone. A prototype insulated double shroud torch (IDST) was designed to eliminate the premature heat transfer to the TMS. Laboratory experiments were conducted to assess its ability to reduce the Cr^{6+} concentration to below the limit of detection in all shielding gas flow rates. A preliminary field test was carried out in an industrial site to evaluate the ease of implementing this technology. The hazard and cost associated with the technology were also assessed. Success of the reduction of Cr^{6+} generated by stainless steel welding would reduce the carcinogenic risk associated with this industrial process.

Experimental Methods

Injection of Silica Precursor

To avoid the excess thermal energy transferred to the silica precursor, the silica precursor needs to flow separately from the primary shielding gas which is a carrier of heat. Dennis et al.(Dennis et al. 2002) first designed a double shroud torch using two nozzles to introduce the primary shielding gas and secondary shielding gas. However, their torch was designed only for conveniently mixing and switching different gas components. It did not address heat insulation and worked no differently with the silica precursor from the premixing it.

In this study, a new double shroud torch was designed that incorporated a ceramic material to insulate against heat transfer between the primary and secondary shielding gases. Figure 3-2 shows the cross-sectional sketch of the new IDST. The IDST was hypothesized to be able to minimize the premature decomposition of silica precursor by delivering the silica precursor directly to an effective position.

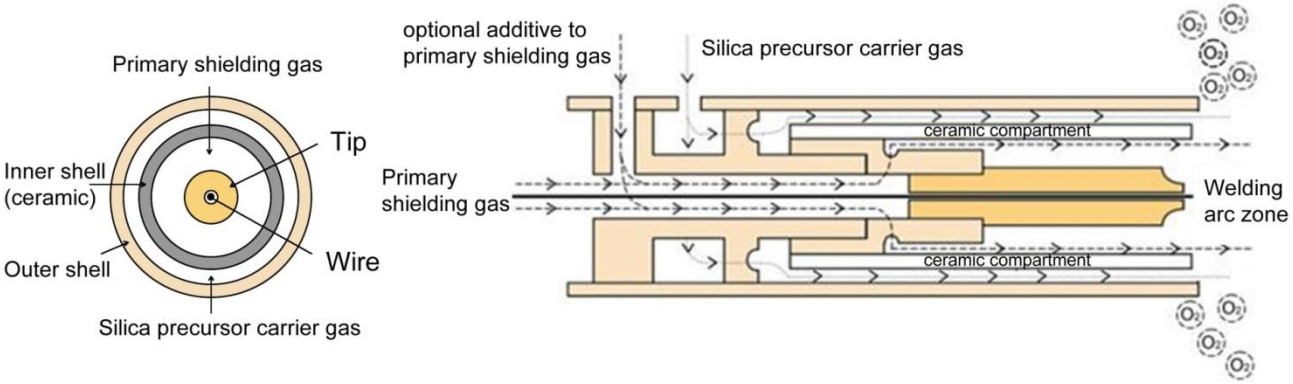

Figure 3-2. Cross-sectional sketch of the insulated double shroud torch (IDST)

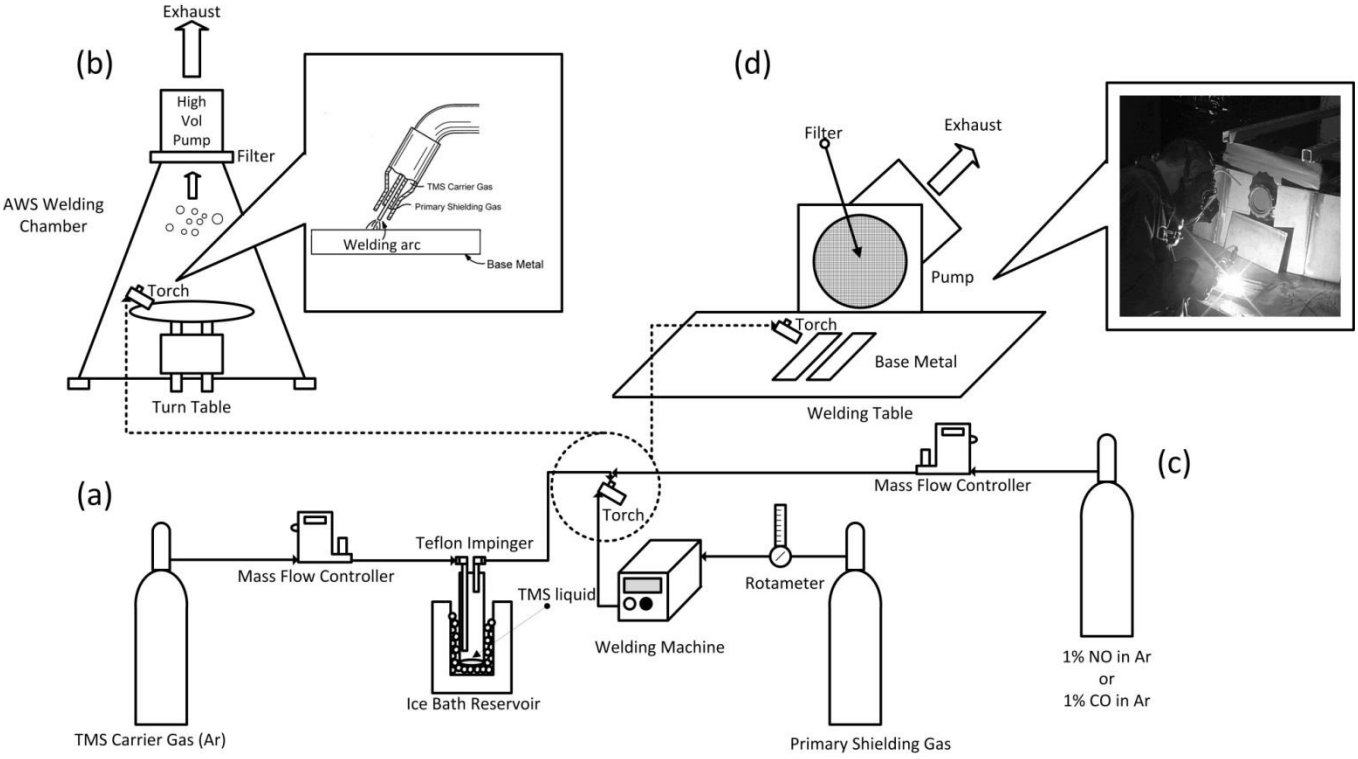

Figure 3-3. Schematic diagram. A) the apparatus for feeding TMS. B) the welding fume chamber with a zoom view at the end of the torch. C) the apparatus for feeding NO or CO. D) the fixed-location sampling system in the field with a picture of the welder performing welding

Traditional welding equipment was modified to introduce the silica precursor TMS into welding shielding gas (Figure 3-3A). TMS carrier gas argon (Ar) flowed through a

Teflon impinger (Apex Instruments T507G) with TMS liquid covering the bottom. The impinger was immersed in an ice bath to lower the TMS vapor pressure which prevented excess TMS vapor from getting in the system. The carrier gas became saturated with TMS vapor, which was delivered to the welding arc zone using the outer shroud of the IDST.

Welding Fume Sampling

Laboratory sampling of welding fumes was performed in an enclosed stainless steel welding chamber shown in Figure 3-3B. The design of the chamber followed the American Welding Society (AWS) F1.2:2006 design.(AWS 2006) The conical chamber measured 36 inches in diameter at the bottom, 8 inches in diameter at the top, and 36 inches in height. A high-volume pump (General Metal Works GL-2000H) with a sampling rate of 50 Lpm was put on top of the chamber. Welding fume particles generated in the chamber were collected on a glass fiber filter (Whatman 90 mm) mounted on the pump.

A welding machine (Lincoln Power MIG 140C) was used in the laboratory study, with a constant voltage of 19.5 V and a wire speed of 100 inches per minute (Ipm) was maintained throughout the study. The study used 0.035 inch diameter 308L stainless steel wire, which has about 20% (wt) Cr. The IDST was kept in a fixed position by a metal stand, and the round shape mild steel base metal was positioned on a constantly rotating turn table (MK Products Aircrafter T-25). The laboratory study simulated beading on the base metal at 1.5 min per sample.

The chamber study used 75% Ar/25% CO_2 as the primary shielding gas, following the welding machine's manufacturer suggestions. Three different flow rates of the primary shielding gas were selected based on previous studies to represent the low,

medium, and high shielding gas flow conditions. Different injection rates of TMS carrier gas were tested, the testing conditions are listed in Table 3-1. The injection rate of TMS carrier gas per each flow rate of the primary shielding gas started at 0.16 Lpm and gradually increased to a percentage of the primary shielding gas that could eliminate the airborne Cr^{6+} concentration to the limit of detection. The flow rates of the primary shielding gas and the TMS carrier gas were respectively controlled by a rotameter (Radnor HRF-1425-580) and a mass flow controller (Omega FMA5500). In addition to the silica precursor, nitric oxide (NO) and carbon monoxide (CO) were also tested during the study as alternative reducing reagents for comparison purposes. A commercial available NO/Ar shielding gas, MISON, consists of 300 ppm (0.03%) NO in Ar. Theoretically, CO can absorb the ultraviolet (UV) light and react with oxygen species to provide a similar reduction. Different percentages of NO or CO in the final shielding gas (Ar) were tested. 1% (v/v) NO or 1% (v/v) CO in Ar were injected as the secondary shielding gas through the IDST (Figure 3c), while pure Ar was used as the primary shielding gas. The testing conditions are listed in Table 3-2. A carbon monoxide monitor (Nighthawks KN-COPP-3) was set near the chamber to determine the CO concentration in the air.

The field sampling was performed in an industrial facility that regularly conducts welding activities. A fixed-location area sampling setup was used in the field as shown in Figure 3d. A certified welder performed the welding task in front of the high-volume pump with the glass fiber filter installed. The sampling period per each sample was extended to 5 minutes arc time to collect enough welding fume for analysis.

Table 3-1. Testing conditions of TMS and shielding gas flows in the chamber sampling

Primary Shielding gas flow rate (Lpm)	TMS Carrier gas flow rate (Lpm)	Percentage of TMS Carrier gas to primary shielding gas flow rate (%)	Estimated TMS concentration in the shielding gas (v/v)
20	0.16	0.8	2.8×10^{-3}
	0.32	1.6	5.6×10^{-3}
	0.64	3.2	1.1×10^{-2}
25	0.16	0.64	2.3×10^{-3}
	0.32	1.3	4.5×10^{-3}
	0.64	2.6	8.9×10^{-3}
	1.3	5.1	1.8×10^{-2}
30	0.16	0.53	1.9×10^{-3}
	0.32	1.1	3.8×10^{-3}
	0.64	2.1	7.4×10^{-3}
	1.3	4.3	1.5×10^{-2}

Table 3-2. Testing conditions of NO/Ar and CO/Ar in the chamber sampling

Primary shielding gas	Injection rate (Lpm)	Secondary shielding gas	Injection rate (Lpm)	Percentage of NO/Ar or CO/Ar
Ar	30	1% (v/v) NO in Ar	0.3	0.01
			0.9	0.03
			3	0.1
		1% (v/v) CO in Ar	0.3	0.01
			0.9	0.03
			3	0.1

A welding machine (Miller Invision 456MP) and a wire feeder (Miller 70 series 24 V wire feeder) were employed in the field sampling. The voltage was controlled by a pulse program with an average of 26 V. 310 stainless steel wire with a diameter of 0.045 inch and 310 stainless steel base metal with a thickness of 3/16 inch were used. The 310 stainless steel typically contains about 25% (wt) Cr. The wire speed was fixed at 192 Ipm. The primary shielding gas used was a mixture of 69% Ar, 31% He, and 1% CO_2. The flow rates of the primary shielding gas and the TMS carrier gas flow were kept constant at 15 Lpm and 0.24 Lpm, respectively.

Analysis of Cr^{6+}

An Ion Chromatography (IC) system (Dionex ICS-1500) was used to analyze Cr^{6+}. The IC was equipped with a cation analytical column (Dionex CS5A) for separating different ions, and a conductivity detector (Dionex DS6) to measure the Cr^{6+} concentration. Sample extraction followed NIOSH Method 7604.(NIOSH 1994) Per manufacturer's specifications for the CS5A column, 5 mM sodium bicarbonate and 1 mM sodium carbonate were chosen as the eluent. The Cr^{6+} content on the glass fiber filter was extracted using 20 mL eluent heated in a water bath to 100 ºC for one hour. The extracted solution was filtered to remove the solid residue in order to protect the ICS-1500 injection loop.

Standard solutions were prepared by diluting 1000 mg/L chromate solution (Acros Organics) with deionized (DI) water, to a range of 1–60 mg/L of Cr^{6+}. The calibration plot was linear in the investigated concentration range with the correlation coefficient larger than 0.9999. The estimated Cr^{6+} concentration (µg/m^3) in the sampled air (C_{cr6+}) was calculated using the following equation.

$$C_{cr6+} = \frac{[Cr^{6+}] \times 20mL}{Q \times t} \qquad 3\text{-}1$$

where $[Cr^{6+}]$ is the concentration (µg/mL) of Cr^{6+} in the 20 mL eluent measured by ICS-1500; Q is the flow rate of the sampling pump, 0.05 m^3/min; t is the sampling time, 1.5 min for the laboratory sampling and 5 min for the field sampling. If $[Cr^{6+}]$ was less than the ICS-1500's limit of detection (about 10 ng/mL), the airborne Cr^{6+} concentration was conservatively assigned the corresponding values of the limit of detection (2.8 µg/m^3 in the lab, 1.1 µg/m^3 in the field).

In previous studies (Topham et al. 2010; Topham et al. 2011; Wang et al. 2011; Yu et al. 2011), some fume particles were encapsulated in the amorphous silica layer generated by the condensation of silica vapor. However, the eluent used in the analytical protocol (5 mM $NaHCO_3$ and 1 mM Na_2CO_3) was not able to dissolve the amorphous silica shell. The use of a strong acid such as hydrofluoric acid (HF) could dissolve the silica shell; however, it could also change the valence state of the original Cr^{6+} as well as damage the instrument. In other words, ion chromatography cannot determine the Cr^{6+} encapsulated in the silica shell. X-ray photoelectron spectroscopy (XPS) is a non-destructive analytical process that could examine the valance state of Cr in the range of the penetration depth of an X-ray. A thin layer of fume particles was scratched down from the glass fiber filter to a silicon substrate. Only samples from one baseline and one optimal injection rate were analyzed. The XPS (Perkin Elmer 5100) gives the intensity as an arbitrary unit (a.u.) for each peak; therefore, the relative ratio of Cr^{6+}/Cr^{3+} was calculated.

Chemical Reagents and Labware

All chemicals used were analytical grade or higher in purity. DI water used for dilution and cleaning was deionized and purified by a Nanopure system (Barnstead Nanopure) to a conductivity of 18.2 mΩ-cm. All the shielding gases used were ultra-high purity and certified by the manufacturers (Airgas, Praxair, and Air Liquide). All the glassware used in the study was cleaned in an ultrasonic cleaner (FS220) for 4 hrs, and dried in an oven (FS230G Isotemp) in a laminar flow hood. The tubings in the sampling system were Polytetrafluoroethylene (PTFE) or Tygon, and air leaking tests were performed regularly.

Hazard and Cost Estimation

TMS is a flammable and volatile liquid (Aston et al. 1941). High concentrations of TMS vapor may cause flash fire or explosions in oxidizing environments. The toxicological properties of TMS to humans have not been fully investigated. However, high temperatures in the welding arc zone are expected to decompose the trace amount of TMS. In this study, the TMS concentration was estimated for a room based on test conditions in the field sampling and a worst case scenario, i.e., all TMS vapor escaped without decomposition and ventilation.

The vapor pressure of TMS was calculated using the Antoine equation, (Aston et al. 1941)

$$\log_{10} V_p = A - \frac{B}{T + C} \qquad 3\text{-}2$$

where A, B, C are 3.97703, 1047.242, -36.057 (unitless), respectively, and T is the temperature of the ice bath (273 K). The ideal gas law was then used to calculate the concentration of TMS in the saturated carrier gas.

The increase in operating costs when using the ASE technology can be a major barrier for industrial implementation. A comprehensive cost assessment of the silica precursor was carried out using a model developed for estimating the welding cost.(Lippold and Frankel 2009) Different scenarios of weld (pipe, butt, and fillet) production were utilized to compare the cost using the general welding technology and the ASE technology. The cost to acquire TMS is $65 per 100 mL and its consumption rate is about 0.02 mL per minute.

Statistics

All the samples were at least quadruplicate (n≥4) per each combination of the primary shielding gas flow rate and the TMS carrier gas flow rate in laboratory. The *t*-test was used to examine the mean concentration of Cr^{6+} under different circumstances. Statistical significance was evaluated using a significance level of p=0.05. All statistical analyses were performed using the statistical software (SAS 9.3).

Results and Discussion

Chamber Sampling Results

Figures 3-4A~4C show the airborne Cr^{6+} concentrations under different combinations of the primary shielding gas and the TMS carrier gas flow rates. In addition to the current results from using the IDST and the limit of detection, the results from a previous study (Topham et al. 2011), in which the TMS carrier gas and the primary shielding gas were premixed via a Y-fitting at the welding gun hose, are illustrated in the figure as well.

The Cr^{6+} concentrations in baseline samples were 25(±5.2) μg/m^3, 35(±4.1) μg/m^3, and 56(±8.9) μg/m^3 for the low, medium, and high primary shielding gas flow rates, respectively. It should be noted that the chamber sampling was a simulation of a continuous welding practice for 1.5 min, and it collected the full stream of welding fumes in an enclosed space. The concentrations measured in the chamber do not directly reflect breathing zone exposure concentrations and cannot be directly compared to the OSHA 8-hr PEL of 5 μg/m^3. The limit of detection of 2.8 μg/m^3 was used as lower reference for the Cr^{6+} reduction. The lower limit of the reduced airborne Cr^{6+}

concentration was assumed to be equal to 2.8 µg/m^3, the previously cited limit of detection in the laboratory study.

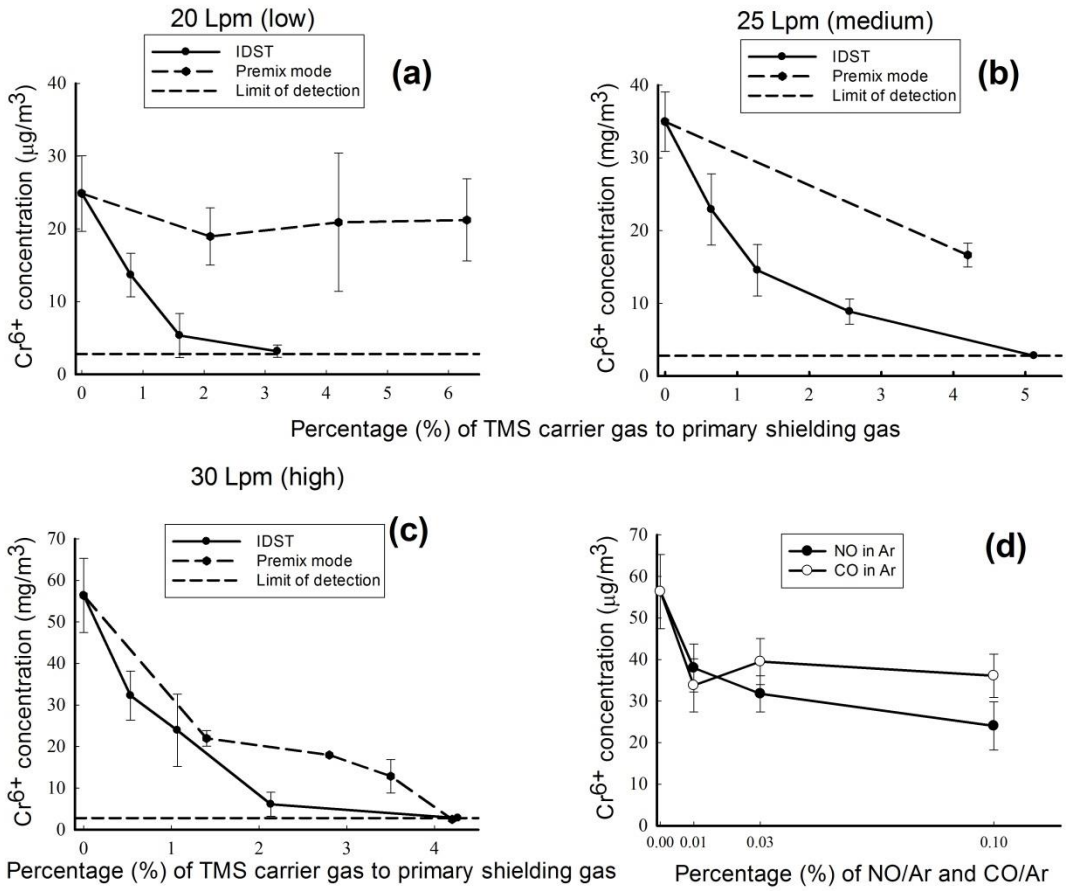

Figure 3-4. Cr^{6+} concentration as a function of TMS carrier gas/primary shielding gas percentage. A) low. B) medium. C) high primary shielding gas flow condition. D) Cr^{6+} concentration as a function of NO/Ar percentage and CO/Ar percentage

Under the low shielding gas flow rate condition (Figure 4a), premixed TMS was unable to reduce the Cr^{6+} (p>0.1) regardless the increase of the percentage of TMS carrier gas to the primary shielding gas over the range studied (up to 6.3% v/v). In contrast, TMS injected by the IDST was able to reduce Cr^{6+} to below the limit of detection (2.8 µg/m^3) at 3.2% TMS gas/primary shielding gas. The percentage was also

less than the needed percentage for the IDST to reduce Cr^{6+} below the limit of detection under the medium and high shielding gas flow rates. In the case of separate flowing of TMS carrier gas and the primary shielding gas, the low flow will create a relatively longer reaction time for the TMS in the welding arc zone, which reduces the ineffective reaction outside the microenvironment.

The medium and high shielding gas flow rates (Figures 3-4B & 3-4C) show similar reduction trends: As more TMS carrier gas was injected, the Cr^{6+} concentration gradually decreased to the limit of detection of 2.8 µg/m^3 (p<0.05 for each conditions). It should be noted that the efficiency of the IDST was always higher than that of premix mode at the same percentage of TMS carrier gas/primary shielding gas. This supports the hypothesis that the IDST could deliver more TMS without premature decomposition than premix mode. Other benefits are that the costs associated with TMS consumption were also reduced and the nozzle showed less silica powder after the IDST experiment. This is direct evidence that the premature reaction of the TMS inside the nozzle that occurred in premix mode was minimized with the IDST.

In summary, the chamber sampling results demonstrated that combining the IDST and the ASE technology could effectively reduce the airborne Cr^{6+} emission over 90%. The positive results prove that the IDST led to a greater Cr^{6+} reduction compared to the original premix mode. It should be noted that the lowest concentrations reported here all corresponded to the limit of detection (2.8 µg/m^3). Hence, the true reduction efficiency might be beyond this conservative estimate.

NO and CO Results

As previously mentioned, NO and CO were intentionally added to the shielding gas to test their reduction of the oxygen species, thus controlling the formation of Cr^{6+}.

Figure 4d shows the results under different percentages of NO and CO in Ar. The mean Cr^{6+} concentration was 24 (±5.8) µg/m^3 when NO was added to the Ar. Compared to the airborne Cr^{6+} concentration of 56 (±8.9) µg/m^3 in the baseline, the difference indicated a mean reduction efficiency of 57%. The maximum reduction occurred at 0.1% of NO, which was much higher than that of the only commercially available NO/Ar shielding gas MISON (0.03% v/v or 300 ppm). A downside of NO is that excess NO may influence the welding arc and lead to mechanical failure of weld (Menzel 2003). Furthermore, the control of NO has to be precise due to a NIOSH REL of 25 ppm for NO (NIOSH 2007) and OSHA PEL of 5 ppm for NO_2 (OSHA 2006c).

There was no statistical difference among Cr^{6+} concentrations with different injection rates of CO (p>0.1). The reduction of the UV intensity and the oxygen species due to CO could only lead to about 35% reduction of Cr^{6+}. The CO monitor also recorded a peak concentration of 100 ppm CO in the air while the percentage of CO in Ar was increased to over 0.1% (v/v), which could be hazardous with prolonged exposure.

Even without the injection of NO, nitrogen oxides (NO_x) can appear in the welding arc zone due to the reaction of ambient oxygen and nitrogen at high temperature. CO_2, the product of reaction between CO and oxygen, can also dissociate to CO at high temperature (>1000 K).(Lavoisier 1984) The thermodynamic equilibrium here inhibited the reaction of NO and CO with the oxygen species. Another reason for the low reduction efficiencies of these gases was that these gases only protected the metal vapor from oxidation near the welding arc zone, while the amorphous silica layer

formed on the metal particles by the ASE technology could insulate the metals from subsequent oxidation occurring outside the welding arc zone.

As seen in Figure 3-4D, the injection of NO or CO into the primary shielding gas as a reducing agent was much less effective at reducing the Cr^{6+} emission than the IDST and ASE technology. In addition, the emission of unreacted NO or CO, as well as the generation of NO_2 potentially pose additional health hazards. Hence, the ASE technology is better suited for reducing Cr^{6+} in welding fumes.

XPS Results

Figure 3-5 shows the XPS spectra of selected samples. Significant bands were found at binding energies from 577.0~578.0 eV for Cr 2p3/2 and 587.0~588.0 eV for Cr 2p1/2. The Cr^{3+} peak was assigned by Cr^{3+} (577.2 eV) and Cr_2O_3 (576.3 eV), while the Cr^{6+} peak was assigned by CrO_3 (578.1 eV) and $Cr2O_7^{2-}$(579.2 eV). The ratio of the Cr^{6+} to Cr^{3+} was calculated by curve fitting. In this particular baseline sample (Figure 5a), the ratio of Cr^{6+} to Cr^{3+} was about 45:55. In the optimal TMS injected samples (Figure 5b), Cr^{6+} was absent. The XPS result provides semi-quantitative evidence of the absence of Cr^{6+} inside the silica shell. This supports the hypothesis that elimination of the Cr^{6+} occurred before the formation of the amorphous silica layer.

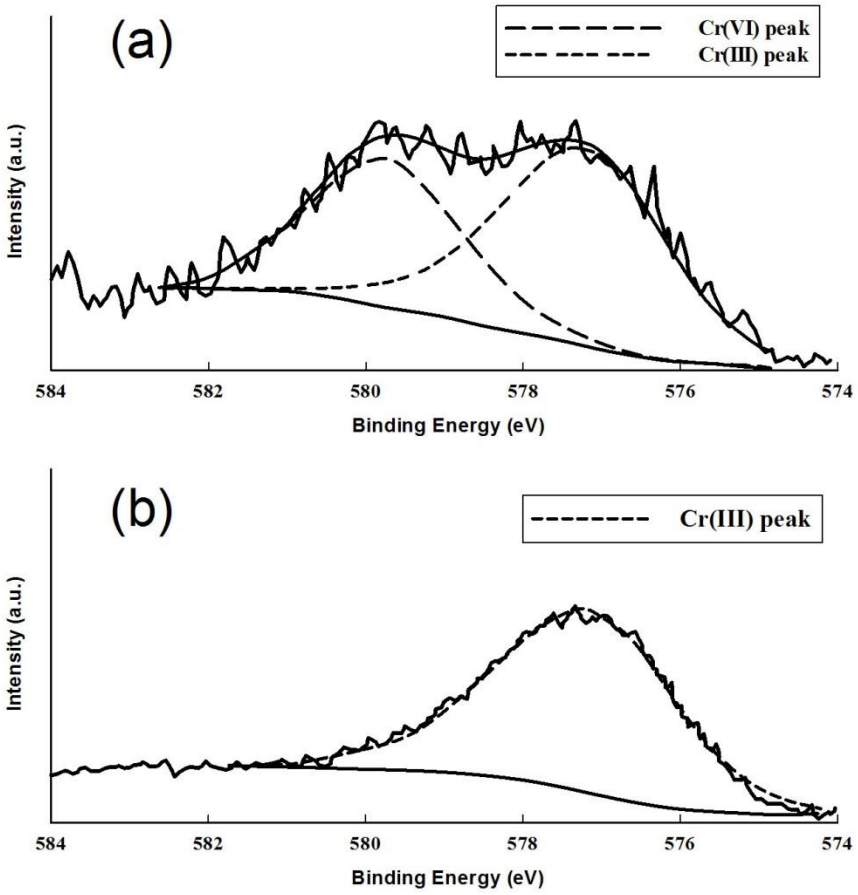

Figure 3-5. XPS spectra. A) baseline fume particle with peak assigned. B) XPS spectra of fume particle generated using 30 Lpm primary shielding gas and 4.2% TMS carrier gas

Field Sampling Results

Due to limited study resources, the only comparison made was between the airborne Cr^{6+} concentrations using no TMS gas versus using 1.6% TMS carrier gas/primary shielding gas. The Cr^{6+} concentration without using TMS was 9.8 (±3.4) $\mu g/m^3$, whereas the Cr^{6+} concentration was less than the limit of detection (1.1 $\mu g/m^3$) with 1.6% TMS carrier gas/primary shielding gas. The baseline airborne Cr^{6+} emission of 9.8 $\mu g/m^3$ was less than the baseline Cr^{6+} concentrations in the chamber samples (range: 25~56 $\mu g/m^3$) due to the greater dilution ventilation in the field setting.

The percentage of TMS carrier gas/primary shielding gas needed to achieve maximum reduction in the field (1.6%) was also lower than the laboratory (3.2%). The possible reason was that the pulse welding process employed in the field sampling could decrease the heat input and increase the efficiency. This also indicates different welding machines and processes might have different optimal injection rates for silica precursor.

Effects on Welding Quality

Figure 3-6 shows photographs of two welds made using baseline (no TMS gas) and 4.2% TMS carrier gas added to 30 Lpm primary shielding gas (75% Ar + 25%CO_2), respectively. The welds were examined by a certified professional welder who reported no visual difference on buildup of the weld. The reaction between the TMS and oxygen species introduced extra heat input to the weld, which led to a longer cooling time for the weld puddle. This is similar to the role of CO_2 in the shielding gas. CO_2 is commonly added to the shielding gas to help weld penetration in cases where the welding machine does not have sufficient capacity. If extra heat is not desired, one can always use other components of the shielding gas to compensate for the heat, such as increasing the Ar content or increasing the primary shielding gas flow rate. The TMS vapor also increased the globular size in the globular transfer mode. The globular tended to bounce at the edge of the weld and create more spots. This problem did not occur in the short-circuit and the spray modes.

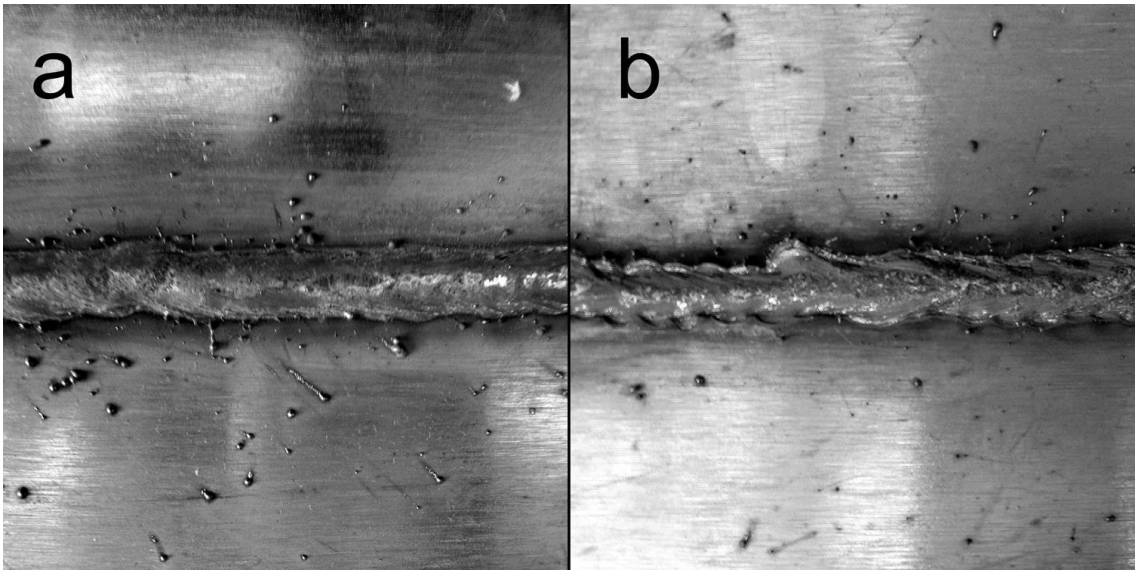

Figure 3-6. Photographs of weld surface. A) baseline. B) 30 Lpm primary shielding gas and 4.2% TMS carrier gas

Apart from these two effects, there was no other evidence that TMS altered the welding process, and no mechanical structure change was expected. However, further in-depth mechanical test such as transverse tensile and bend tests should be performed to confirm the effects of introducing TMS on the generated weld.

Hazard and Cost Estimation

Equation 3-3 was used to calculate the worst-case volume concentration of unreacted TMS vapor in the air in a 5m×5m×3m room with a 5-min duration of welding. The scenario represents the conditions of the field sampling in this study (details of the calculation are given in Appendix A). This equation is based on dilution of the saturated carrier gas (TMS vapor in Ar) entering the TMS-free room air without ventilation. An assumption was made that the saturated carrier gas was at atmospheric pressure (760 mmHg). The saturation vapor pressure of TMS is 271 mmHg at 0 ºC (ice bath). The corresponding maximum concentration was calculated to be 5.7 ppm when injecting

2.4×10^{-4} m^3/min TMS carrier gas which was the flow rate (0.24 Lpm) used in the field sampling. This maximum concentration was three orders of magnitude below the TMS' lower flammable limit/lower explosion limit (LFL/LEL) of 1%. This result indicates the use of TMS will not cause explosion risks for welding in a typically sized room, even without removal by ventilation.

$$C_{TMS} = \frac{271\,mmHg \times Qt}{760\,mmHg \times V} \times 10^6 \qquad 3\text{-}3$$

where C_{TMS} is the concentration of TMS (vppm), Q is the flow rate of TMS (2.4×10^{-4} m^3/min), t is the duration of welding (5 min), and V is the space of the room (75 m^3).

Using the model from SERDP PP-1415 (Lippold and Frankel 2009) to assess the additional costs of the TMS in various welding processes, the general material cost was calculated to increase by 3.8% (see Appendix A). The cost of the shielding gas containing TMS was $0.6 per ft of weld. This cost does not include the initial capital cost of the IDST, which might vary significantly from laboratory phase to industrial bulk production. The details of these calculation are available in another report (Paulson and Wu 2012). The costs of implementing the ASE technology are comparable to those of other control technologies such as LEV and on-gun extraction (WTIA 1999; Pocock et al. 2009).

Summary

Overall, the use of the IDST with the ASE technology was shown to reduce the airborne Cr^{6+} concentration to below the limit of detection (2.8 μg/m^3) in the laboratory, under all primary shielding gas flow rates. The premature decomposition of silica precursor that occurred in the premix mode was minimized by injecting the primary shielding gas and TMS carrier gas separately. TMS was shown to be more effective and

less hazardous than NO and CO as a reducing reagent in welding applications, with an acceptable cost. As observed in the previous studies, the in-situ generated silica condenses on the fume particles that can insulate the metals from the analytical eluent of IC. XPS result confirms that at the optimal ratio, TMS prevented the formation of all the Cr^{6+} compounds.

In addition to the laboratory chamber sampling, a fixed-location area sampling study was carried out in an industrial welding facility to examine the practicality of this technology. By adding 1.6% TMS carrier gas to the primary shielding gas, the Cr^{6+} concentration was reduced to below the limit of detection of 1.1 $\mu g/m^3$. Furthermore, visual inspection of welds generated using the ASE technology showed no surface deterioration in weld quality. Nevertheless, a mechanical structure test will be helpful in determining if extra heat and increased globular size introduced by the TMS have any impact on weld quality.

Besides reducing the Cr^{6+} concentration in welding fumes, ASE technology also encapsulates other toxic metals such as Ni and Mn, which will be discussed in the next chapter.

CHAPTER 4
ENCAPSULATION EFFECTIVENESS OF WELDING FUME PARTICLES AND ITS IMPACT ON MECHANICAL PROPERTIES OF WELDS

Objective

Coating an amorphous silica layer on particle surfaces to insulate engineered nanoparticles from degradation from exposure to the surrounding environment has been reported in various studies (Liz-Marzán et al. 1996; Biswas et al. 1997; Correa-Duarte et al. 1998; Yi et al. 2005; Teleki et al. 2009). It has also been demonstrated to be an effective measure for controlling nano-sized metal particle emissions from combustors and incinerators (Biswas et al. 1995; Owens and Biswas 1996; Biswas et al. 1997; Biswas and Wu 1998). This concept, when implemented in welding (as shown in Figure 4-1), has been labeled amorphous silica encapsulation (ASE) and presents a potential solution that can reduce the toxicity of welding fume particles provided the silica coating layer is in the amorphous phase. Indeed, X-ray diffractograms (XRD) of the coated fume particles confirmed that the in-situ generated silica was all in the amorphous phase (Topham et al. 2010), hence eliminating the potential hazard of crystalline silica. The amorphous silica layer on metal particles can insulate the metal species from absorption when inhaled. Additionally, silica thus formed yields a web-like network structure that effectively increases the size of the particles, which shifts the particle deposition upward in the respiratory tract (ICRP 1994). Furthermore, the decomposition of the silica precursor scavenges oxygen species, thus suppressing the oxidation of Cr to Cr^{6+} (Topham et al. 2010; Topham et al. 2011; Wang et al. 2012).

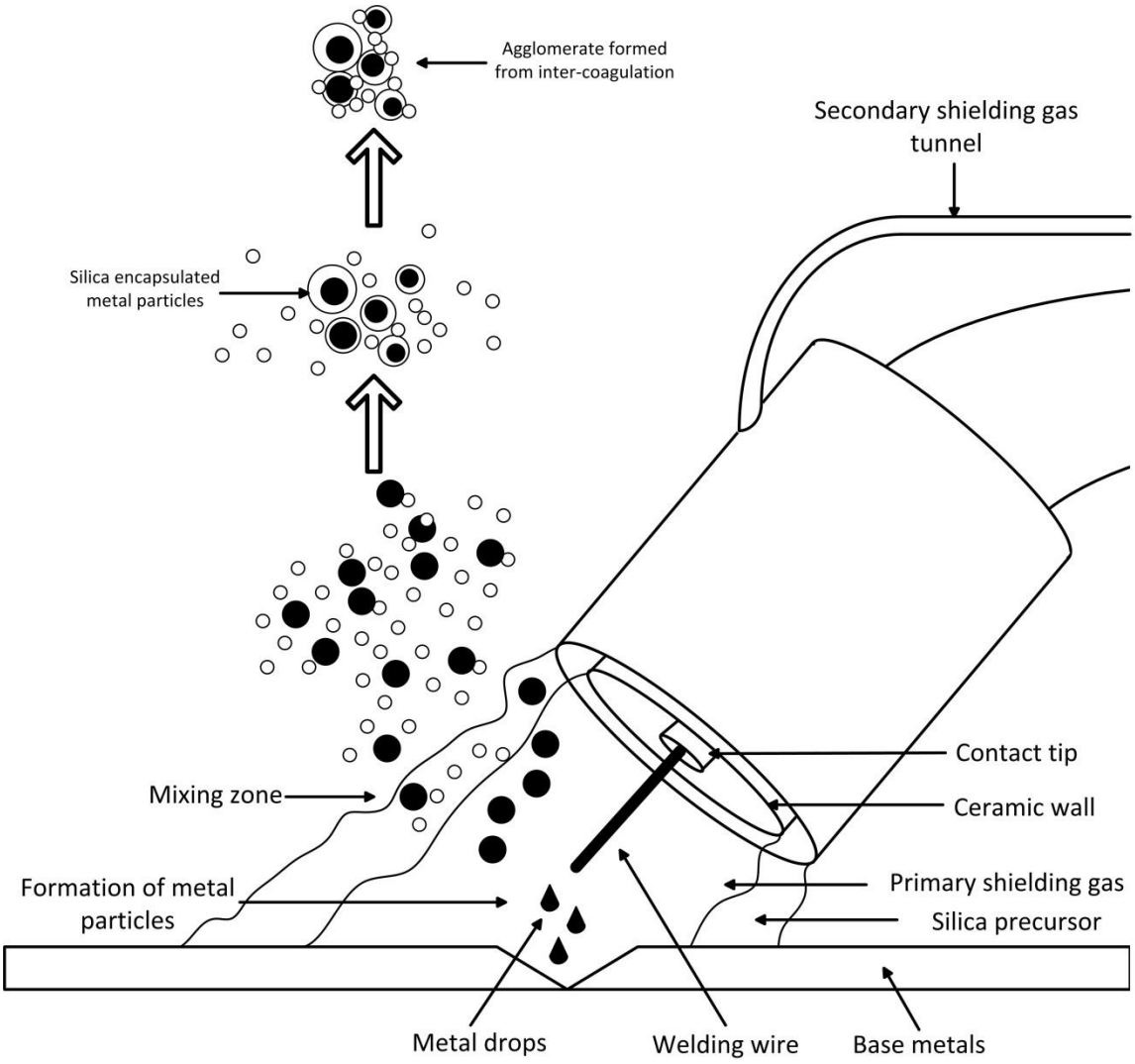

Figure 4-1. Mechanistic illustration of the ASE technology in welding application

The results in Chapter 2 using a premixed shielding gas containing a silica precursor showed the SCE to be about 14~38%, depending on the flow rate used. The relatively low SCE resulted from the premature decomposition of the silica precursor, i.e., the spatial and temporal mismatch of metal vapor's nucleation and silica condensation. At low shielding gas flow, when the gas could not effectively disperse the heat, thermal energy induced the decomposition of the silica precursor and the formation of silica particles inside the nozzle and outside the welding arc zone, before welding fume particles had even formed. In Chapter 3, an insulated double shroud torch

(IDST) was developed to address this premature decomposition issue (Wang et al. 2012). The IDST design involves a ceramic wall in the torch to insulate the heat between the primary shielding gas and the silica precursor carrier gas (as shown in Figure 4-1), thus preventing the premature decomposition of the silica precursor that occurs when the gases are premixed. While the testing showed reduction of airborne Cr^{6+} concentration to below the detection limit, the impact on SCE and the mechanical properties of the weld remained unknown. Knowledge of SCE is imperative due to the fact that uncoated fume particles are still available for worker inhalation and subsequent systemic biodistribution. Verification that the mechanical properties of the weld had not been altered by the addition of the silica precursor is critical, if the technology is to be accepted and adopted by the industry.

The objectives of this Chapter were to assess the effectiveness of the ASE technology with IDST feeding to encapsulate the welding fume particles and to characterize the mechanical properties of welds. Both quantitative analysis of SCEs and qualitative TEM images were acquired for evaluating the conditions of encapsulation. The weld generated from the ASE technology underwent a series of mechanical property tests to validate the applicability of the ASE technology to welding practices.

Experimental Methods

Welding Fume Generation

Sampling of welding fumes (Figure 4-2) followed the American Welding Society (AWS) fume hood design recommended in Method F1.2-2006 (AWS 2006). Welding fumes were generated in an enclosed conical chamber of 36 inches in diameter at the base, 8 inches in diameter at the top, and 36 inches in height. A high-volume flow pump (General Metal Works GL-2000H, Cleves, OH) was mounted on top of the chamber.

The welding fume particles generated were collected onto a glass fiber filter (Whatman 90 mm, pore size 1 µm, Maidstone, Kent, UK).

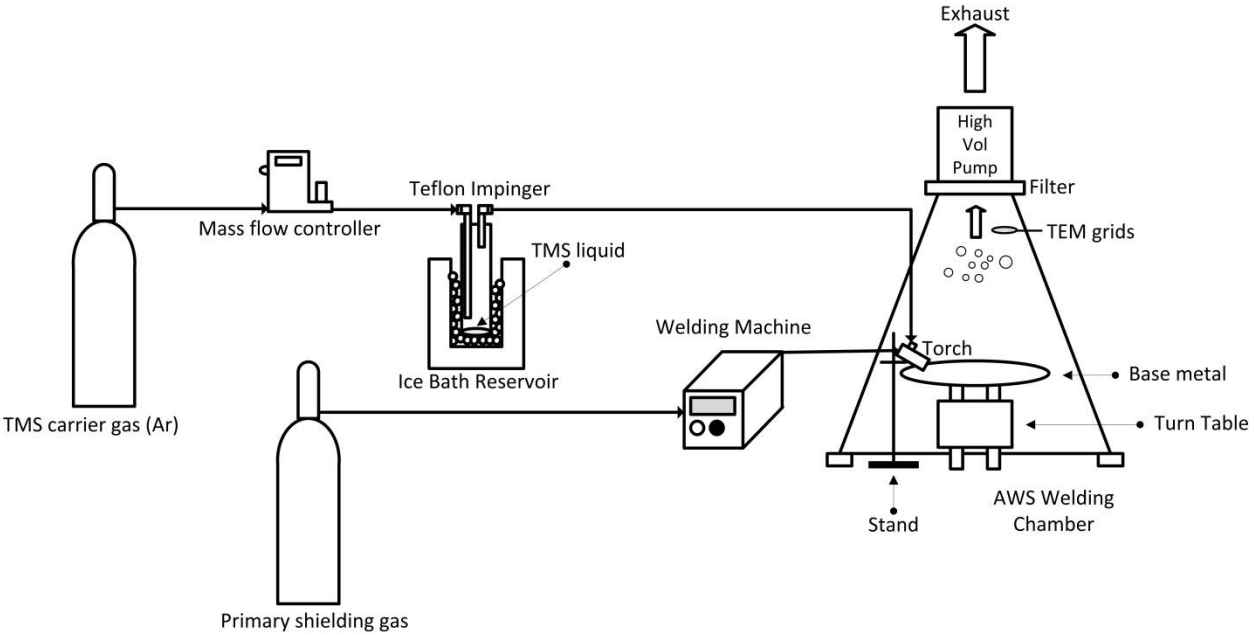

Figure 4-2. Schematic diagram of the TMS feeding apparatus and the welding fume chamber

A welding machine (Lincoln Power MIG 140C, Cleveland, OH) was used in the study. The voltage and wire speed were kept at 19.5 V and 100 inches per minute (ipm) throughout the study. The welding wires used were ER 308L stainless steel of 0.035 inch diameter, with a nominal composition of 19.5~22.0% Cr, 9.0~11.0% Ni, and 1.0~2.5% Mn. A mild steel base metal was used to minimize costs as well as to avoid interference from stainless steel components in the base metal. The base metal plates were placed on a rotating turntable (MK Products Aircrafter T-25, Irvine, CA) at the bottom of the chamber (as seen in Figure 4-2). A stand was used to hold the welding gun and to keep the torch at a constant height relative to the base metals. The trigger of the welding gun was modified to allow remote control from outside the welding

chamber. The chamber study simulated welding on the rotating plates for 1.5 minutes per sample. The length of the sampling period was based on those used in previous studies to ensure sufficient fume particles were collected for analysis.

An IDST replaced the conventional welding torch to allow separate flows of the primary shielding gas and the TMS carrier gas. The TMS carrier gas (argon) flowed through a Teflon impinger (Apex Instruments T507G, Fuquay-Varina, NC) filled with TMS liquid at the bottom. The impinger was immersed in an ice bath at 0 °C to lower the vapor pressure of TMS for controlling the amount of vapor entering the carrier gas. The TMS-saturated carrier gas was delivered to the welding arc zone through the outer shroud of the IDST. A mixture of 75% argon and 25% carbon dioxide was chosen as the primary shielding gas, based on the low power capacity of the welding machine. The flow rates of the primary shielding gas and the TMS carrier gas (listed in Table 4-1) were respectively controlled by a rotameter (Radnor HRF-1425-580, Radnor, PA) and a mass flow controller (Omega FMA5500, Stamford, CT).

The welding fume particles collected on the filter were gravimetrically measured before and after sampling, using an analytical scale (Sartorius MC210S) with a readability of 10 µg. Each sample was weighed three times and the mean value was calculated.

Table 4-1. Flow rates of primary shielding gas and TMS carrier gas, and the corresponding mass of collected welding fume particles

Primary shielding gas (Lpm)	TMS carrier gas (Lpm)	Mass of collected fume particles (mg)
20 (low)	0.16	12.3±1.1
	0.32	13.1±0.9
	0.64	11.7±1.3
	0.96	12.4±0.6
25 (medium)	0.16	13.6±0.9
	0.32	12.8±1.7
	0.64	14.2±0.8
	0.96	13.0±1.2
30 (high)	0.16	17.6±1.5
	0.32	16.5±0.8
	0.64	19.2±1.1
	0.96	21.4±2.3

Analysis of Silica Encapsulation

Determination of SCE followed the methodology developed in a Chapter 3, which used the acid resistance ability of the silica shell to measure SCE. Glass fiber filters loaded with welding fume particles were cut into two halves. One half was digested using 9 mL nitric acid (HNO_3, 68%) and 1 mL hydrofluoric acid (HF, 48~51%), which were aggressive enough to dissolve all the metals regardless of their coating conditions. The other half was digested using 10 mL aqua regia, a mixture of HNO_3 and hydrochloric acid (HCl, 38%) (1:3 v/v), which only dissolved metals not encapsulated in the silica shell. The SCE was thus calculated by using the differences in measured metal mass in the following equation:

$$\mathrm{SCE} = \frac{\sum_{i=1}^{N} C_{NF,i} - \sum_{i=1}^{N} C_{AR,i}}{\sum_{i=1}^{N} C_{NF,i}} \times 100\%, \qquad 4\text{-}2$$

where SCE is in percentage (%), N is the number of metals involved (three in this study), $C_{NF,i}$ is the measured concentration of the i^{th} metal digested by HNO_3/HF mixture, $C_{AR,i}$ is the measured concentration of the i^{th} metal digested by aqua regia. In other words, SCE represents the ratio of encapsulated metals to total metals measured.

The digestion was done using a microwave digestion system (CEM MDS 81D, Matthews, NC) following the eight-step protocol described in the previous study (Wang et al. 2011). The digests were cooled, filtered, and diluted. Measurement of the mass of each metal in diluted solutions was conducted with inductively coupled plasma-atomic emission spectroscopy (ICP-AES, Perkin-Elmer Plasma 3200, Norwalk, CT). Two atomic emission spectral lines for each metal (Cr, Ni, and Mn) were used simultaneously to reduce spectral interference introduced by other co-existing elements in the welding fume. The operating conditions and spectral lines selected are listed in Table 4-2. The concentration of each metal in a sample was determined by averaging the results of five reading replicates.

Transmission electron microscopy (TEM, JEOL 2010F, Peabody, MA) was used to observe the morphology and silica encapsulation conditions of the welding fume particles. The JEOL 2010F has an ultrahigh spatial resolution below 1 nm. A specialty grid (Pelco 300 mesh, Ted Pella, Redding, CA) was inserted into the welding chamber, as shown in Figure 4-2. The grid was held for 30 s in the welding fume stream drawn upwards by the pump. Fume particles thus attached to the ultrathin lacy carbon film on the grid. Images of both the baseline and the ASE samples were captured. The microscopic image is a supplemental tool for determining the effectiveness of the ASE technology. However, TEM only focused on a fraction of the welding fume particles and was limited to a two-dimensional plane.

Table 4-2. Operating conditions of the ICP-AES and the spectral wavelengths used for the analysis

Incident Power (W)	1300
Plasma gas flow rate (Lpm)	13
Auxiliary gas flow rate (Lpm)	0.5
Nebulizer gas flow rate (Lpm)	0.8
Peristaltic pump flow rate (mL min^{-1})	1
Reading delay time (s)	40
Reading per sample	5 replicates
Cr spectral wavelengths (nm)	205.552, 267.716
Ni spectral wavelengths (nm)	231.604, 221.647
Mn spectral wavelengths (nm)	257.610, 293.306

Mechanical Property Test

It is difficult to generate welds of high quality using the chamber system due to problems of the welder's access to the enclosed environment. The welds for mechanical property tests were generated at an industrial facility that regularly conducts welding activities. The modification to the conventional welding system in the facility for the IDST was similar to the laboratory chamber setup, except with a different welding machine (Miller Invision 456MP, Appleton, WA). The voltage was controlled by a pulse program with an average of 26 V. ER 310 stainless steel base plate of 0.18-inch-thickness was welded with 0.045-inch-diameter ER 310 stainless steel welding wire. The nominal ER 310 stainless steel plate composition is 24-26% Cr, 19-22% Ni, and 2% Mn, while the welding wire is 25-28% Cr, 20-22.5% Ni, and 1-2.5% Mn. The wire speed was fixed at 192 ipm. The primary shielding gas used was a mixture of 69% Ar, 30% He, and 1% CO_2. The flow rates of the primary shielding gas and the TMS carrier gas flow were kept constant at 15 Lpm and 0.24 Lpm, respectively.

A total of six welds were produced, three for the baseline and three for the ASE technology. Two of the six joints were analyzed for chemical composition (ASTM 2011b) prior to machining. Standard transverse tension test specimens were machined from

each weld (ASTM 2011a). Metallographic analysis was performed on additional weld sections at both macro- and microstructure scales for each weld. Examinations highlighted fusion, penetration, microstructure, macrostructure, and weld discontinuities. The transverse tensile tests (AWS 1998; ASTM 2011a), were designed to compare the performance of welds generated from the baseline and ASE technology.

Quality Control and Statistics

All chemicals used were analytical grade or higher in purity. DI water used for dilution and cleaning was deionized and purified by a Nanopure system (Barnstead Nanopure D11901, Thermo Fisher Scientific, Waltham, MA) to a conductivity of 18.2 mΩ-cm. All acid solutions (Acros Organics, Morris Plains, NJ) were at their original concentration and not diluted. All the shielding gases used were ultra-high purity and certified by the manufacturers (Airgas and Air Liquide). The glassware used in the study was cleaned in an ultrasonic cleaner (FS220, Thermo Fisher Scientific, Waltham, MA) for 4 hours, and dried in an Isotemp oven (FS230G, Thermo Fisher Scientific, Waltham, MA) in a laminar flow hood. The tubing in the sampling system was Polytetrafluoroethylene (PTFE) or Tygon, and air leaking tests were performed regularly.

The calibration curve for chemical analysis was obtained from external standards. Standard solutions were prepared by diluting high-purity stock solutions with DI water: 1000 mg/L Ni and 1000 mg/L Mn (Spex Certiprep, Metuchen, NJ) and 1000 mg/L chromate (CrO_4^{2-}) (Acros Organics, Morris Plains, NJ).

All the samples were pentaplicate per each combination of the primary shielding gas flow rate and the TMS carrier gas flow rate. *t*-test was used to examine the results

from different combinations using a significance level of $p = 0.05$. Statistical analyses were performed using the statistical software SAS 9.3.

Results and Discussion

Silica Encapsulation

Figures 4-3A~C show SCEs under different combinations of primary shielding gas and TMS carrier gas flow rates. Overall, the SCE ranged from 31~76%, which was a significant improvement from the SCE of 14~38% with premixed gases in the previous study (Wang et al. 2011). Furthermore, the TMS carrier gas feed rate was below 1 Lpm (compared to over 2 Lpm when the gases were premixed.) Inspection of the welding gun revealed few deposits of white silica powder, verifying a lower degree of premature decomposition of the TMS. These pieces of evidence prove that the IDST design can deliver silica precursor to the welding arc zone more effectively and efficiently than the premixed gas method while decreasing the costs associated with feeding excessive TMS.

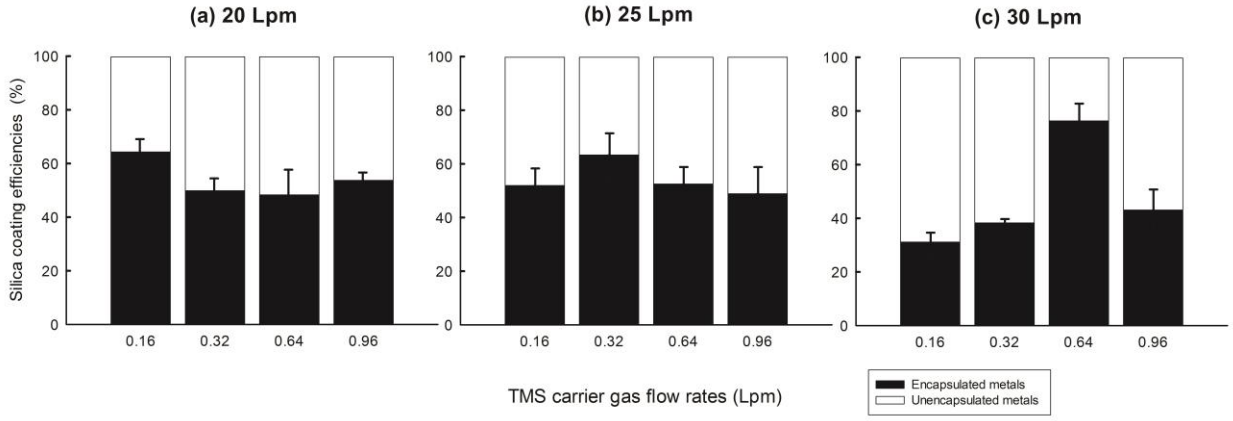

Figure 4-3. SCE as a function of TMS carrier gas flow rate. A) 20 Lpm. B) 25 Lpm. C) 30 Lpm primary shielding gas flows.

Under the low and medium shielding gas flow rates, the highest SCE were similar at 64%. The highest SCE for 20 Lpm (low) primary shielding gas flow was 64±6.1%, feeding with only 0.16 Lpm TMS carrier gas, and there was no statistical difference in SCE among 0.32~0.96 Lpm TMS carrier gas flow rates (p>0.1). The SCE of the 25 Lpm (medium) primary shielding gas flow reached a maximum of 64±9.4% at 0.32 Lpm TMS carrier gas flow rates, and no statistical difference for the rest of TMS carrier gas flow rates. The 30 Lpm (high) shielding gas flow showed a different trend. The SCEs were low at 31±4.9% and 38.3±2.8% at 0.16 Lpm and 0.32 Lpm TMS carrier gas flow rates, respectively. Although a maximum SCE of 76±7.9% occurred at 0.64 Lpm TMS carrier gas flow, it decreased to 43±9.0% after further increase of the TMS carrier gas flow rate.

Table 4-1 lists the mass of collected fume particles under the different conditions tested. The gravimetric measurements of collected fume particles under low and medium primary shielding gas flows were significantly lower than those of high shielding gas flow (p<0.01). Hence, the ASE technology was able to deliver enough in-situ-generated silica to coat the relatively low amount of welding fume particles under low and medium primary shielding gas. However, coating under high primary shielding gas flow (30 Lpm) was less effective with low TMS feed rates, at least partially due to the high mass of welding fume generated. At very high TMS feed (0.96 Lpm), both the primary and the TMS carrier flows might disperse the silica vapor and metal particles to a larger mixing zone and therefore reduce the time of interaction. The chaotic condition at high gas flow was confirmed by the TEM images later, with a large quantity of uncoated metal particles and the formation of stand-alone silica particles.

By delivering TMS into the effective mixing area using the IDST technology, it was hoped that the SCE would be near 100% and all metal particles would be fully encapsulated. However, the welding process naturally contains a high intensity of ultraviolet (UV) light emitted from the welding arc. TMS inevitably undergo photolysis under UV (González et al. 1992) in undesirable locations such as inside the welding gun. This was confirmed by the trace amount of silica powder deposits in the torch. To further improve SCE, aerosol dynamic modeling of the welding fume system will be needed to provide helpful insights into the effects of the UV and other influential factors. These insights can be used to optimize the silica precursor delivery setup.

The calculation of SCE was done by summing up the differences in mass of individual metals. The mass of iron (Fe) was excluded from the calculation due to its insignificant toxicity, even though Fe is a major component among the metals in welding fume particles. Other trace metals present only in extremely low amounts in the welding fume particles were also disregarded. Hence, SCE as calculated was toxicity-weighted with Cr, Ni, and Mn. In addition, SCE measurements only counted particles fully enclosed in a hermetical silica shell (i.e., partially encapsulated particles were not counted as encapsulated). In short, SCE measurements conservatively quantify the reduction in the bioavailable mass of selected toxic metals (Cr, Ni, and Mn) caused by encapsulation of these toxic particles in amorphous silica shells.

TEM Imagery

Figures 4-4A~D display the TEM imagery of welding fume particles under various conditions. Because of the penetration ability of electrons when interacting with the particles, metals with a high electron density are typically darker on a bright-field TEM image while silica is lighter with its low electron density (Williams and Carter 2009).

Figure 4-4A depicts the welding fume particles generated from 30 Lpm primary shielding gas without the introduction of TMS. The diameter of the welding fume particles ranged from 10~100 nm. From the 2D image, it was difficult to determine if the particles were chain-like agglomerates or overlapped at different planes.

Figures 4-4B~C show welding fume particles generated from 30 Lpm primary shielding gas and 0.64 Lpm TMS carrier gas flow with SCE of 76±7.9%. The images showed a silica-encapsulated metal agglomerate, with a clear boundary between the amorphous silica layer and its metal components. By comparing with Figure 4-4A, it was observed that the primary particle size was smaller than that in the baseline case. The result suggests that the silica coating prevented sintering of metal particles. Figure 4-4C also showed that encapsulated metal particles have different shapes, from spherical to polygonal. The nano-sized primary metal particles were bound to an agglomerate particle with a larger equivalent diameter through the inter-coagulation mechanism (Lee and Wu 2005). This resultant increase in particle size can effectively reduce respiratory tract deposition, due to the low deposition of particles around 200~300 nm (ICRP 1994).

Figure 4-4D shows the welding fume particles generated from 30 Lpm primary shielding gas and 0.96 Lpm TMS carrier gas flows with SCE of 43±9.0%. The particles are more randomly arranged, due to the high amount of welding fume particles generated and possible poor mixing interaction between silica vapor and metal particles. In the situation of excessive TMS feed, the silica vapor was more likely to form stand-alone silica particles than to condense on the surface of metal particles. The same phenomenon was also observed at the 0.96 Lpm TMS carrier gas flow with 20 and 25 Lpm primary shielding gas. Although some metal particles were trapped in the

silica matrix, a high level of excess silica particles formed from feeding a high amount of TMS warrants investigation of the health effects. Some studies showed that amorphous silica particles may cause phagocytosis but the mechanism by which this is caused is not clear (Lundborg et al. 2006; Yu et al. 2009; Costantini et al. 2011). TEM imagery supports the idea that there is an optimal TMS carrier gas flow rate for applying the ASE technology, i.e., a rate to allow sufficient silica vapor for the amount of metal particles, without causing an overflow of excess silica particles.

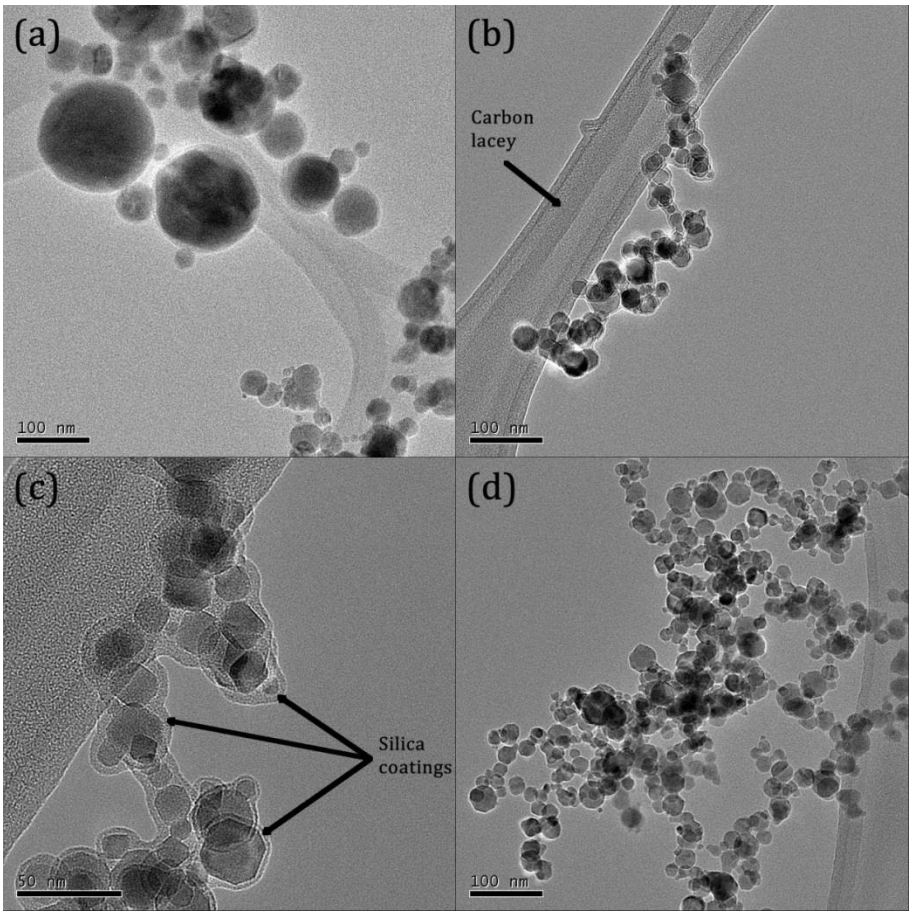

Figure 4-4. TEM images. A) baseline welding fume particles without any coating. B) welding fume particles agglomerate with a distinct silica layer. C) 2× magnification view of the fume particles and silica layer in image B. D) welding fume particles with excessive silica particles formed.

Mechanical Properties

The chemical compositions of the welds in weight percentage (wt%) from the baseline and the ASE technology are listed in Table 4-3. Cr, Ni, Mn, and other elements in both conditions were almost identical to the standard ER 310 stainless steel (AWS 2012). It was also noted that the ASE technology did not introduce extra Si content into the welds, while extra Si could adversely affect weld quality (Lampman 1997).

Table 4-3. Chemical composition (wt%) of weld metals and standard requirements

Standard material/Welds	Cr	Ni	Mn	Si	Mo	Cu	P	S
ER 310 stainless steel welding wire specification (AWS 2012)	25.0~28.0	20.0~22.5	1.0-2.5	0.30-0.65	N/A*	N/A*	0.05	0.03
Baseline	26.5	20.0	1.19	0.47	0.14	0.10	0.02	0.01
ASE technology	26.0	19.7	1.21	0.47	0.14	0.10	0.02	0.01

* No standard values for the elements Mo and Cu in the specification (AWS 2012)

The macrostructures of the welds are shown in Figure 4-5. The weld metal and base plate are labeled as WM and BP, respectively. The welds of the baseline technology revealed typical columnar grains adjacent to fine grains of the base plates. The welds from the ASE technology were identical to the baselines in macrostructure with no weld defect.

Figure 4-6A displays the microstructure of one particular baseline weld. The baseline weld was comprised of grains within the hundreds of micron range, adjacent to the fine grains in the heat-affected zone (HAZ) and the fusion line (FL). The microstructures of the baseline weld showed the presence of intermetallic particles onto which the grains nucleated. The microstructures of one particular weld generated by the ASE technology are shown in Figure 4-6B. The weld was generally similar to that of the

baseline, except for a tiny crack at the interface of the HAZ and weld metal (WM). It is possible that the addition of gas (TMS/Ar) created a gas pocket that coalesced into a crack. However, no crack was found in other welds from the ASE technology.

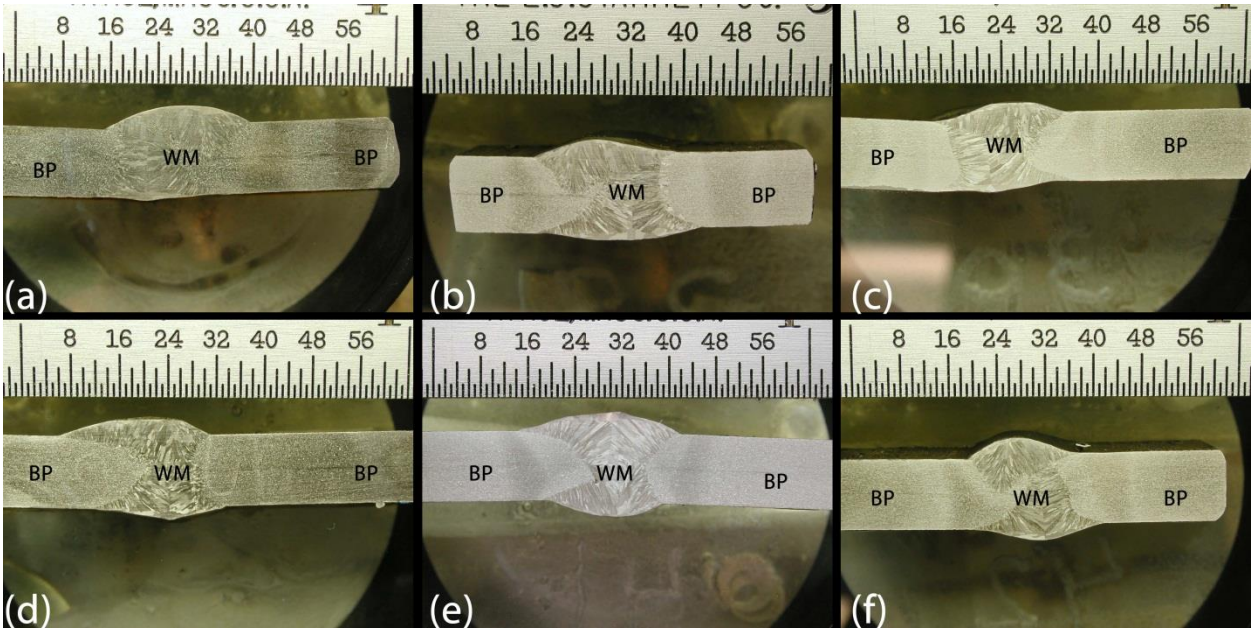

Figure 4-5. Macrostructure of welds. A) B) C) welds generated with baseline technology. D) E) F) welds generated with ASE technology.

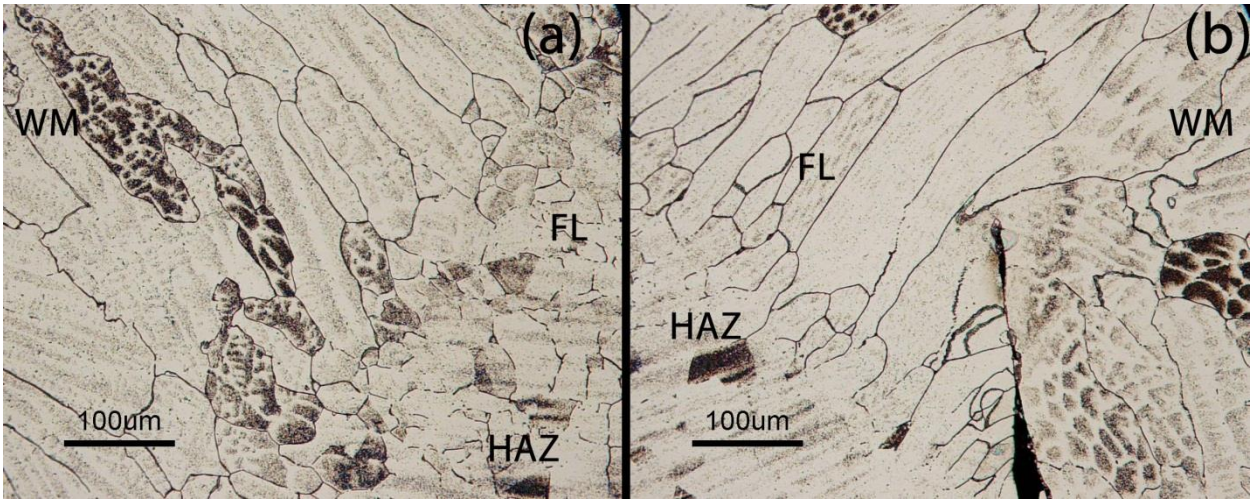

Figure 4-6. Microstructure of welds. A) baseline technology. B) ASE technology

The results of the tensile tests of the welds are shown in Figure 4-7A, and the detailed data are in Appendix B. The yield strength (YS) of the welds from the baseline and the ASE technology were identical, 44±1 kilo-pounds per square inch (ksi). Meanwhile, the ultimate tensile strength (UTS) of the welds from the baseline and the ASE technology were 83±4.3 ksi and 77±8.1 ksi, respectively, with no statistical difference (p>0.1).

Figure 4-7B shows the comparison of average elongation of welds from the baseline and the ASE technology. Again, the elongation values showed no statistical difference (p>0.1). The AWS requirement for ER 310 stainless steel (AWS 2012) is also displayed.

It should be noted that the AWS minimums for UTS and elongation are established for standard materials with uniform composition, not for welds involving a combination of welded metal, HAZ, and base metal. Hence, these AWS minimums are included for reference only. As both the baseline and the ASE samples were lower than the AWS minimum, welder inexperience working with a new welding shielding gas additive likely is a major factor contributing to the imperfect welds. If not from the statistical aspect, the result indicated that the ASE technology reduced tensile strength in some samples. While the ASE technology did not statistically deteriorate the mechanical quality of the welds, optimization of different welding parameters to achieve better tensile property certainly should be considered.

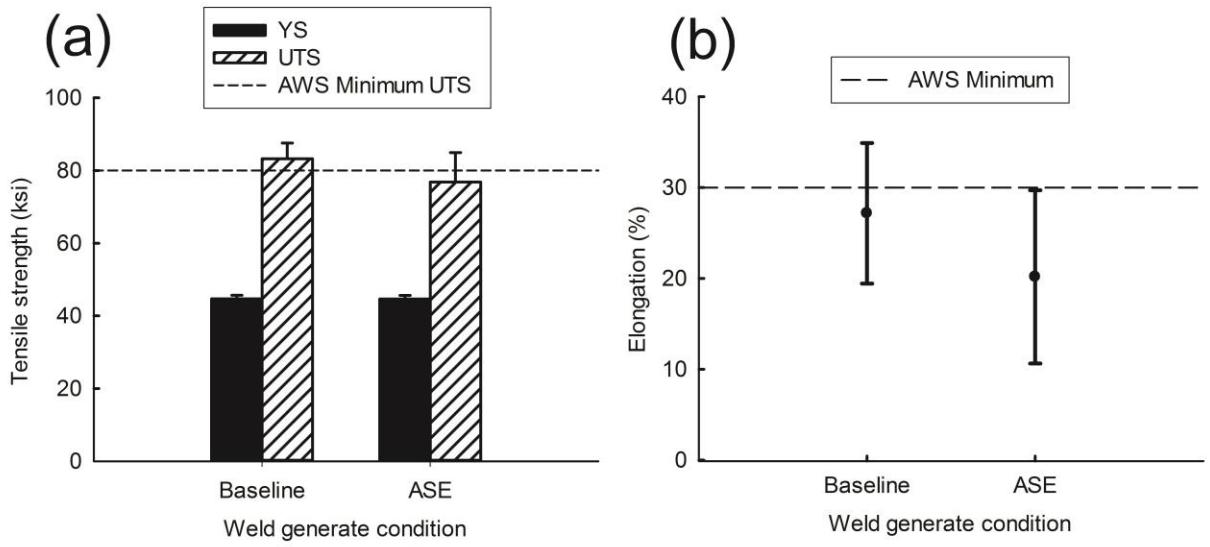

Figure 4-7. Tensile test results. A) Yield strength (YS) and ultimate tensile strength (UTS). B) elongation of welds generated with baseline and ASE technology

Summary

The ASE technology applied to the stainless steel welding process is an emerging method for effective minimization of welder exposure to toxic nano-sized welding fume particles. Overall, 31-76% of Cr, Ni, and Mn in the welding fume particles were completely encapsulated in a layer of amorphous silica by feeding the TMS carrier gas into the welding arc zone through the IDST. At low and medium primary shielding gas flow rates, the SCE was similar and reached a maximum of 64% at a moderate TMS carrier gas flow rate. At the high primary shielding gas flow rate, the SCE was 76% at 0.64 Lpm TMS carrier gas flow rate, and much lower at other TMS carrier gas flow rates. The high amount of welding fume generated at high primary shielding gas flow rate likely contributed to the low SCE. The high gas flows possibly caused a poor mixing, reduced the exposure time, and resulted in a low SCE and the formation of more stand-alone silica particles, which was confirmed by the TEM images. On the

other hand, the TEM images also showed a distinct silica layer on the primary metal particles and agglomerates at the optimal gas flow rate.

The result also showed that introducing TMS as an additive to the shielding gas did not change the metal and Si contents in the welds. The metallography of welds generated from the baseline and the ASE technology were similar. A tiny crack was found in the microstructure of one particular weld from the ASE technology. The yield strength, ultimate tensile strength, and elongation of welds from the baseline and the ASE technology showed no statistical difference.

The ASE technology may be further optimized to achieve both a higher SCE and mechanical properties through tools such as computational fluid dynamic simulations combined with aerosol dynamics. Toxicological studies are also essential to help fully realize the potential health benefits brought by the ASE technology.

CHAPTER 5
CONCLUSIONS AND RECOMMENDATIONS

In this doctoral study, an analytical method to determine the amount of metals encapsulated in the amorphous silica shell was developed. HNO_3/HF acid mixture and aqua regia digestion method were used to determine silica coating efficiencies based on the measured mass difference. This method can be also applied to applications of silica shell/metal core particles. Metals encapsulated by amorphous silica cannot be further extracted by general acid such as HNO_3 or aqua regia, or weak acid environment inside human body. Hence, this proportion of metal should not be bio-accessible to human body. The experimental result for the pre-mixed TMS feed showed silica coating efficiency increased with increasing shielding gas flow rate. The low silica coating efficiency under low shielding gas flow rate was due to the premature decomposition of silica precursors.

Insulated double shroud torch (IDST) was designed and shown to reduce the airborne Cr^{6+} concentration to below the limit of detection (2.8 $\mu g/m^3$) in the laboratory, under all primary shielding gas flow rates. The premature decomposition was minimized by injecting the primary shielding gas and TMS carrier gas separately. TMS was shown to be more effective and less hazardous than NO and CO as a reducing reagent in welding applications, with an acceptable cost. XPS result confirmed that at the optimal ratio, TMS prevented the formation of all the Cr^{6+} compounds regardless encapsulation status.

In addition to the laboratory chamber sampling, field study was carried out to examine the practicality of this technology. By adding 1.6% TMS carrier gas to the

primary shielding gas, the Cr^{6+} concentration was reduced to below the limit of detection of 1.1 µg/m^3.

Besides reducing the Cr^{6+} concentration in welding fumes, the ASE technology also encapsulates other toxic metals such as Ni and Mn. Using IDST, 31-76% of Cr, Ni, and Mn in the welding fume particles were completely encapsulated in a layer of amorphous silica. At low and medium primary shielding gas flow rates, the SCE was similar and reached a maximum of 64% at a moderate TMS carrier gas flow rate. At the high primary shielding gas flow rate, the SCE was 76% at 0.64 Lpm TMS carrier gas flow rate, and lower at other TMS carrier gas flow rates. The high amount of welding fume generated at high primary shielding gas flow rate likely contributed to the low SCE. The high gas flows possibly caused a poor mixing, reduced the mixing time, and resulted in a low SCE and the formation of more stand-alone silica particles, which was confirmed by the TEM images.

The ASE technology did not change the metal and Si contents in the welds. The metallography of welds generated from the baseline and the ASE technology were similar. The yield strength, ultimate tensile strength, and elongation of welds from the baseline and the ASE technology showed no statistical difference.

All the study results showed the potential of the ASE technology in addressing the welding fume exposure issues, by retrofitting the welding equipment with the IDST, without adversely impacting the cost and quality of welding process. The ASE technology answered the call from the National Occupational Research Agenda, which listed developing effective welding fume control technology as priority research area. The ASE technology upon implementation can possibly help the welding industries

comply the newest tightened occupational standard for Cr^{6+} and other metals. The technology may potentially protect over 500,000 welders in the US and more around the world, as welding activities continue to play an important role in the growing construction activities and economic revival. The newly developed method to quantify SCEs can be used in assessing other silica-metal core-shell structure nanotechnology applications. The study on SCEs under different flow rates of gases allows a better understanding of how silica and metals dynamically interact in such an aerosol system, and this knowledge can be extended to help understand other applications utilizing similar *in-situ* generated silica such as nanoparticle flame synthesis, thermal plasma reaction, and chemical vapor deposition.

There are several aspects that the ASE technology may be further optimized and assessed in the future: (1) to achieve both a higher SCE and mechanical properties through tools such as computational fluid dynamic simulations combined with aerosol dynamics modeling. The welding experiments are expensive with complicated factorial designs. Thus, modeling can be a good supplement and validation; (2) to investigate the cytotoxicity change caused by the amorphous silica shell. The human lung alveolar cells such as A549 cell can be cultured and exposed to the welding fume particles, to represent the inhalation toxicity. The cell exposure unit can be retrofitted to connect to a welding chamber directly to achieve an in-flight exposure of freshly generated welding fume particles; (3) to determine the bioavailability of welding fume particles before and after silica encapsulation using simulated lung fluid test. The biotoxicity can be greatly reduced if the adsorption of metals to human body is masked by an amorphous silica shell; (4) to develop a comprehensive systemic biokinetic model for welding fume,

coupling with respiratory deposition model, bioavailability and cytotoxicity test results. This model can be used to predict the health effects and to trace back the welding exposure. The tool will also be useful in assessing the effectiveness of the ASE technology.

APPENDIX A
DETAIL RESULTS OF THE HAZARD AND COST ESTIMATION

Estimation of TMS in the worst case scenario

One potential concern in implementation is the safe handling of TMS. Tetramethylsilane (TMS) is a flammable and volatile liquid. High concentration of TMS vapor may cause flash fires or explosions in oxidizing environments. Exposure to TMS may cause skin, eye, and respiratory tract irritation, although the toxicological properties of TMS have not been fully investigated. The MSDS suggests that workers should avoid inhalation of TMS. There is no standard or published document for handling welding with TMS shielding gas since it is still under development. Nevertheless, there has been no incident of fire or explosion involved in welding with TMS shielding gas to date.

We carried out a calculation of TMS concentration in a typical room in a scenario in which all TMS leaked into a room without decomposition. Vapor pressure (V_p) of TMS was calculated using the Antoine equation,

$$\log_{10} V_p = A - \frac{B}{T + C}$$

where A, B, C were 3.97703, 1047.242, -36.057 (Aston et al. 1941), respectively. Temperature was set to 273 K because the TMS was in an ice bath. Accordingly, V_p was 271 mmHg. The ideal gas law was used to calculate the concentration of TMS in saturated carrier gas,

$$\frac{n}{V} = \frac{P}{RT}$$

where pressure (P) is equal to 271/760=0.356 atm; gas constant (R) is equal to 82.0575 atm·cm^3/(K·mol); temperature (T) is equal to 273 K. Accordingly,

$$\frac{\mathrm{n}}{\mathrm{V}} = \frac{0.356\ \mathrm{atm}}{82.0575\,\frac{\mathrm{atm\ cm^3}}{\mathrm{K\ mol}} \times 273\mathrm{K}} = 1.59 \times 10^{-5}\,\frac{\mathrm{mol}}{\mathrm{cm^3}}$$

Consider the worst case scenario, in which all the TMS has leaked into the air without forming silica: Welding to join two test plates takes a maximum of about 3 min. According to the standard operation procedure (Appendix B) in field demonstration, the TMS flow would be stopped between two welding events while the welder replaced the plates and supplies. For a room of 74 m^3 and a pre-set carrier gas flow rate of 0.24 Lpm, the TMS concentration in the tent/room would be

$$\frac{1.59 \times 10^{-5}\,\frac{\mathrm{mol}}{\mathrm{cm^3}} \times (0.24 \times 1000)\,\frac{\mathrm{cm^3}}{\mathrm{min}} \times 5\ \mathrm{min}}{75\ \mathrm{m^3} \times 1\ \mathrm{atm} \div (8.20575 \times 10^{-5}\,\frac{\mathrm{m^3 atm}}{\mathrm{K\ mol}} \times 298\ \mathrm{K})} = 5.7\ \mathrm{ppm}$$

The value is orders of magnitude lower than the TMS lower flammable limit/lower explosion limit (LFL/LEL) of 1%. It should be noted this calculation is based on the worst case scenario, which is very unlikely to occur. The ventilation system in the field will lower the accumulated TMS concentration.

Result of the Cost Estimation

This cost estimation intended to compare three baseline welding processes utilizing the TMS technology. The estimation incorporated (1) the approximate cost differences between MIG welding using standard shielding gas and the TMS additive; (2) the approximate cost differences between standard ventilation systems and ventilation systems designed to meet the new occupational standards; (3) the approximate costs associated with the welding process requalification if a change is

made to the ASE technology. (4) assuming using the ASE technology without retrofitting conventional ventilation systems, will fit the occupational standards.

A detailed cost analysis for the substitution of Cr-free welding consumables for standard Type 308 filler metals for the welding of stainless steel was developed in 2006 under SERDP Project PP-1415, “Development of Chromium-Free Welding Consumables for Stainless Steels.” Some aspects of this approach were utilized to assess and compare the costs associated with the ASE technology and traditional welding. Ten different combinations of joint type and industry sector were evaluated. These same combinations were evaluated below to assess the effect on costs as a result of using the ASE technology. The industry sectors from which the applications were selected included shipbuilding, transportation and storage tanks, and general fabrication. The joint designs included V-groove butt welds between both pipe and plate configurations, as well as T joints with fillet welds.

The criteria developed in the PP-1415 were utilized for the various GMAW joints with the additional costs associated with the three TMS approaches included. The unit costs of each scenario are listed in Table A-1. These costs were then compared to costs of producing the same joints traditional welding. Scenario 1 represented the mixing of TMS at the torch. Scenario 2 utilized customized TMS cylinder gas, where the gas was supplied from the customized gas department of Airgas, a gas supply company. Scenario 3 was similar to Scenario 2, but with the estimated reduced cost of TMS cylinder gas once it is commercially available and in high-volume production (“commercial TMS cylinder gas”). The calculation of the commercial cost was based on a net profit rate of 50%, according to Airgas. Gas-flow costs were based on the

estimated total arc times associated with each joint type, and did not include mass flow controller and nozzle equipment costs.

Table A-1. Unit cost used in the cost model

	Unit price	Consumption rate	Cost per minute
Scenario 1			
Primary shielding gas (Ar/CO_2)	\$27/300 ft^3	29 Lpm	0.092226148
Carrier gas (Ar)	\$25/300 ft^3	1 Lpm	0.002944641
TMS	\$65.16/100 mL	0.02 mL/min	0.013032
Scenario 2			
Primary shielding gas (Ar/CO_2)	\$27/300 ft^3	29 Lpm	0.092226148
TMS premix cylinder gas	\$1264/44 L	1 Lpm	28.72727273
Scenario 3 (Commercial product of cylinder gas)			
Primary shielding gas (Ar/CO_2)	\$27/300 ft^3	29 Lpm	0.092226148
TMS premix cylinder gas	\$205/300 ft^3	1 Lpm	0.024146054

The comparisons of costs are summarized in Tables A-2. The results found that using TMS mixing at the torch would slightly increase costs, while using customized TMS cylinder gas would dramatically increase costs. The estimated commercial TMS cylinder gas can reduce the costs to the same level as TMS mixing at the torch. TMS in the cylinder would be more convenient to end users than the other means. While customized TMS cylinder gas is already available, currently it is only available through custom order. The result suggested that costs would be greatly reduced once the ASE technology becomes widely adopted in the welding community, and TMS gas in cylinders becomes a commonly available commodity.

When OSHA established the new ventilation requirements for reducing exposure to hexavalent chromium, it stated that the primary methods for reducing such an exposure would be local exhaust ventilation and improvement of general dilution ventilation. In addition, it was anticipated that in many cases, a welder would utilize personal protective equipment with a respirator when welding stainless steels.

Therefore, this cost assessment was based on the assumption that a typical fabrication facility would incur additional costs for improved general and local ventilation, as well as personal protective equipment, as a result of the new OSHA regulation.

Table A-2. Welded joint costs of traditional welding and ASE technology

			Traditional		ASE	
Scenario 1 (mixed at torch)						
Industry	Joint description	Process	Cost/ft or cost/joint* ($)	gas cost ($)**	Cost/ft or cost/joint* ($)	gas cost ($)**
Ship building/pressure vessels	6" diameter pipe	GMAW	24.5	1.2	25.2	1.9
	12" diameter pipe	GMAW	56.2	2.3	57.8	3.9
	3/16" fillet weld	GMAW	7.4	0.5	7.7	0.8
Tanks	3/16" butt weld	GMAW	5.4	0.5	5.7	0.8
	3/8" butt weld	GMAW	8.8	0.5	9.1	0.8
General fabrication	3/16" fillet weld	GMAW	2.2	0.3	2.4	0.5
	1/4" fillet weld	GMAW	4	0.4	4.3	0.7
Scenario 2 (customized TMS shielding gas in cylinder)						
Ship building/pressure vessels	6" diameter pipe	GMAW	24.5	1.2	542	509
	12" diameter pipe	GMAW	56.2	2.3	1092	1038
	3/16" fillet weld	GMAW	7.4	0.5	214	207
Tanks	3/16" butt weld	GMAW	5.4	0.5	223	218
	3/8" butt weld	GMAW	8.8	0.5	226	218
General fabrication	3/16" fillet weld	GMAW	2.2	0.3	122	120
	1/4" fillet weld	GMAW	4	0.4	185	181
Scenario 3 ((commercial TMS shielding gas in cylinder)						
Ship building/pressure vessels	6" diameter pipe	GMAW	24.5	1.2	25.4	2.1
	12" diameter pipe	GMAW	56.2	2.3	58.1	4.2
	3/16" fillet weld	GMAW	7.4	0.5	7.7	0.8
Tanks	3/16" butt weld	GMAW	5.4	0.5	5.8	0.9
	3/8" butt weld	GMAW	8.8	0.5	9.2	0.9
General fabrication	3/16" fillet weld	GMAW	2.2	0.3	2.4	0.5
	1/4" fillet weld	GMAW	4	0.4	4.3	0.7

There are numerous general considerations associated with ventilation decisions regarding the new OSHA ventilation requirements, including issues such as the size of the fabrication facility and whether or not welding is being conducted in confined space. Every case will be different. This analysis was based on two typical cases: a relatively

large fabrication space and a relatively small fabrication space. It is important to point out that this comparison represents very generic cases, and should only be used as a guideline. In addition to the overall size of the facility, there are many specific factors that must be considered that will affect ventilation requirements for each location. Examples of other factors to be considered included the location and number of roof and wall ventilators, overhead doors and obstructions, make-up air exchange systems, welding parameters, working hours, annual consumable usage, type of welding processes used, etc.

For the purposes of this generic comparison, the two different weld shop sizes considered were a 60 by 30-ft shop with 12 welders, and a 200 by 100-ft shop with 36 welders. Assumptions in each case included a single shift, welding parameters ranging from 90 to 150 amps, overhead obstructions (cranes) and no wall ventilators, and an heating ventilation air conditioning (HVAC) system present as an air exchange system. In the case of the larger shop, it was assumed there were five roof ventilators at 1000 CFM each, 4 overhead doors, and the annual consumable usage was estimated at 60,000 lb/year. For the smaller shop, it was assumed there were 2 roof ventilators at 1000 CFM each, 2 overhead doors, and the annual consumable usage was estimated at 20,000 lb/year. In each case, it was assumed that SMAW, GMAW, and GTAW processes were used. The extent to which the SMAW process is used will play a significant role in filter replacement frequency (higher usages of SMAW will require more frequent filter replacements), but there was no attempt to quantify this detail. One more major assumption was that 100% of the welding in these two shops was stainless steel, which in many cases would not be accurate.

Lincoln Electric provided quotes for ventilation systems that were used for comparison. The system costs included both a general ventilation system and a source extraction system. The general system was a U-shaped push-pull type. This would provide a continuous positive and negative air flow over the weld area. The source ventilation system included pivoting and telescopic extraction arms for each welding booth. Other costs considered included the costs of personal protection ventilation suits and air monitoring. The summary below incorporates the aforementioned assumptions and information and compares the typical ventilation system purchase cost differences between a shop that welds stainless steel (and therefore is subject to the new OSHA requirements) to those of a shop not subject to such requirements. These results are also summarized on Table A-3.

Table A-3. Typical ventilation system cost

Weld shop size	Number of welders	meet OSHA standard	Initial purchase expense ($)	Recurring expenses ($)
200’ × 100’	36	Yes	700000	50000
		No	410000	20000
60’ × 30’	12	Yes	162000	20000
		No	100000	10000

For the purposes of better understanding the financial impact of the OSHA hexavalent chromium lower exposure requirement, and the additional costs associated with the ASE technology, six scenarios involving the two welding shop sizes were compared. The results are summarized in Table A-4.

Table A-4. Summary of the cost comparison of the ASE technology in different scenarios and traditional welding

Room size	Scenario	Initial cost ($)	Annual recurring cost ($)	Ventilation cost ($)
200 ft by 100 ft	Traditional welding with new ventilation system	700000	50000	N/A
	Mix at the torch	109000	59000	290000
	Customized gas cylinder	44000000	Insignificant	Insignificant
	Commercial gas cylinder	126000	76000	290000
60 ft by 30 ft	Traditional welding with new ventilation system	162000	20000	N/A
	Mix at the torch	37000	20000	62000
	Customized gas cylinder	15000000	Insignificant	Insignificant
	Commercial gas cylinder	42000	25000	62000

APPENDIX B
DETAIL RESULTS OF THE MECHANICAL STRUCTURE TEST

The chemical composition analyses of the baseline weld and ASE weld are shown in Table B-1. The weight percentages of the solutes: chromium (Cr), nickel (Ni), molybdenum (Mo), manganese (Mn), and other metals were within the standard limits for the 310 stainless steel plate and wire chemical composition.

Table B-1. Composition profile of test welds and standard materials (%)

Weld ID	C	Cr	Ni	Mo	Mn	Si	P	S	Cu
Baseline weld	0.073	26.5	20.0	0.14	1.19	0.47	0.016	0.0006	0.097
ASE weld	0.081	26.0	19.7	0.14	1.21	0.47	0.020	0.0007	0.10
ER310 consumables	0.25	24.0 – 26.0	19.0 – 22.0	N/A	2.00	1.50	0.045	0.030	N/
Standard 310 Plate	0.08 – 0.15	25.0 – 28.0	20.0 – 22.5	0.75	1.0 – 2.5	0.30 – 0.65	0.03	0.03	0.75

The macrostructures of the three baseline plates are shown in Figure 4-5A~C. The microstructures of the weld zone in one baseline plate are shown in Figure B-1. No analyses were performed to determine the phases of the microstructure (Ferrite, Austenite, and Bainite). The macrostructures revealed a typical welded metal feature of columnar grains which was controlled by growth due to the high temperature, adjacent to fine grains of the parent metal, and buffered by the heat affected zone (HAZ). The macrostructures of the three baseline plates were similar and did not appear to contain any weld defects.

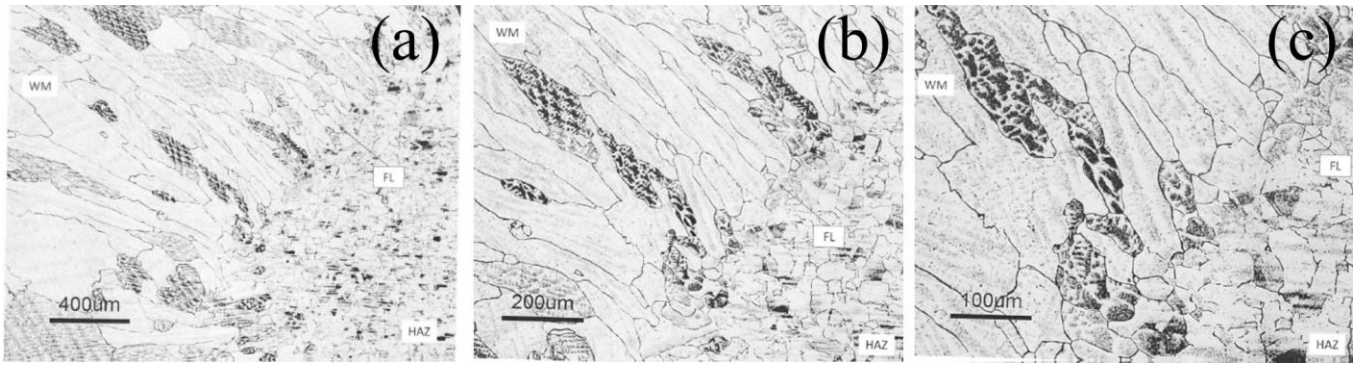

Figure B-1. Microstructure of the weld zone in one plate (a) 5×, (b) 10×, (c) 20×.

Figure B-1 reveals a microstructure of welded metal with grains of hundreds of micrometers' length adjacent to the HAZ and the fusion line (FL). The HAZ and FL are of finer grain size. The microstructures also indicated the presence of inter-metallic particles where the grains probably nucleated on them. This is a typical feature of particles affected nucleation of grains. No defects were evident in the microstructures shown.

The macrostructures of the ASE plates are shown in Figure 4-5D~F. The general features were similar to those of the baseline plates. However, a crack at the interface between the WM and the HAZ appeared and is shown in Figure 4-5E. The microstructure of this plate in Figure B2 revealed the length of the crack to be several hundred microns. The TMS addition or problems with shielding gas or improper welding technique might have caused gas pockets, which could have coalesced into a crack.

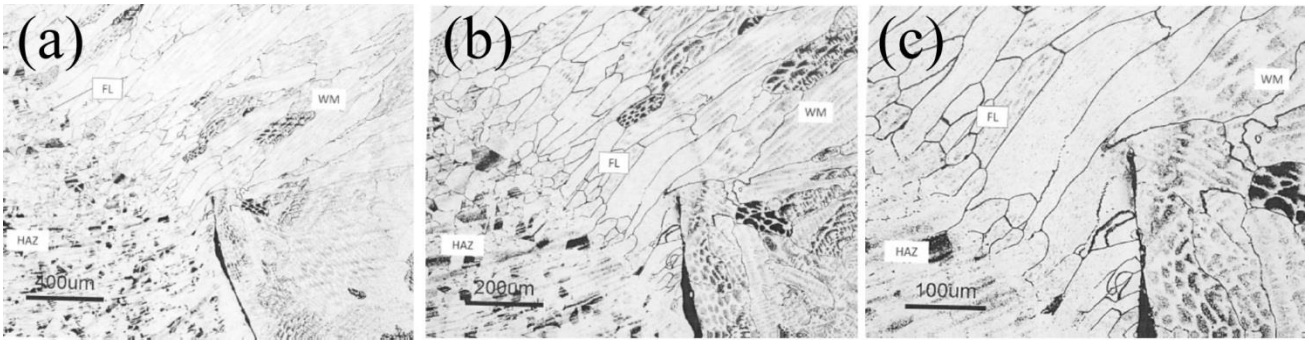

Figure B-2. Microstructure of the weld zone in sample F541 (a) 5×, (b) 10×, (c) 20×.

The tensile data are shown in Table B-2. The ultimate strength values of 5 out of 6 baseline specimens were above 80ksi, the minimum value for the E310 (AWS specification A5.4). The tensile strength of the sample that did not reach the minimum tensile strength was 75.5 ksi (94.4% of the minimum value). It should be noted that when comparing the properties of all-weld-metal (AWM) tests with those of transverse tests, the structures were different. In the AWM, there was a uniform material, while in the transverse samples were composites of base metal, HAZ, and the weld zone. These regions would stretch unequally in a tensile test, which was problematic for determining whether the mechanical tensile properties were acceptable or not. This is why yield strength and percent elongation properties are not usually reported in a transverse tensile test. The ultimate tensile strength is usually reported for comparison methods.

The results indicated that significant defects existed in all the six plates and it was equally significant that most of the specimens (5 out of 6) in the baseline and 1/3 of the ASE specimens (2 out of 6) had their tensile strength values exceed the 80 ksi minimum value. In summary, while the ASE technology does not significantly

deteriorate the mechanical quality of the welds, it probably can use some optimization of the different parameters to achieve the expected mechanical tensile parameters.

Table B-2. Tensile values of baseline and TMS test welds – 3/16” transverse tension test specimen

Standard material/Welds	YS, ksi*	UTS, ksi	El, %*
ER 310 stainless steel welding wire specification*	N/A	80	30
Baseline	44.8	86.5	37
	44.8	81.0	22
	46.2	85.5	28
	44.4	86.5	29
ASE technology	44.9	75.5	15
	43.2	84.5	32
	43.5	76.5	17
	43.7	76.5	18
	45.3	64.0	9.0
	45.1	87.5	37
	46.0	83.0	24
	44.4	73.5	16

* American Welding Society A5.9: Specification for Bare Stainless Steel Welding Electrodes and Rods.

** All the fractures in the tensile tests were ductile in the welded area. Ductile fractures are required to ensure that catastrophic brittle failures are avoided in the welded area.

APPENDIX C
CHARACTERIZATION OF MERCURY IN CEMENT KILN BAGHOUSE FILTERED DUST (BFD) AND THE RELEASE OF VAPOR PHASE MERCURY FROM CONCRETE PROCESSING WITH BFD-ADDED CEMENT

Abstract

The fate of mercury (Hg) in cement processing and products has drawn intense attention due to its contribution to the ambient emission inventory. Feeding Hg-loaded coal fly ash to the cement kiln introduces Hg into the kiln's baghouse filtered dust (BFD), and the practice of replacing 5% of cement with the Hg-loaded BFD by cement plants has raised environmental and occupational health concerns. The objective of this study was to determine Hg concentration and speciation in BFD, as well as to investigate the release of vapor phase Hg from storing and processing BFD-added cement. The results showed that Hg in the BFD from different seasons ranged 0.91~1.44 mg/kg (ppm), with 62~73% as soluble inorganic Hg, while Hg in the other concrete constituents were 1~3 orders of magnitude lower than the BFD. The time-series study showed up to 21% of Hg loss while storing the BFD in the open environment by the end of 7th day. Real-time monitoring in the bench system indicated that high temperature and moisture can facilitate Hg release at the early stage. Ontario Hydro (OH) traps showed that Hg emission from BFD is related to the air exchange surface area. In the bench simulation of concrete processing, 0.4~0.5% of Hg escaped from mixing and curing BFD-added cement. Follow-up head-space study did not detect Hg release in the following 7 days. In summary, replacing 5% of cement with the BFD investigated in this study has minimal occupational health concern for concrete workers, and proper storing and mixing of BFD with cement can minimize Hg emission burden for the cement plant.

Introduction

Fly ash from coal-fired power plants is one of the main raw materials in the pyroprocess of the Portland cement kiln,(Demirbaş 1996) and it provides the desired plasticity, permeability, sulphate resistance, and durability for cement and concrete.(Pistilli and Majko 1984; Kula et al. 2001) However, as a result of utilizing activated carbon injection in the power plant flue gas treatment system,(Hassett and Eylands 1999) coal fly ash now contains mercury (Hg) loaded carbon material. The addition of coal fly ash to the raw mill therefore leads to an undesired Hg emission from the cement kiln stack.(Mlakar et al. 2010) The Environmental Protection Agency (EPA) established the National Emission Standards for Hazardous Air Pollutants (NESHAP) and the New Source Performance Standards (NSPS) for Portland cement kilns, with a limit of 55 or 21 lb Hg emission per million tons of clinker production for the existing or new cement kiln, respectively.(USEPA 2010) To address the Hg emission issue, a filtration baghouse is typically used downstream in the cement kiln to remove the Hg-loaded dust from the flue gas.(USEPA 2011) A material flow chart in a typical cement plant is illustrated in Figure C-1. The collected kiln's baghouse filtered dust (BFD) is either landfilled or recycled back into the cement production loop.(Siddique 2006; Linero 2011) Although no adverse effect to the cement kiln and the product, the accumulated Hg in the kiln may eventually increase the Hg emission from the stack to the ambient air.(Senior et al. 2009) As the cement demand and production continue to grow(Edwards 2012) in the United States with potential economic revival and increasing construction activities, the excessive contribution to the Hg emission inventory from cement plants becomes an important issue to the environment and ecosystem.

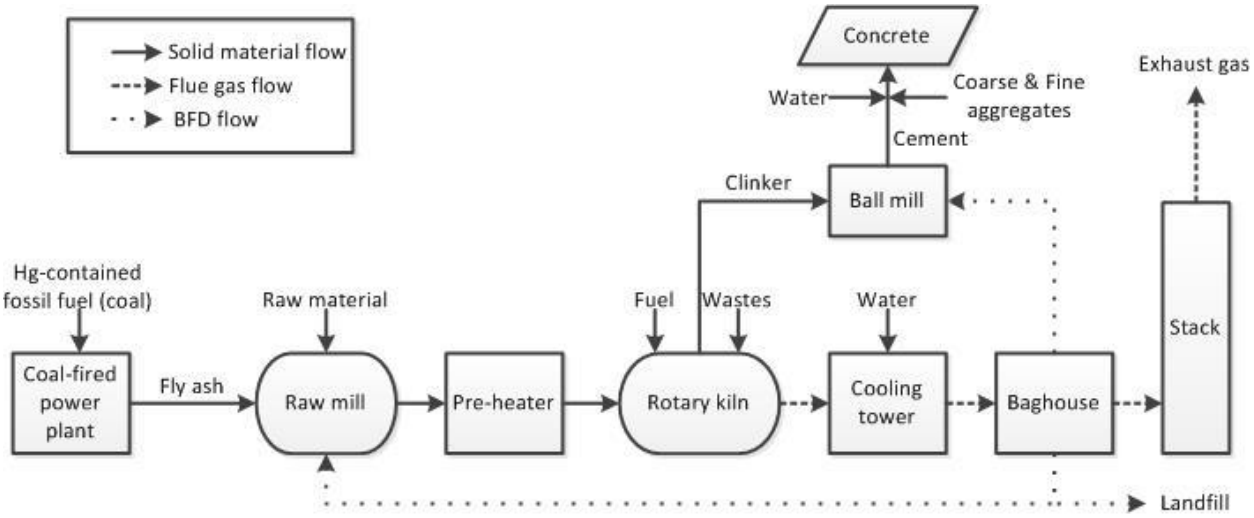

Figure C-1. Simplified material flow of a typical cement kiln. The BFD from the baghouse filter was either recycled back to the raw mill or added to the final cement product.

In lieu of recycling BFD to the kiln, some cement plants in the State of Florida have been practicing to directly add BFD to the final cement product in the ball mill. The practice is based on the hypothesis that the concrete made from the BFD-added cement can immobilize the Hg. BFD has similar property to lime, and research showed adding BFD up to 5% mass of the cement has no significant effect on the mechanical properties of concrete.(Maslehuddin et al. 2009) While this practice theoretically may reduce the Hg emission to the ambient air, few studies have investigated the environmental consequences of storing the BFD-added cement and the exposure of the workers processing the BFD-added cement. In addition, the ball mill mixing the BFD and cement may not have a dust filtration device as the rotary kiln has. This may consequently increase the Hg emission from the cement plant, due to the unfiltered flue gas.

It was reported that the total Hg concentration in the BFD is similar to the coal fly ash added to the cement kiln.(Siddique 2006) However, the recent popularity of

selective non-catalytic reduction (SNCR) devices employed in the coal-fired power plants has changed the composition of the fly ash, with more ammonia and possibly Hg. Information about Hg concentration for the other concrete constituents is also scarce. These concrete constituents may have trace level Hg due to the possibility for Hg entering these materials either in the kiln (cement) or by natural occurrence (aggregates). In addition, it is difficult to determine the speciation of Hg due to the fact that the amount of total Hg presented in these materials is at trace level. However, the environmental mobility, bio-accumulation, and toxicity of Hg all depend on the speciation. Alkyl-Hg and soluble inorganic-Hg (SI-Hg) are much more mobile and toxic than the non-soluble inorganic-Hg (NSI-Hg) that is predominantly elemental Hg.(Langford and Ferner 1999)

Among the studies with the Hg-contained cement, most focused on the leaching characteristics of curing the concrete, while very few focused on the vapor phase Hg release. A head-space study(Hamilton and Bowers 1997) showed that vapor phase Hg was released from the Hg-doped (0.2% wt/wt) solidified cement monolith. The release rate of Hg was a function of time and temperature. The study also prompted that the vapor phase Hg release from cement monolith was possibly due to moisture and temperature increase during mixing and curing. However, the study was carried out with a very high concentration of doped Hg (0.2% wt/wt) in cement which is not likely to happen in the industrial setting. Another study(Golightly et al. 2009) demonstrated that about 0.31% of total Hg was released from curing concrete, with 55% of the cement replaced by coal fly ash. A study(Goodrow et al. 2005) in New Jersey revealed that the

total Hg contribution to the atmosphere from cement-stabilized waste was negligible (<4%), although the release rate (130 kg/y) was on par with other industrial sources.

The objective of this study was to characterize the Hg concentration and speciation in the BFD as well as other concrete constituents, by using different extraction methods and high sensitivity analytical equipment. A bench system was built to simulate the storage, mixing, curing of the BFD-added cement, under different environmental conditions. Both real-time monitoring and Ontario Hydro (OH) method were used to examine the amount of vapor phase Hg released. The environmental impact and occupational hazard of adding BFD to cement were assessed.

Experimental

Material Characterization

Fresh BFD was sampled from different running seasons (Oct, 2011; Dec, 2011; Feb, 2012, Aug 2012.) of one cement kiln in the State of Florida. Commercially available Portland cement, coarse aggregate (rocks), and fine aggregate (sands) were acquired from local retail stores. All the materials were stored in either desiccators or desiccated buckets. The materials were homogenized by a rotatory drum prior to the experiment.

The digestion procedure for materials were derived based on the sequential extraction procedure described in EPA Method 3200,(USEPA 2005) while the analysis of the materials were based on EPA Method 7474.(USEPA 2007) For each type of constituent, fifteen of 0.5 g sample were weighed using an analytical scale (Sartorius MC210S, Goettingen, German) with a readability of 0.01 mg. The samples were then put into threaded cap Polytetrafluoroethylene (PTFE) tubes. 10 mL of the extraction

solvent and acids for different Hg species (listed in Table C-1) were added to the PTFE tube, with five replicates for each extraction method. The PTFE tubes were heated up to about 100 °C for 30 minutes in a microwave digestion system (CEM MDS 81D, Matthews, NC). The digests were diluted with deionized (DI) water to a pre-determined level, to accommodate the upper/lower detection limits of the analytical instruments. The diluted solution was transferred into a 50 mL centrifuge tube and analyzed by a hydride generation - atomic fluorescence spectrometer (HG-AFS) (Aurora Biomed 3300, Vancouver, BC, Canada). The detection limit of the HG-AFS was around 1 ng/mL. The Hg concentration in each type of samples was averaged from the five replicates.

Table C-1. Hg classification in this study

	Hg Species	Environmental mobility	Toxicity	Extraction
Soluble inorganic Hg (SI-Hg)	Hg^{2+} ($HgCl_2$, $HgSO_4$, HgO, $Hg(NO_3)_2$, $Hg(OH)_2$)	Mobile	Toxic	10% HCl
Alkyl Hg	Methyl Hg, Ethyl Hg	Mobile	Highly toxic	Toluene
Non-soluble inorganic Hg (NSI-Hg)	Hg^0 HgS, Hg_2Cl_2	Semi-mobile Non-mobile	Less toxic Less toxic	Calculated from mass balance
Total Hg	All of the above			Aqua regia (HNO_3: HCl, 1:3 v/v)

In addition to the characterization, a 7-day time-series study was carried out on two batches of the BFD (Oct, 2011; Dec, 2011) to evaluate the Hg loss from the BFD, by exposing them to natural weather (~30 °C, 60~70% relative humidity). The BFD was laid down on a flat surface as a thin layer and left outdoors. A small portion of the sample was fetched on a daily basis during the 7-day period. The retrieved sample was dried in the desiccator to remove excessive water absorbed on the BFD, digested and

analyzed by HG-AFS. The condition was used to simulate storing the BFD in an open area with indefinite head-space.

Bench System

Real-time measurement of vapor phase Hg release from the materials and concrete processing were performed separately in a small enclosed cylindrical tube and air-tight glove box (Plas Lab 818-GB, Lansing, MI) with an interior volume of 489 L. The conceptual illustration of the bench system is shown in Figure C-2. In Figure C-2A, gas flows from two air cylinders were mixed at a mixing chamber to create a total flow of 1~2 liter per minute (Lpm). The ratio of flow rates between water saturated air and dry air was used to control the relative humidity (RH), which was monitored by a hygrometer (Omega HX94C, Stamford, CT) inside the mixing chamber. The gas stream then went through either apparatus in Figure C-2B or C-2C, depending on whether measuring vapor phase Hg release from the materials or concrete processing. The small enclosed cylindrical tube with heating tape wrapped around (Figure C-2B) was used to test vapor phase Hg release from the BFD, cement, and BFD/Cement mixture under given flow rate, RH, and temperature. This limited head space study was to simulate storing the BFD in an enclosed environment. Simulation of concrete processing was carried out in the glove box shown in Figure C-2C. Thermometers mounted in the cylindrical tube and inside the concrete were used to monitor the temperature during the earlier stage of mixing.

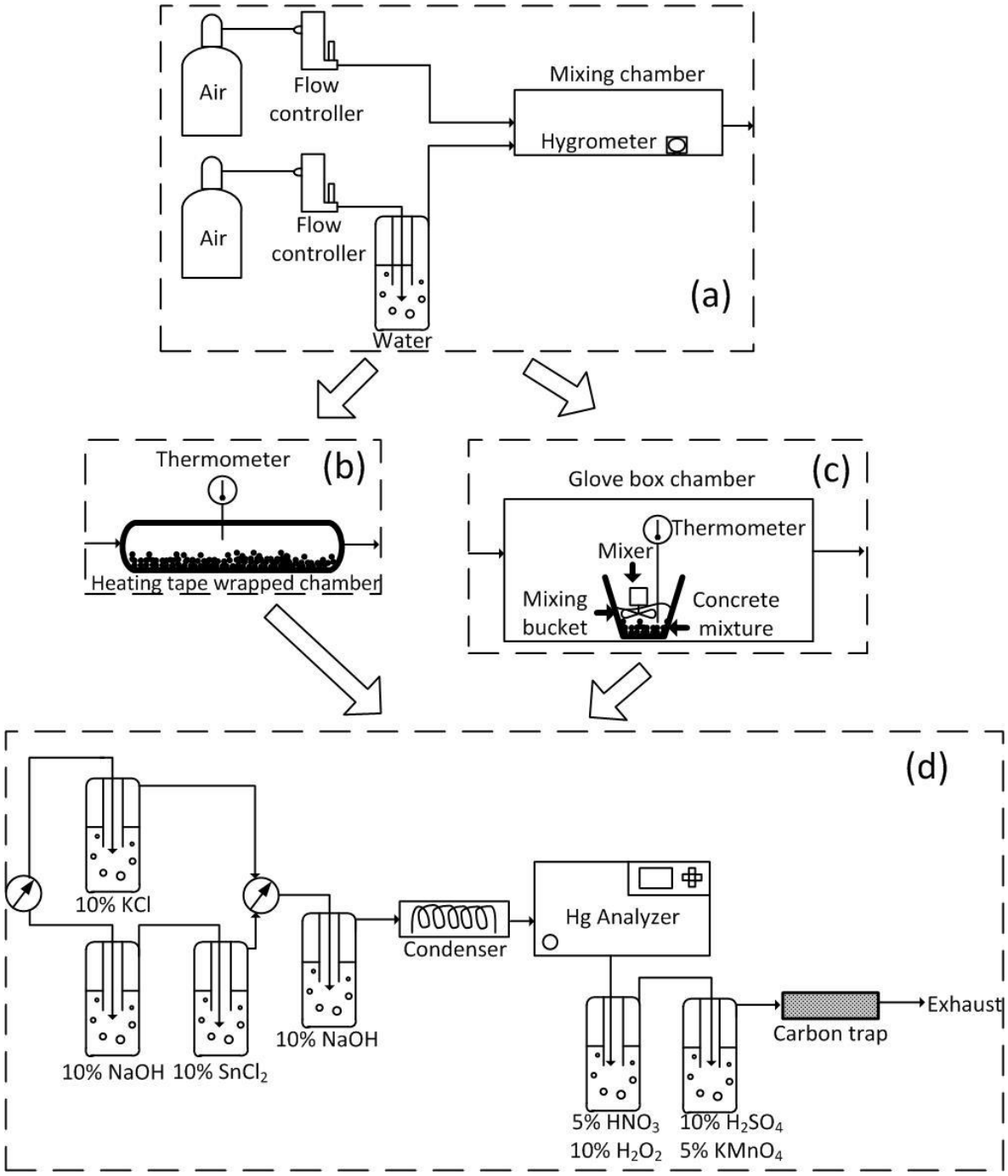

Figure C-2. Breakdown schematic diagram of the bench system. A) controlled humidified air generator. B) temperature controlled tube. C) glove box with concrete processing inside. D) Hg transformation unit, real-time Hg analyzer, and OH trap.

The gas stream carrying any released vapor phase Hg was sent through a Hg transformation unit (Figure C-2D) developed in a previous study.(Li and Wu 2006) By

switching to 10% potassium chloride (KCl) solution, the soluble inorganic Hg (SI-Hg) was absorbed in the impinger, while only non-soluble inorganic Hg (NSI-Hg) passed the unit. On the other channel, SI-Hg was reduced to Hg^0 by 10% tin(II) chloride ($SnCl_2$) solution. In this channel, all the vapor phase Hg passed through the unit. The measured difference of these two channels was the amount of SI-Hg. 10% sodium hydroxide (NaOH) solution in the unit removed any acidic gas, and a condenser reduced the moisture content in the gas stream. Both were to prevent potential damage to the Hg analyzer. A real-time Hg analyzer (Ohio Lumex RA915+, Twinsburg, OH) monitored the Hg concentration in the gas stream, with a resolution of 2 ng /m^3 s. The Hg analyzer was calibrated using a Hg permeation device (VICI Metrics Dynacal, Poulsbo, WA) which can release Hg^0 vapor at a constant rate. The analyzer was zeroed using ultrahigh purity nitrogen cylinder gas prior to each test.

The vapor phase Hg passed the Zeeman atomic absorption spectrometer in the real-time Hg analyzer, and then entered the Ontario Hydro (OH) trap. Since SI-Hg was either removed or reduced by the Hg transformation unit, the original OH sampling train was modified to skip the 10% KCl solution impingers. 100 mL of hydrogen peroxide (H_2O_2) solution and 100 mL potassium permanganate ($KMnO_4$) solution with acids were used to collect Hg^0. 10% KCl solution was added to the $KMnO_4$ trap solution after the sampling, to remove the SO_2 produced from the reaction. The OH trap was diluted and immediately analyzed by a cold vapor - atomic fluorescence spectrometer (CV-AFS) (Tekran 2600, Toronto, ON, Canada). The CV-AFS with a detection limit of 1 pg/mL was capable of detecting trace amount of Hg in the OH traps.

The bench system was used for the first 24 hours due to two reasons: the data record length limit of the real-time Hg analyzer, and instability of Hg in the OH trap while feeding continuous air.(Laudal and Heidt 1997) A long-term head-space experiment was therefore performed using the glove box as a supplement to the 24 hour study. The solidified concrete was put into the box without air exchange. After a pre-set period, vacuum was used to pull 20 L air from the glove box through the OH trap. The concentration in the OH trap was used to calculate the Hg vapor released from the solidified concrete.

Test Conditions

500 g each of BFD, cement, and 5% BFD/95% cement was weighed and laid on the bottom surface of the cylindrical tube in Figure C-2B. In addition to 500 g of BFD, 100 g of BFD was also tested, which had a similar surface area exposed to the air flow in the cylindrical tube (Figure C-3). Two flow rates (1 and 2 Lpm) and four relative humitidties (0%, 25%, 75%, 100%) were employed. The temperature in the tube was either room temperature (~23 °C) or elevated by the heating tape (~80 °C). This experiment was designed to identify the potential effect of environmental parameters on storing BFD and cement prior to handling.

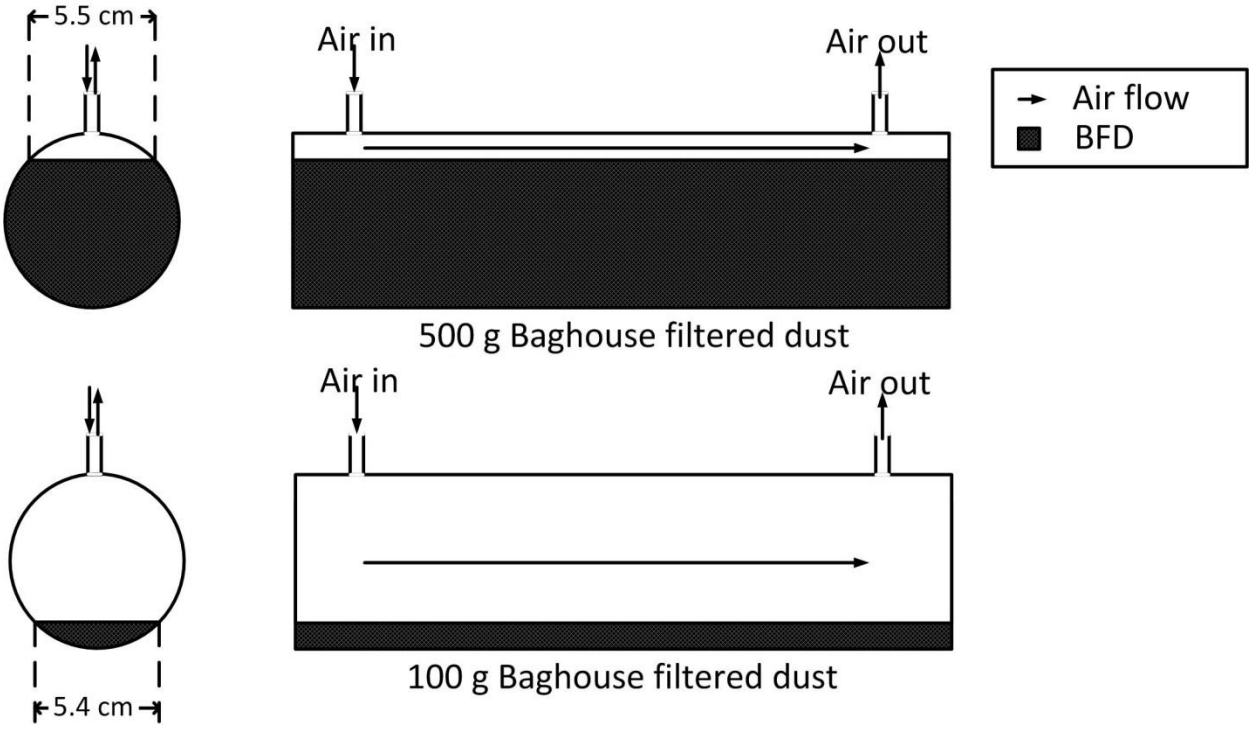

Figure C-3. Cross sectional and lateral view of the cylindrical tube loaded with 500 g and 100 g BFD

Simulation of concrete processing was conducted in the glove box in Figure C-2C using Feb, 2012 BFD sample. The mixing ratio of different constituents followed the original recipe for Portland cement concrete(Kosmatka et al. 2002). The recipe of concrete was scaled down to fit the size of the glove box and is listed in Table C-2. Different from the simulation of storage, the gas stream's RH was fixed at 50%. During concrete processing, large amount of water was supplied to the mixture and the relative humidity was already at 100%. Air exchange rate of the glove box was set to 1.5 Lpm. The stirring of BFD, cement, water, and aggregates using a hand mixer lasted about 3 minutes, while the concrete remained undisturbed and became completely solidified in 8 hours. The concrete processing was repeated five times using 5%BFD/95% cement mixture and 10% BFD/90% cement mixture, respectively. After 24 hours of curing, one

of the concretes from each mixing ratio was subjected to a 7-day head-space study with OH trap.

Table C-2. The recipe of the Portland cement concrete (kg) used in this study

Constituent	5% BFD/95% Cement	10% BFD/90% Cement
Water	0.54	0.54
BFD	0.05	0.10
Cement	0.95	0.90
Coarse aggregates	1.82	1.82
Fine aggregates	1.45	1.45
Total	4.81	4.81

Quality Control and Statistics

All the solutions and dilution were made with DI water from a Nanopure system (Barnstead Nanopure D11901, Waltham, MA) with a conductivity of 18.2 mΩ-cm. The chemicals used were analytical grade or higher in purity. The reservoir, bench system components, and tubing used in the study were ultrasonically cleaned to remove any residues. Pressurized air leak test was performed before conducting each experiment.

The calibration curve for the Hg analysis was prepared by diluting high-purity 1000 mg/L solutions (Ricca Chemical, Arlington, TX) with an R^2 equal to or larger than 0.9999. Lab blank (10% HCl solution) was randomly inserted to sample batch of the HG-AFS and the CV-AFS to examine signal drift, residues, and background Hg level. All the samples were at least triplicates and the results were averaged. *t*-test was used to examine the results from different samples using a significance level of $p = 0.05$. Statistical analyses were performed using the statistical software package (SAS 9.3, Cary, NC).

Results and Discussion

Hg Concentration and Speciation in the Materials

Table C-3 lists the Hg concentration and speciation in the BFD, cement, and other constituents in the concrete processing. Alkyl-Hg was below the detection limit in all the samples, and therefore was eliminated from following studies. The high temperature and combustion condition in the cement kiln may decompose any organic phase compounds.

Table C-3. Hg concentration and speciation in the concrete constituents

Material		Total Hg (μg/kg)	SI-Hg (mg/kg)	Percentage of SI-Hg (%)
BFD	Oct 2011	910 ± 60	560 ± 20	61.5
	Dec 2011	1430 ± 70	1050 ± 40	73.4
	Feb 2012	1520 ± 90	990 ± 100	65.4
	Aug 2012	1440 ± 230	1030 ± 100	71.5
Cement		74.51 ± 6.24	47.02 ± 8.94	63.1
Coarse aggregates (rocks)		4.32 ± 1.52	2.63 ± 1.16	60.8
Fine aggregates (sand)		0.44 ± 0.06	0.33 ± 0.04	73.2

The total Hg concentration in the BFD ranged from 0.91~1.52 mg/kg (ppm) and was consistent in each season. More mobile and toxic SI-Hg counted about 61.54~73.43% of total Hg in the samples, while the rest was in NSI-Hg phase. The total Hg concentration in the BFD was higher than previously measured value of 0.66 mg/kg (mean) in the cement kiln dust by Portland Cement Association (PCA).(PCA 1992) It should be noted that Hg concentration in the BFD measured by PCA has a large deviation with some samples having up to 25.50 mg/kg total Hg. The BFD from different cement kiln plants does not have the same characteristics. The variance of Hg in fed coal fly ash, raw materials, wastes, fuels could contribute to the difference among different seasons of the same cement plant.

The total Hg concentration was 74.51 µg/kg (ppb) in the commercial cement. It was about one order of magnitude lower than the BFD. When mixing 5% of BFD with 95% of cement, the significance of Hg contributed from BFD diminished due to the small proportion. The concentration in the cement was also higher than the available studies(Pistilli and Majko 1984; PCA 1992) in past decades; the latter showed Hg in the cement was averaging below 14 µg/kg with the highest to be 39 µg/kg.

The aggregates in the concrete processing showed much less Hg presence compared to the BFD and the cement. The coarse aggregates (rocks) and the fine aggregates (sands) had 4.32 µg/kg and 0.44 µg/kg of total Hg. Hg in the sands was just slightly above the detection limit of CV-AFS. Those constituents were naturally occurring materials and the characteristic can substantially vary from different geological locations. All the constituents had a relative constant SI-Hg/Total Hg ratio of 0.6~0.7.

Vapor Phase Hg Released from the BFD and Cement (Bench System)

Figure C-4 shows the change of Hg concentration in the 7-day time-series study in the open area using the BFD. The vaporization of NSI-Hg loss was significant on the first day, from 0.36 mg/kg to 0.27 mg/kg for Oct, 2011 sample, and from 0.25 mg/kg to 0.15 mg/kg for Dec, 2011 sample. The concentration of NSI-Hg stayed relatively unchanged afterward. The SI-Hg remained constant during the 7-day period. The total Hg loss was 13.83~17.52% on the first day, while 20.21~21.16% during the 7-day period, mostly contributed from NSI-Hg vaporization. This corresponded to 30.77~57.14% on the first day and 43.59~65.71% during the 7-day of the total NSI-Hg in the samples.

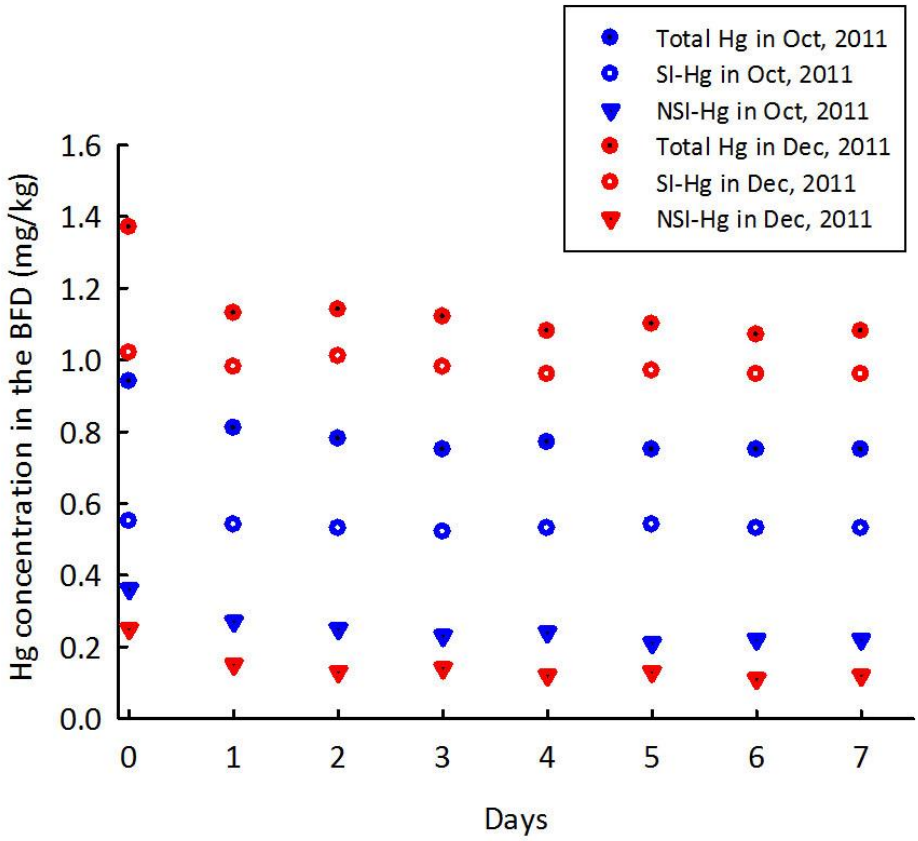

Figure C-4. Total Hg, SI-Hg, and NSI-Hg concentration in the 7-day time-series study.

Figure C-5 shows the total Hg concentration in the gas stream as a function of time in 24 hours in the bench system for the BFD samples. Generally, significant Hg release was detectable only in the first 2 hours after experiment started. The concentration was at the background level (2 ng/m^3 s) afterward. High RH and temperature facilitated the Hg release in the earlier stage, while the gas flow rates did not affect the release pattern. High temperature increased the diffusion activity while lowering the adsorption affinity between Hg and the dust. Water in high moist air may compete with Hg on adsorption surface.(Li et al. 2011) Hg speciation results are not presented in Figure 5, due to the fact that early detectable release was mostly NSI-Hg, i.e. switching the channel in the Hg-transformation unit gave an identical result. The Hg

analyzer could not detect any significant release from the cement and the 5% BFD/95% cement mixture under all experimental conditions. This was due to the lower total Hg concentration in these materials.

Averagely, 1.6±0.4% of Hg in the 500 g BFD was released as vapor phase, while almost all released Hg was in NSI-Hg phase (p<0.05). The amount of total Hg released from the BFD and consequently captured by OH trap in different experimental condition is listed in Table C-4. There was no statistical correlation found between total Hg released with any environmental parameter. This indicated the total Hg released in 24 hours were independent of gas flow rate, temperature, and RH. Furthermore, the amount of Hg released from 500 g and 100 g BFD were identical, regardless the mass difference in total Hg. It was possibly due to their similar area of air exchange (Figure C-3). This suggests the release was limited to the top layer and the corresponding effective thickness was calculated to be 0.12 cm. This implies that the release of Hg from BFD can be correlated to the degree of contact between air and dust.

The amount of Hg released from the cement was below the detection limit at most environmental conditions, due to the low Hg concentration in the cement. Similarly, the 5% BFD/95% cement mixture did not show any detectable vapor phase Hg released. The higher concentration of Hg and porous structure of the BFD likely contributed to the higher vapor phase Hg released and captured by the OH traps.

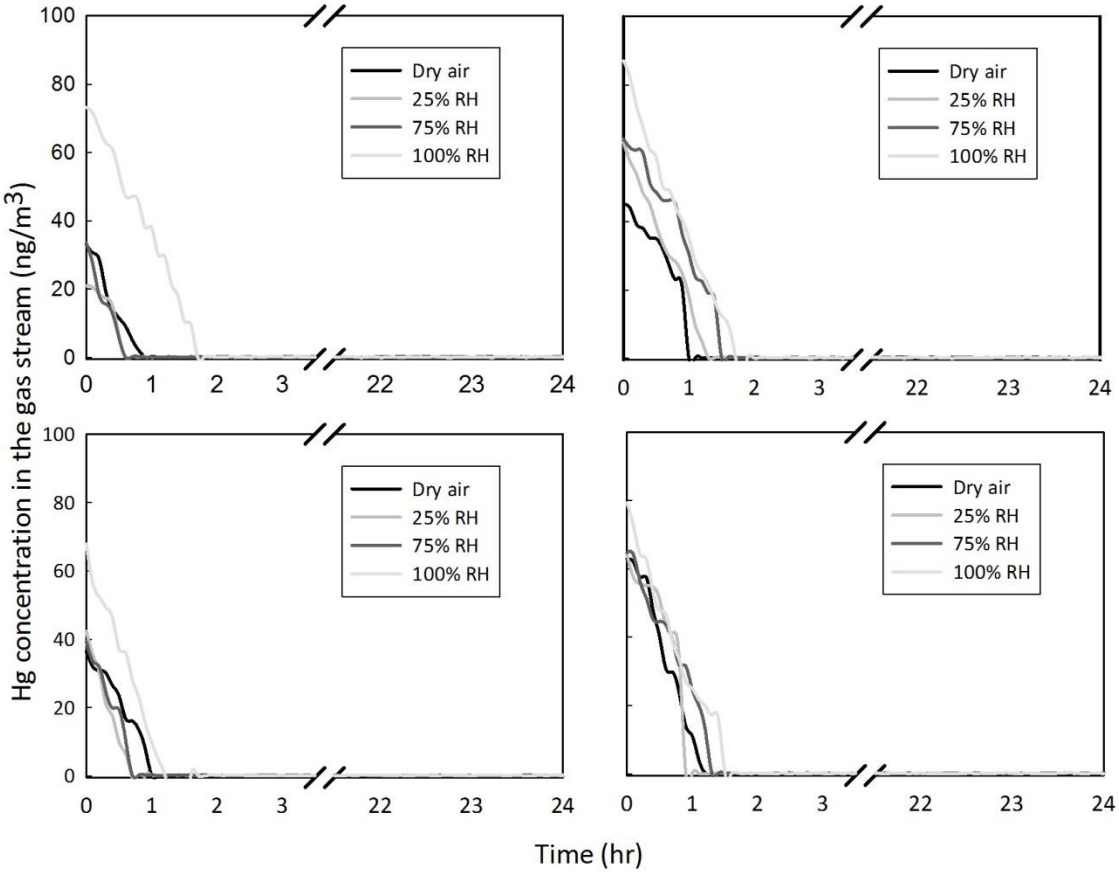

Figure C-5. Hg released from the BFD as a function of time. A) 1 Lpm gas flow rate and room temperature. B) 1 Lpm gas flow rate and elevated temperature. C) 2 Lpm gas flow rate and room temperature. D) 2 Lpm gas flow rate and elevated temperature.

Table C-4. Total Hg (µg) released from the BFD under different experimental conditions, in the OH trap

Amount of BFD	Air flow rate	Temperature	Dry air	25% RH	75% RH	100% RH
500 g	1 Lpm	23 °C	18 (2.4%)*	9 (1.2%)	10 (1.3%)	15 (2.0%)
		80 °C	11 (1.5%)	5 (1.3%)	13 (1.7%)	7 (0.9%)
	2 Lpm	23 °C	13 (1.7%)	18 (2.4%)	14 (1.8%)	13 (1.7%)
		80 °C	11 (1.5%)	11(1.5%)	11 (1.5%)	13 (1.7%)
100 g	2 Lpm	80 °C				13 (8.7%)

* The percentage in the parenthesis denotes total Hg released versus total Hg in the 500 g or 100 g Feb, 2012 BFD.

Vapor Phase Hg Release during Concrete Curing

The release of Hg from mixing and curing cement was more complicated than the BFD and the cement. The mixing process involved several minutes of high speed blending and numerous bubbles were created in the mixtures. Considerable amount of water was added into the mixture during this process. However, the temperature was raised only about 11 °C during the mixing, which could be considered to be negligible. In this study, the BFD and the cement contributed 1% and 20% mass balance to the concrete mixture, respectively. The rest of the concrete mixture was coarse and fine aggregates, which contained much less Hg. The total mass of concrete constituents was 4.8 kg for each batch of experiment and the material contained about 0.15~0.22 mg of total Hg, from the calculation using mass fraction in Table C-2 and Hg concentration in Table C-3.

During the mixing and curing of the 5% BFD/95% cement and the 10%BFD/90% cement, there was no detectable Hg release activity from the real-time monitoring. It may be due to the lower total Hg content in the concrete mixture (3.4 times less) than the 100% BFD. Total Hg released from the 10% BFD/90% cement mixture captured by the OH trap was 0.8±0.09 µg, slightly higher than 0.7±0.07 µg from the 5% BFD/95% cement mixture (p<0.05). Again, all total Hg released was in NSI-Hg phase (p<0.05). The total Hg released from the concrete mixing was about 0.4~0.5% of the total Hg in the concrete constituents. This was higher than the study(Golightly et al. 2005) using coal fly ash-added cement, while the latter had 0.1% of Hg escaped. Powdered activated carbon in coal fly ash was usually not saturated with Hg due to low Hg-carbon ratio,(Galbreath and Zygarlicke 2000) and it increased the ability of retaining Hg in the

dust, thus possibly led to the difference between study results. There was no detectable Hg in the OH trap for the 7-day head-space study on solidified concrete. It indicated that the majority of Hg release occurred in the first 24 hour.

Impact on the Ambient and Occupational Environment

From the experimental results, storing BFD in an open area contributed the highest Hg loss up to 21%. The Hg loss is related to the degree of contact between air and BFD, i.e., area of air exchange surface. Hence, it is recommended that cement kiln plant store unused BFD in a closed area to avoid additional Hg emission from the plant.

The ball mill where clinkers are grinded and BFD is added to the final product is constantly rotating. Thus, it creates good mixing between air and BFD. All the volatile Hg (NSI-Hg) can be possibly released from rotating and feeding air. However, there will be likely minimum oxidized Hg (SI-Hg) loss due to the low temperature profile (~240 °F/116 °C) of the ball mill. Based on mass balance, there would be 30 lb of additional Hg emitted from the ball mill per million ton of cement produced, by adding 5% of BFD containing 1 mg/kg of Hg content to the ball mill, assuming conservatively all the 30% NSI-Hg is released. This is above the EPA limit of 21 lb per million tons of clinker produced.(USEPA 2010) Therefore, it is recommended that the plant should direct the flue gas from the ball mill to a Hg-removal device to prevent undesired emission of Hg to the ambient air. The worst case scenario is that if the 73 million tons of cement US produced(USGS 2013) in 2012 all contained 5% BFD, and without Hg-removal device attached. This would create 2190 lb additional Hg emission. This is significant compared to the total Hg emission of 9658.2 lb in 2008(EPA 2012) from the cement industry as estimated by EPA.

During concrete curing and after being solidified, less than 0.5% of Hg was released in the vapor phase. Assuming 5% of the cement is replaced with the BFD containing 1 mg/kg of Hg, about 0.05 mg Hg per ton of concrete could be released. In a typical scenario of workers placing and finishing the concrete floor (about 16.5 ton concrete) in an enclosed room (6.72 m in length, 5 m in width, 3 m in height), the maximum ceiling concentration of Hg is less than 0.01 mg/m^3, if no ventilation at all. This is much lower than the permissible exposure limit (PEL) of 0.1 mg Hg/m^3 ceiling concentration set by the Occupational Safety and Health Administration (OSHA). (OSHA 2006b) For an outdoor concrete curing scenario, the Hg will be instantly diluted by ambient air and should cause no violation to the PEL.

In summary, caution should be exercised how the BFD should be stored and mixed to minimize Hg emission to the environment. Meanwhile, the occupational exposure is minimal while replacing 5% of the cement with the BFD containing Hg concentration around 1 ppm. It should be noted that the total Hg concentration in the concrete constituents may vary from geological location, hence affecting the released amount. Understanding the mechanism how Hg is trapped in the concrete will provide knowledge how to avoid potential release from concrete in the long term. Field study is also essential to validate the laboratory study of vapor phase Hg release in the cement plant and concrete processing site.

Acknowledgements

The study was funded by the Florida Department of Transportation (FDOT) through contract BDK75-977-50. The authors would like to thank Mr. Oliver H. Sohn and

Mr. Eduardo R. Ferrer for assisting the sample and data collection. The authors are also grateful to Mr. Al Linero of Florida Department of Environmental Protection for his valuable input.

LIST OF REFERENCES

ACGIH (2012). Documentation of the Threshold Limit Values and Biological Exposure Indices, Cincinnati, OH.

Anderson, R. A. (1997). Chromium as an essential nutrient for humans. Regul. Toxicol. Pharm. 26:S35-S41.

Antonini, J., Taylor, M., Zimmer, A. and Roberts, J. (2003). Pulmonary Responses to Welding Fumes: Role of Metal Constituents. J. Toxicol. Environ. Health Part A 67:233-249.

Antonini, J. M., Clarke, R. W., Murthy, G. G. K., Sreekanthan, P., Jenkins, N., Eagar, T. W. and Brain, J. D. (1998). Freshly Generated Stainless Steel Welding Fume Induces Greater Lung Inflammation in Rats as Compared to Aged Fume. Toxicol. Lett. 98:77-86.

Antonini, J. M., Keane, M., Chen, B. T., Stone, S., Roberts, J. R., Schwegler-Berry, D., Andrews, R. N., Frazer, D. G. and Sriram, K. (2011). Alterations in welding process voltage affect the generation of ultrafine particles, fume composition, and pulmonary toxicity. Nanotoxicology 5:700-710.

Antonini, J. M., Stone, S., Roberts, J. R., Chen, B., Schwegler-Berry, D., Afshari, A. A. and Frazer, D. G. (2007). Effect of Short-term Stainless Steel Welding Fume Inhalation Exposure on Lung Inflammation, Injury, and Defense Responses in Rats. Toxicol. Appl. Pharmacol. 223:234-245.

ASTM (2011a). E8/E8M-11: Standard Test Methods for Tension Testing of Metallic Materials.

ASTM (2011b). E1019: Standard Test Methods for Determination of Carbon, Sulfur, Nitrogen, and Oxygen in Steel, Iron, Nickel, and Cobalt Alloys by Various Combustion and Fusion Techniques.

Aston, J. G., Kennedy, R. M. and Messerly, G. H. (1941). the heat capacity and entropy, heats of fusion and vaporization and the vapor pressure of silicon tetramethyl. J. Am. Chem. Soc. 63:2343-2348.

Atanassova, D., Stefanova, V. and Russeva, E. (1998). Co-precipitative pre-concentration with sodium diethyldithiocarbamate and ICP-AES determination of Se, Cu, Pb, Zn, Fe, Co, Ni, Mn, Cr and Cd in water. Talanta 47:1237-1243.

ATSDR (2008a). Draft toxicological profile for chromium, HHS, ed., Atlanta, GA.

ATSDR (2008b). Draft toxicological profile for manganese, HHS, ed., Atlanta, GA.

ATSDR (2005). Toxicological profile for nickel, HHS, ed., Atlanta, GA.

AWS (2012). A5.9 Specification for Bare Stainless Steel Welding Electrodes and Rods, American Welding Society.

AWS (1998). B4.0 Standard Methods for Mechanical Testing of Welds, American Welding Society.

AWS (2006). F1.2:2006 Laboratory Method for Measuring Fume Generation Rates and Total Fume Emission of Welding and Allied Processes, American Welding Society.

Biswas, P., Owens, T. M. and Wu, C.-Y. (1995). Control of toxic metal emissions from combustors using vapor phase sorbent materials. J. Aerosol Sci. 26:S217-S218.

Biswas, P. and Wu, C.-Y. (1998). Control of toxic metal emissions from combustors using sorbents: A review. J. Air Waste Manage. Assoc. 48:113.

Biswas, P. and Wu, C.-Y. (2005). Nanoparticles and the Environment. J. Air Waste Manage. Assoc. 55:708-746.

Biswas, P., Wu, C.-Y., Zachariah, M. R. and McMillin, B. (1997). Characterization of Iron Oxide-silica Nanocomposites in Flames: Part II. Comparison of Discrete-sectional Model Predictions to Experimental Data. J. Mater. Res. 12:714-772.

Biswas, P. and Zachariah, M. R. (1997). In situ immobilization of lead species in combustion environments by injection of gas phase silica sorbent precursors. Environ. Sci. Technol. 31:2455-2463.

BLS (2008). National employment matrix, US Department of Labor, Washington, DC.

Boevski, I., Daskalova, N. and Havezov, I. (2000). Determination of barium, chromium, cadmium, manganese, lead and zinc in atmospheric particulate matter by inductively coupled plasma atomic emission spectrometry (ICP-AES). Spectrochim. Acta, Part B 55:1643-1657.

Castner, H. R. and Null, C. L. (1998). Chromium, Nickel and Manganese in Shipyard Welding Fumes. Weld. J. 77:223-231.

CDC (2008). National occupational research agenda: Construction.

Chen, J.-C., Wey, M.-Y. and Ou, W.-Y. (1999). Capture of heavy metals by sorbents in incineration flue gas. Sci. Total Environ. 228:67-77.

Cho, H.-W., Yoon, C.-S., Lee, J.-H., Lee, S.-J., Viner, A. and Johnson, E. W. (2011). Comparison of Pressure Drop and Filtration Efficiency of Particulate Respirators using Welding Fumes and Sodium Chloride. Ann. Occup. Hyg. 55:666-680.

Correa-Duarte, M. A., Giersig, M. and Liz-Marzán, L. M. (1998). Stabilization of CdS Semiconductor Nanoparticles Against Photodegradation by a Silica Coating Procedure. Chem. Phys. Lett. 286:497-501.

Costantini, L. M., Gilberti, R. M. and Knecht, D. A. (2011). The Phagocytosis and Toxicity of Amorphous Silica. PLoS ONE 6:e14647.

Craig, B. D. and Anderson, D. S. (1995). Handbook of corrosion data. ASM International, Materials Park, OH.

Dams, R., Rahn, K. A. and Winchester, J. W. (1972). Evaluation of filter materials and impaction surfaces for nondestructive neutron activation analysis of aerosols. Environ. Sci. Technol. 6:441-448.

Demirbaş, A. (1996). Optimizing the physical and technological properties of cement additives in concrete mixtures. Cem. Concr. Res. 26:1737-1744.

Dennis, J. H., French, M. J., Hewitt, P. J., Mortazavi, S. B. and Redding, A. J. (1996). Reduction of hexavalent chromium concentration in fumes from mteal cored arc welding by addition of reactive metals. Ann. Occup. Hyg. 40:339-344.

Dennis, J. H., French, M. J., Hewitt, P. J., Mortazavi, S. B. and Redding, C. A. J. (2002). Control of Exposure to Hexavalent Chromium and Ozone in Gas Metal Arc Welding of Stainless Steels by Use of A Secondary Shield Gas. Ann. Occup. Hyg. 46:43-48.

Dennis, J. H., Mortazavi, S. B., French, M. J., Hewitt, P. J. and Redding, C. R. (1997). The effects of welding parameters on ultraviolet light emissions, ozone and CrVI formation in MIG welding. Ann. Occup. Hyg. 41:95-104.

Dulski, T. R. (1996). A manual for the chemical analysis of metals. ASTM, West Conshohocken, PA.

E.P.A., U. S. (1996). EPA Method 3052, Microwave Assisted Digestion of Siliceous and Organically based Matrices, U.S. Government Printing Office, Washington, DC.

Ebrahimnia, M., Goodarzi, M., Nouri, M. and Sheikhi, M. (2009). Study of the effect of shielding gas composition on the mechanical weld properties of steel ST 37-2 in gas metal arc welding. Mater. Des. 30:3891-3895.

Edwards, P. (2012). Cement in the USA, in Global Cement Magazine.

EPA (2012). 2008 National emissions inventory data & documentation.

Filgueiras, A. V., Capelo, J. L., Lavilla, I. and Bendicho, C. (2000). Comparison of ultrasound-assisted extraction and microwave-assisted digestion for determination of magnesium, manganese and zinc in plant samples by flame atomic absorption spectrometry. Talanta 53:433-441.

Flynn, M. R. and Susi, P. (2012). Local Exhaust Ventilation for the Control of Welding Fumes in the Construction Industry - A Literature Review. Ann. Occup. Hyg. 56:764-776.

Flynn, M. R. and Susi, P. (2009). Neurological Risks Associated with Manganese Exposure from Welding Operations - A Literature Review. Int. J. Hyg. Environ. Health 212:459-469.

Frederick, W. J., Ling, A., Tran, H. N. and Lien, S. J. (2004). Mechanisms of sintering of alkali metal salt aerosol deposits in recovery boilers. Fuel 83:1659-1664.

Fu, W., Yang, H., Hari, B., Liu, S., Li, M. and Zou, G. (2006). Preparation and characteristics of core-shell structure cobalt/silica nanoparticles. Mater. Chem. Phys. 100:246-250.

Galbreath, K. C. and Zygarlicke, C. J. (2000). Mercury transformations in coal combustion flue gas. Fuel Process. Technol. 65–66:289-310.

Geiser, M. and Kreyling, W. (2010). Deposition and Biokinetics of Inhaled Nanoparticles. Part. Fibre Toxicol. 7:2.

Golightly, D. W., Cheng, C.-M., Weavers, L. K., Walker, H. W. and Wolfe, W. E. (2009). Fly ash properties and mercury sorbent affect mercury release from curing concrete. Energy Fuels 23:2035-2040.

Golightly, D. W., Sun, P., Cheng, C.-M., Taerakul, P., Walker, H. W., Weavers, L. K. and Golden, D. M. (2005). Gaseous mercury from curing concretes that contain fly ash: laboratory measurements. Environ. Sci. Technol. 39:5689-5693.

González, P., Fernández, D., Pou, J., García, E., Serra, J., León, B. and Pérez-Amor, M. (1992). Photo-induced Chemical Vapour Deposition of Silicon Oxide Thin Films. Thin Solid Films 218:170-181.

Goodrow, S. M., Miskewitz, R., Hires, R. I., Eisenreich, S. J., Douglas, W. S. and Reinfelder, J. R. (2005). Mercury emissions from cement-stabilized dredged material. Environ. Sci. Technol. 39:8185-8190.

Graf, C., Vossen, D. L. J., Imhof, A. and van Blaaderen, A. (2003). A General Method To Coat Colloidal Particles with Silica. Langmuir 19:6693-6700.

Gray, C. N., Goldstone, A., Dare, P. R. M. and Hewitt, P. J. (1983). The evolution of hexavalent chromium in metallic aerosols. Am. Ind. Hyg. Assoc. J. 44:384 - 388.

Gullett, B. K. and Raghunathan, K. (2002). Reduction of Coal-Based Metal Emissions by Furnace Sorbent Injection. Energy Fuels 8:1068-1076.

Guo, B., Yim, H., Khasanov, A. and Stevens, J. (2010). Formation of Magnetic FexOy/Silica Core-Shell Particles in a One-Step Flame Aerosol Process. Aerosol Sci. Technol. 44:281 - 291.

Hall, S. R., Davis, S. A. and Mann, S. (1999). Co-condensation of organosilica hybrid shells on nanoparticle templates: a direct synthetic route to functionalized core-shell colloids. Langmuir 16:1454-1456.

Hamilton, W. P. and Bowers, A. R. (1997). Determination of acute Hg emissions from solidified/stabilized cement waste forms. Waste Manage. 17:25-32.

Hansen, K. and Stern, R. M. (1985). Welding fumes and chromium compounds in cell transformation assays. J. Appl. Toxicol. 5:306-314.

Harris, R. C., Lundin, J. I., Criswell, S. R., Hobson, A., Swisher, L. M., Evanoff, B. A., Checkoway, H. and Racette, B. A. (2011). Effects of Parkinsonism on Health Status in Welding Exposed Workers. Parkinsonism Relat. Disord. 17:672-676.

Hassett, D. J. and Eylands, K. E. (1999). Mercury capture on coal combustion fly ash. Fuel 78:243-248.

Hewett, P. (1995). The Particle Size Distribution, Density and Specific Surface Area of Welding Fumes from SMAW And GMAW Mild-steel and Stainless-steel Consumables. Am. Ind. Hyg. Assoc. J. 56:128-135.

Hewitt, P. J. and Hirst, A. A. (1993). A Systems Approach to the Control of Welding Fumes at Source. Ann. Occup. Hyg. 37:297-306.

IARC (1990). Monographs on the Evaluation of Carcinogenic Risks to Humans: Chromium, Nickel and Welding

ICRP (1994). Human Respiratory Tract Model for Radiological Protection. Anals of the ICRP, Publication 66.

Ikävalko, E., Laitinen, T. and Revitzer, H. (1999). Optimised method of coal digestion for trace metal determination by atomic absorption spectroscopy. Fresenius J. Anal. Chem. 363:314-316.

Iler, R. K. (1979). The Chemistry of Silica: Solubility, Polymerization, Colloid and Surface Properties and Biochemistry of Silica. Wiley-Interscience.

ISO (1995). Extraction of Trace Elements Soluble in Aqua Regia, ISO 11466.

IUPAC (1997). Detection Limit, in Compendium of Chemical Terminology.

Jie, S., De-ren, W., Ye-dong, H., Hui-bin, Q. and Gao, W. (2008). Reduction of oxide scale on hot-rolled strip steels by carbon monoxide. Mater. Lett. 62:3500-3502.

Kasprzak, K. S., Sunderman Jr, F. W. and Salnikow, K. (2003). Nickel carcinogenesis. Mutation Research/Fundamental and Molecular Mechanisms of Mutagenesis 533:67-97.

Keane, M., Stone, S. and Chen, B. (2010). Welding fumes from stainless steel gas metal arc processes contain multiple manganese chemical species. J Environ Monitor 12:1133-1140.

Keskinen, H., Kalliomäki, P. L. and Alanko, K. (1980). Occupational Asthma Due to Stainless Steel Welding Fumes. Clin. Exp. Allergy 10:151-159.

Kim, S., Harrington, M. and Pui, D. (2007). Experimental study of nanoparticles penetration through commercial filter media, in Nanotechnology and Occupational Health, A. D. Maynard and D. Y. H. Pui, eds., Springer Netherlands, 117-125.

Kittelson, D. B., Watts, W. F. and Johnson, J. P. (2006). On-road and laboratory evaluation of combustion aerosols--Part1: Summary of diesel engine results. J. Aerosol Sci. 37:913-930.

Korczynski, R. E. (2000). Occupational health concerns in the welding industry. Appl. Occup. Environ. Hyg. 15:936-945.

Kosmatka, S. H., Kerkhoff, B. and Panarese, W. C. (2002). Design and control of concrete mixtures. Portland Cement Association, Skokie, IL.

Kropschot, S. J. and Doebrich, J. (2010). Chromium - Makes stainless steel stainless USGS Mineral Resources Program.

Kula, I., Olgun, A., Erdogan, Y. and Sevinc, V. (2001). Effects of colemanite waste, cool bottom ash, and fly ash on the properties of cement. Cem. Concr. Res. 31:491-494.

Kuss, H. M. (1992). Applications of microwave digestion technique for elemental analyses. Fresenius J. Anal. Chem. 343:788-793.

Lamble, K. and Hill, S. (1998). Microwave digestion procedures for environmental matrices . Critical Review. Analyst 123:103R-133R.

Lampman, S., ed. (1997). Weld Integrity and Performance. ASM International Materials Park, OH.

Langård, S. (1988). Chromium carcinogenicity: A review of experimental animal data. Sci. Total Environ. 71:341-350.

Langford, N. and Ferner, R. (1999). Toxicity of mercury. J. Hum. Hypertens. 13:651-656.

Laohaudomchok, W., Lin, X., Herrick, R. F., Fang, S. C., Cavallari, J. M., Shrairman, R., Landau, A., Christiani, D. C. and Weisskopf, M. G. (2011). Neuropsychological Effects of Low-level Manganese Exposure in Welders. NeuroToxicology 32:171-179.

Laudal, D. L. and Heidt, M. K. (1997). Evaluation of flue gas mercury speciation method, Energy and Environmental Research Center, Grand Forks, ND.

Lavoisier, A. (1984). Elements of Chemistry. Dover Publications

Lee, M.-H., McClellan, W., Candela, J., Andrews, D. and Biswas, P. (2007). Reduction of Nanoparticle Exposure to Welding Aerosols by Modification of the Ventilation System in a Workplace. J. Nanopart. Res. 9:127-136.

Lee, S.-R. and Wu, C.-Y. (2005). Size Distribution Evolution of Fine Aerosols Due to Intercoagulation with Coarse Aerosols. Aerosol Sci. Technol. 39:358-370.

Li, G. J., Zhang, L.-L., Lu, L., Wu, P. and Zheng, W. (2004). Occupational Exposure to Welding Fume among Welders: Alterations of Manganese, Iron, Zinc, Copper, and Lead in Body Fluids and the Oxidative Stress Status. J. Occup. Environ. Med. 46:241-248.

Li, H., Li, Y., Wu, C.-Y. and Zhang, J. (2011). Oxidation and capture of elemental mercury over SiO_2–TiO_2–V_2O_5 catalysts in simulated low-rank coal combustion flue gas. Chem. Eng. J. 169:186-193.

Li, Y. and Wu, C.-Y. (2006). Role of moisture in adsorption, photocatalytic oxidation, and reemission of elemental mercury on a SiO2-TiO2 nanocomposite. Environ. Sci. Technol. 40:6444-6448.

Linero, A. (2011). Synopsis of mercury (Hg) controls at Florida cement plants, in 104th Air and Waste Management Association Annual Conference and Exhibition, Orlando, FL, 782.

Lippold, J. C. and Frankel, G. S. (2009). SERDP Project Report PP-1415: Development of chromium-free welding consumables for stainless steels, Ohio State University, 2009, Columbus, OH.

Liz-Marzán, L. M., Giersig, M. and Mulvaney, P. (1996). Synthesis of Nanosized Gold−Silica Core−Shell Particles. Langmuir 12:4329-4335.

Lu, Y., Yin, Y., Li, Z.-Y. and Xia, Y. (2002). Synthesis and Self-Assembly of Au-SiO2 Core−Shell Colloids. Nano Lett. 2:785-788.

Lundborg, M., Dahlén, S.-E., Johard, U., Gerde, P., Jarstrand, C., Camner, P. and Låstbom, L. (2006). Aggregates of Ultrafine Particles Impair Phagocytosis of Microorganisms by Human Alveolar Macrophages. Environ. Res. 100:197-204.

Marshall, P. (1984). Austenitic Stainless Steels: Microstructure and Mechanical Properties. Elsevier Applied Science, London, UK.

Maslehuddin, M., Al-Amoudi, O. S. B., Rahman, M. K., Ali, M. R. and Barry, M. S. (2009). Properties of cement kiln dust concrete. Constr. Build. Mater. 23:2357-2361.

Mayer, C., Klein, R. G., Wesch, H. and Schmezer, P. (1998). Nickel subsulfide is genotoxic in vitro but shows no mutagenic potential in respiratory tract tissues of BigBlue™ rats and Muta™Mouse mice in vivo after inhalation. Mutation Research/Genetic Toxicology and Environmental Mutagenesis 420:85-98.

Maynard, A. D., Ito, Y., Arslan, I., Zimmer, A. T., Browning, N. and Nicholls, A. (2004). Examining Elemental Surface Enrichment in Ultrafine Aerosol Particles Using Analytical Scanning Transmission Electron Microscopy. Aerosol Sci. Technol. 38:365-381.

McLaren, J. W. and Berman, S. S. (1985). Wavelength selection for trace analysis by ICP-AES. Spectrochim. Acta, Part B 40:217-225.

McMillin, B. K., Biswas, P. and Zachariah, M. R. (1996). In situ characterization of vapor phase growth of iron oxide-silica nanocomposites: Part I. 2-D planar laser-induced fluorescence and Mie imaging. J. Mater. Res. 11:1552-1561.

Meeker, J. D., Susi, P. and Flynn, M. R. (2010). Hexavalent chromium exposure and control in welding tasks. J. Occup. Environ. Hyg. 7:607 - 615.

Menzel, M. (2003). The influence of individual components of an industrial gas mixture on the welding process and the properties of welded joints. Weld. Int. 17:262-264.

Menzel, N., Schramel, P. and Wittmaack, K. (2002). Elemental composition of aerosol particulate matter collected on membrane filters: A comparison of results by PIXE and ICP-AES. Nucl. Instrum. Methods Phys. Res., Sect. B 189:94-99.

Mlakar, T. L., Horvat, M., Vuk, T., Stergaršek, A., Kotnik, J., Tratnik, J. and Fajon, V. (2010). Mercury species, mass flows and processes in a cement plant. Fuel 89:1936-1945.

Moroni, B. and Viti, C. (2009). Grain Size, Chemistry, and Structure of Fine and Ultrafine Particles in Stainless Steel Welding Fumes. J. Aerosol Sci. 40:938-949.

Myöhänen, T., Mäntylahti, V., Koivunen, K. and Matilainen, R. (2002). Simultaneous determination of As, Cd, Cr and Pb in aqua regia digests of soils and sediments using electrothermal atomic absorption spectrometry and fast furnace programs. Spectrochim. Acta, Part B 57:1681-1688.

Nadkarni, R. A. (1984). Applications of microwave oven sample dissolution in analysis. Anal. Chem. 56:2233-2237.

Niitsoo, O. and Couzis, A. (2011). Facile Synthesis of Silver Core - Silica Shell Composite Nanoparticles. J. Colloid Interface Sci. 354:887-890.

NIOSH (2008). Criteria document update: Occupational exposure to hexavalent chromium, Cincinnati, OH.

NIOSH (1994). Method 7604: chromium, hexavalent, Cincinnati, OH:.

NIOSH (2013). NIOSH Publication No. 2013-128: Criteria for a Recommended Standard: Occupational Exposure to Hexavalent Chromium, Cincinnati, OH.

NIOSH (2007). Pocket Guide to Chemical Hazards, Cincinnati, OH.

Oberdorster, G., Maynard, A., Donaldson, K., Castranova, V., Fitzpatrick, J., Ausman, K., Carter, J., Karn, B., Kreyling, W., Lai, D., Olin, S., Monteiro-Riviere, N., Warheit, D. and Yang, H. (2005). Principles for characterizing the potential human health effects from exposure to nanomaterials: elements of a screening strategy. Particle and Fibre Toxicology 2:8.

Oberdörster, G., Stone, V. and Donaldson, K. (2007). Toxicology of nanoparticles: A historical perspective. Nanotoxicology 1:2-25.

Ohmori, M. and Matijevic, E. (1992). Preparation and properties of uniform coated colloidal particles. VII. Silica on hematite. J. Colloid Interface Sci. 150:594-598.

Okorie, A., Entwistle, J. and Dean, J. R. (2010). The optimization of microwave digestion procedures and application to an evaluation of potentially toxic element contamination on a former industrial site. Talanta 82:1421-1425.

Oller, A. R., Kirkpatrick, D. T., Radovsky, A. and Bates, H. K. (2008). Inhalation carcinogenicity study with nickel metal powder in Wistar rats. Toxicology and Applied Pharmacology 233:262-275.

OSHA (2006a). Chromium (VI), in Toxic and Hazardous Substances, Occupational Safety and Health Standards.

OSHA (2006b). Mercury, in Toxic and Hazardous Substances, Occupational Safety and Health Standards.

OSHA (2006c). Nitrogen dioxide, in Toxic and Hazardous Substances, Occupational Safety and Health Standards.

Owens, T. M. and Biswas, P. (1996). Vapor phase sorbent precursors for toxic metal emissions control from combustors. Industrial & Engineering Chemistry Research 35:792-798.

Paulson, K. and Wu, C.-Y. (2012). ESTCP Project Report WP-0903: Innovative welding technologies to control HAP emissions using silicon additives, University of Florida, Gainesville, FL.

Paulson, K. M., Wang, J., Topham, N., Wu, C. Y., Alexandrov, B. T., Lippold, J. C. and Es-Said, O. S. (2011). Alternatives for Joining Stainless Steel to Reduce Cr(VI) Emissions and Occupational Exposures. J. Ship Prod. Des. 27:91-97.

PCA (1992). An analysis of selected trace metals in cement and kiln dust, Portland Cement Association, Skokie, IL, 4.

Peckner, D. and Bernstein, I. M. (1977). Handbook of Stainless Steel. McGraw-Hill.

Pellerin, C. and Booker, S. M. (2000). Reflections on hexavalent chromium: Health hazards of an industrial heavyweight. Environ. Health Perspect. 108.

Pistilli, M. and Majko, R. (1984). Optimizing the amount of Class C fly ash in concrete mixtures 6.

Pocock, D., Saunders, C. J. and Carter, G. (2009). Effective control of gas shielded arc welding fume, H. a. S. Executive, ed.

Rice, M. B., Cavallari, J., Fang, S. and Christiani, D. (2011). Acute Decrease in HDL Cholesterol Associated With Exposure to Welding Fumes. J. Occup. Environ. Med. 53:17-21.

Richman, J. D., Livi, K. J. T., Spannhake, E. W., Macri, K. K., Torrey, C. M. and Geyh, A. S. (2008). Assessment of Pulmonary Exposure to Manganese: Uptake of Metals from Inhaled Welding Fumes into the Circulatory System. Epidemiology 19:S262-S262.

Rubio, R., Huguet, J. and Rauret, G. (1984). Comparative study of the Cd. Cu and Pb determination by AAS and by ICP-AES in river water : Application to a mediterranean river (Congost river, Catalonia, Spain). Water Res. 18:423-428.

Sandroni, V., Smith, C. M. M. and Donovan, A. (2003). Microwave digestion of sediment, soils and urban particulate matter for trace metal analysis. Talanta 60:715-723.

Schoonover, T., Conroy, L., Lacey, S. and Plavka, J. (2011). Personal Exposure to Metal Fume, NO_2, and O_3 among Production Welders and Non-welders. Ind. Health 49:63-72.

Scott, D. R., Loseke, W. A., Holboke, L. E. and Thompson, R. J. (1976). Analysis of Atmospheric Particulates for Trace Elements by Optical Emission Spectrometry. Appl. Spectrosc. 30:392-405.

Senior, C., Montgomery, C. J. and Sarofim, A. (2009). Transient model for behavior of mercury in Portland cement kilns. Ind. Eng. Chem. Res. 49:1436-1443.

Sethi, V. and Biswas, P. (1990). Modeling of Particle Formation and Dynamics in a Flame Incinerator. J. Air Waste Manage. Assoc. 40:42-46.

Siddique, R. (2006). Utilization of cement kiln dust (CKD) cement mortar and concrete—an overview. Resour. Conserv. Recycl. 48:315-338.

Sievering, H., Dave, M. J., McCoy, P. G. and Walther, K. (1978). Cellulose filter high-volume cascade impactor aerosol collection efficiency. A technical note. Environ. Sci. Technol. 12:1435-1437.

Sriram, K., Lin, G. X., Jefferson, A. M., Roberts, J. R., Chapman, R. S., Chen, B. T., Soukup, J. M., Ghio, A. J. and Antonini, J. M. (2010). Dopaminergic neurotoxicity following pulmonary exposure to manganese-containing welding fumes. Arch. Toxicol. 84:521-540.

Summers, M. J., Summers, J. J., White, T. F. and Hannan, G. J. (2011). The Effect of Occupational Exposure to Manganese Dust and Fume on Neuropsychological Functioning in Australian Smelter Workers. J. Clin. Exp. Neuropsychol. 33:692-703.

Tan, S. H. and Horlick, G. (1987). Matrix-effect observations in inductively coupled plasma mass spectrometry. J. Anal. At. Spectrom. 2:745-763.

Teleki, A., Suter, M., Kidambi, P. R., Ergeneman, O., Krumeich, F., Nelson, B. J. and Pratsinis, S. E. (2009). Hermetically Coated Superparamagnetic Fe_2O_3 Particles with SiO2 Nanofilms. Chem. Mater. 21:2094-2100.

Thaon, I., Demange, V., Herin, F., Touranchet, A. and Paris, C. (2012). Increased Lung Function Decline in Blue-collar Workers Exposed to Welding Fumes. Chest.

Todoli, J. L., Gras, L., Hernandis, V. and Mora, J. (2002). Elemental matrix effects in ICP-AES. J. Anal. At. Spectrom. 17:142-169.

Topham, N., Kalivoda, M., Hsu, Y.-M., Wu, C.-Y., Oh, S. and Cho, K. (2010). Reducing Cr^{6+} emissions from gas tungsten arc welding using a silica precursor. J. Aerosol Sci. 41:326-330.

Topham, N., Wang, J., Kalivoda, M., Huang, J., Yu, K.-M., Hsu, Y.-M., Wu, C.-Y., Oh, S., Cho, K. and Paulson, K. (2011). Control of Cr^{6+} Emissions from Gas Metal Arc Welding Using a Silica Precursor as a Shielding Gas Additive. Ann. Occup. Hyg. 56:242-252.

USEPA (2010). 75 FR 54970: National emission standards for hazardous air pollutants from the portland cement manufacturing industry and standards of performance for portland cement plants; Final rule, Washington, DC.

USEPA (2011). Materials characterization paper in support of the final rulemaking: identification of nonhazardous secondary materials that are solid waste - cement kiln dust (CKD), Washington, DC.

USEPA (2005). Method 3200: Mercury species fractionation and quantification by microwave assisted extraction, selective solvent extraction and/or solid phase extraction, Washington, DC.

USEPA (2007). Method 7474: Mercury in sediment and tissue samples by atomic fluorescence spectrometry, Washington, DC.

USEPA (1998). Toxicological review of hexavalent chromium, Washington, DC.

USGS (2013). Cement statistics and information.

Vitek, J. M. and David, S. A. (1987). The aging behavior of homogenized type 308 and 308CRE stainless steel. Metall. Trans. A 18A:7:1195-1202.

Wallace, M., Shulman, S. and Sheehy, J. (2001). Comparing exposure levels by type of welding operation and evaluating the effectiveness of fume extraction guns. Appl. Occup. Environ. Hyg. 16:771-779.

Wang, J., Kalivoda, M., Guan, J., Theodore, A., Sharby, J., Wu, C.-Y., Paulson, K. and Es-Said, O. (2012). Double Shroud Delivery of Silica Precursor for Reducing Hexavalent Chromium in Welding Fume. J. Occupy. Environ. Hyg. 9:733-742.

Wang, J., Topham, N. and Wu, C.-Y. (2011). Determination of silica coating efficiency on metal particles using multiple digestion methods. Talanta 85:2655-2661.

Webb, E., Amarasiriwardena, D., Tauch, S., Green, E. F., Jones, J. and Goodman, A. H. (2005). Inductively coupled plasma-mass (ICP-MS) and atomic emission spectrometry (ICP-AES): Versatile analytical techniques to identify the archived elemental information in human teeth. Microchem. J. 81:201-208.

Williams, D. B. and Carter, C. B. (2009). Transmission Electron Microscopy: A Textbook for Materials Science. Springer, New York, NY.

WTIA (1999). Fume minimisation guidelines: welding, cutting, brazing and soldering.

Wu, S., Zhao, Y.-H., Feng, X. and Wittmeier, A. (1996). Application of inductively coupled plasma mass spectrometry for total metal determination in silicon-containing solid samples using the microwave-assisted nitric acid-hydrofluoric acid-hydrogen peroxide-boric acid digestion system. J. Anal. At. Spectrom. 11:287-296.

Xu, Y.-H., Iwashita, A., Nakajima, T., Yamashita, H., Takanashi, H. and Ohki, A. (2005). Effect of HF addition on the microwave-assisted acid-digestion for the

determination of metals in coal by inductively coupled plasma-atomic emission spectrometry. Talanta 66:58-64.

Yi, D. K., Selvan, S. T., Lee, S. S., Papaefthymiou, G. C., Kundaliya, D. and Ying, J. Y. (2005). Silica-Coated Nanocomposites of Magnetic Nanoparticles and Quantum Dots. J. Am. Chem. Soc. 127:4990-4991.

Yu, I. J., Kim, K. J., Chang, H. K., Song, K. S., Han, K. T., Han, J. H., Maeng, S. H., Chung, Y. H., Park, S. H., Chung, K. H., Han, J. S. and Chung, H. K. (2000). Pattern of Deposition of Stainless Steel Welding Fume Particles Inhaled into the Respiratory Systems of Sprague-Dawley Rats Exposed to a Novel Welding Fume Generating System. Toxicol. Lett. 116:103-111.

Yu, K.-M., Topham, N., Wang, J., Kalivoda, M., Tseng, Y., Wu, C.-Y., Lee, W.-J. and Cho, K. (2011). Decreasing biotoxicity of fume particles produced in welding process. J. Hazard. Mater. 185:1587-1591.

Yu, K., Grabinski, C., Schrand, A., Murdock, R., Wang, W., Gu, B., Schlager, J. and Hussain, S. (2009). Toxicity of Amorphous Silica Nanoparticles in Mouse Keratinocytes. J. Nanopart. Res. 11:15-24.

Zatka, V. J. (1985). Speciation of hexavalent chromium in welding fumes interference by air oxidation of chromium. Am. Ind. Hyg. Assoc. J. 46:327-331.

Zeidler-Erdely, P. C., Battelli, L. A., Stone, S., Chen, B. T., Frazer, D. G., Young, S.-H., Erdely, A., Kashon, M. L., Andrews, R. and Antonini, J. M. (2011). Short-term Inhalation of Stainless Steel Welding Fume Causes Sustained Lung Toxicity But No Tumorigenesis in Lung Tumor Susceptible A/J Mice. Inhalation Toxicol. 23:112-120.

Zeidler-Erdely, P. C., Kashon, M. L., Battelli, L. A., Young, S. H., Erdely, A., Roberts, J. R., Reynolds, S. H. and Antonini, J. M. (2008). Pulmonary inflammation and tumor induction in lung tumor susceptible A/J and resistant C57BL/6J mice exposed to welding fume. Part. Fibre Toxicol. 5.

Zimmer, A. T. and Biswas, P. (2001). Characterization of the Aerosols Resulting from Arc Welding Processes. J. Aerosol Sci. 32:993-1008.

BIOGRAPHICAL SKETCH

Jun Wang was born in Shanxi Province, China in June 1984. He graduated from Nankai University twice, with a Bachelor of Engineering in environmental engineering (2006), and a Master of Science in environmental management and economics (2009). From 2005 to 2009, he was actively involved in various studies at China State Environmental Protection Key Laboratory of Particulate Matters Pollution and Control. The research resulted in one first-authored journal paper, one co-authored journal paper, and two co-authored books. He also worked as an instructor for environmental management courses at Tianjin Bohai Vocational College from 2006 to 2007.

Jun joined Dr. Chang-Yu Wu's research group at the University of Florida in the summer of 2009. His primary research was about welding fume control technologies, while also participated in several other projects. During the four-year doctoral study, he published several first-authored journal papers. He received various prestigious academic scholarships, travel grants, and poster competition awards from different professional organizations. He served in the professional community, in the form of conference committee member, conference abstract reviewer, peer-reviewed journal reviewer, student chapter president, and conference student volunteer. He graduated in Aug 2013 with a Doctor of Philosophy (Ph.D.) in environmental engineering sciences from the University of Florida, and immediately joined the University of Oklahoma Health Science Center as tenure-track assistant professor.